Dissertation

VTT PUBLICATIONS 773

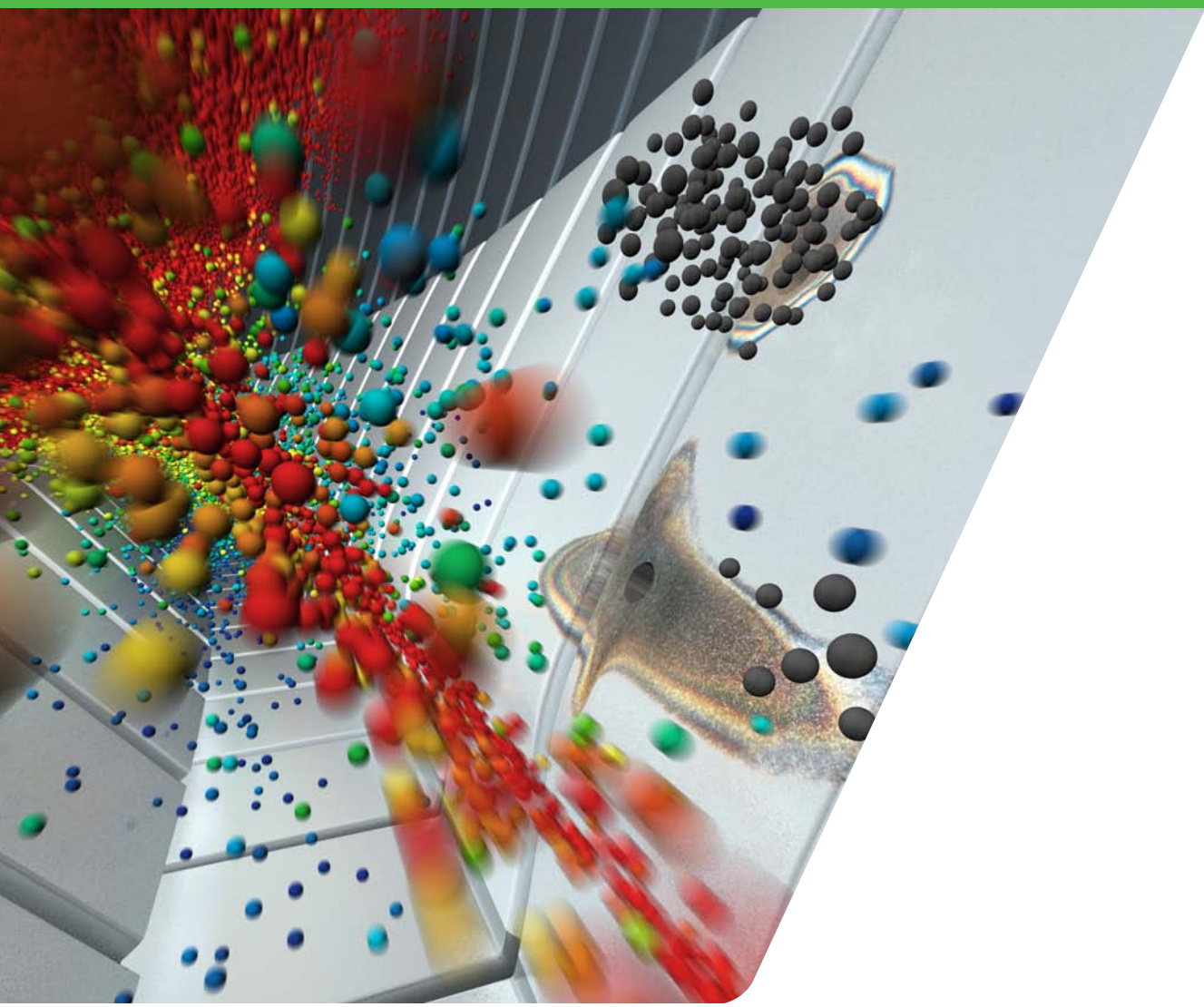

Leena Aho-Mantila

Divertor plasma conditions and their effect on carbon migration in the ASDEX Upgrade tokamak

VTT PUBLICATIONS 773

Divertor plasma conditions and their effect on carbon migration in the ASDEX Upgrade tokamak

Leena Aho-Mantila

Dissertation for the degree of Doctor of Science in Technology to be presented with due permission of the School of Science for public examination and debate in Auditorium K216 at the Aalto University School of Science (Espoo, Finland) on the 4th of November, 2011, at 12 noon.

ISBN 978-951-38-7756-9 (soft back ed.)
ISSN 1235-0621 (soft back ed.)

ISBN 978-951-38-7757-6 (URL: http://www.vtt.fi/publications/index.jsp)
ISSN 1455-0849 (URL: http://www.vtt.fi/publications/index.jsp)

JULKAISIJA – UTGIVARE – PUBLISHER

VTT, Vuorimiehentie 5, PL 1000, 02044 VTT
puh. vaihde 020 722 111, faksi 020 722 4374

VTT, Bergsmansvägen 5, PB 1000, 02044 VTT
tel. växel 020 722 111, fax 020 722 4374

VTT Technical Research Centre of Finland, Vuorimiehentie 5, P.O. Box 1000, FI-02044 VTT, Finland
phone internat. +358 20 722 111, fax + 358 20 722 4374

Cover: Jyrki Hokkanen, CSC (Data: Leena Aho-Mantila)

Kopijyvä Oy, Kuopio 2011

Leena Aho-Mantila. Divertor plasma conditions and their effect on carbon migration in the ASDEX Upgrade tokamak [Diverttorin plasmaolosuhteet ja niiden vaikutus hiilen kulkeutumiseen ASDEX Upgrade -tokamakissa]. Espoo 2011. VTT Publications 773. 76 p. + app. 62 p.

Keywords tokamak, plasma-material interaction, scrape-off layer, kinetic modelling, fluid modelling, ASDEX Upgrade, fusion energy

Abstract

Divertors play a critical role in power and particle exhaust and plasma-material interaction in tokamaks. Of particular concern is the release of impurities from the material components, which reduces the lifetime of the vessel wall and affects the fusion performance. Furthermore, impurities with low charge number can migrate and re-deposit forming potentially tritium-rich layers in the tokamak. Sophisticated numerical simulations are required to understand how the various complex and often nonlinear processes in the plasma boundary affect the divertor performance.

This thesis investigates the plasma conditions and the migration of impurities in the divertor region, using numerical code packages with the most complete available description of the relevant physical processes. It is known from earlier studies that the codes have both weaknesses and uncertainties in their models, which limits our current predictive capabilities. In this thesis work, carbon injection experiments at the ASDEX Upgrade tokamak are modelled. The work assesses the present-day boundary plasma models and elucidates impurity migration processes by comparing the simulations with experimental data.

The results show that both the local migration and the net erosion of carbon are sensitive to the divertor plasma conditions. Good agreement between the modelled and measured divertor plasma parameters is obtained for a limited operational regime at low density. In this regime, the measured carbon migration is also reproduced in the simulations, and it is shown to be significantly affected by the electric field and the collisionality of the plasma in the divertor region. A significant improvement in code-experiment agreement is obtained after drifts arising from electric and magnetic fields are included in both plasma and impurity simulations. At higher plasma densities, collisionless hot electrons are a potential explanation for the deficiencies observed when benchmarking the plasma models against experiments.

Leena Aho-Mantila. Divertor plasma conditions and their effect on carbon migration in the ASDEX Upgrade tokamak [Diverttorin plasmaolosuhteet ja niiden vaikutus hiilen kulkeutumiseen ASDEX Upgrade -tokamakissa]. Espoo 2011. VTT Publications 773. 76 s. + liitt. 62 s.

Asiasanat tokamak, plasma-material interaction, scrape-off layer, kinetic modelling, fluid modelling, ASDEX Upgrade, fusion energy

Tiivistelmä

Diverttorilla on tärkeä rooli tokamakin ensiseinämän läheisyydessä olevan plasman olosuhteiden ja plasma-materiaalivuorovaikutuksen säätelyssä. Erityisenä huolena on materiaalipintojen eroosio, joka lyhentää seinämien elinikää ja tuottaa epäpuhtauksia plasmaan. Epäpuhtauksien kulkeutumisesta riippuu, miten epäpuhtaudet vaikuttavat fuusioreaktorin suorituskykyyn ja mihin ne kerrostuvat uudelleen, mahdollisesti yhdessä tritiumin kanssa. Koska diverttorin toimintaan vaikuttavat prosessit ovat monimutkaisia ja epälineaarisia, niiden kuvaamiseen tarvitaan kehittyneitä simulointiohjelmistoja.

Tässä väitöskirjassa tarkastellaan diverttorialueen plasmaolosuhteita ja epäpuhtauksien kulkeutumista käyttäen tulevaisuuden koelaitteiden suunnitteluun tähtääviä simulointiohjelmistoja. Nämä ohjelmistot sisältävät viimeisimmät saatavilla olevat fysiikkamallit, mutta aiemmat työt ovat tuoneet esille merkittäviä epävarmuuksia niiden laskentatuloksissa. Väitöskirjassa simuloidaan ASDEX Upgrade -tokamakilla tehtyjä kokeita, joissa hiiltä on injektoitu diverttorialueelle. Työssä arvioidaan nykyisten reunaplasmamallien oikeellisuutta ja selvitetään hiilen kulkeutumisominaisuuksia vertaamalla simulaatiotuloksia kokeellisiin mittauksiin.

Työn tulokset osoittavat, että hiilen kokonaiseroosio ja paikallinen kulkeutuminen vaihtelevat diverttorin plasmaolosuhteiden mukaan. Simulaatioilla pystytään hyvin toistamaan mitatut plasmaolosuhteet rajatulla alhaisen tiheyden käyttöalueella. Tässä tapauksessa myös mallinnettu hiilen kulkeutuminen vastaa mittaustuloksia, ja sen osoitetaan riippuvan voimakkaasti diverttorialueen sähkökentästä ja plasman törmäyksellisyydestä. Sähkö- ja magneettikentistä johtuvan ajautumisen huomioiminen parantaa merkittävästi niin plasma- kuin epäpuhtaussimulaatioiden vastaavuutta koetulosten kanssa. Törmäyksettömät korkeaenergiset elektronit voivat selittää simulaatioiden ja kokeiden välisiä eroavaisuuksia suuremmilla plasmatiheyksillä.

Preface and acknowledgements

My first acquaintance with tokamak physics took place already in 2004, when Prof. Rainer Salomaa gave me an opportunity to work as a summer student at the Laboratory of Advanced Energy Systems at TKK. After finishing my Master's thesis in 2007, I continued at TKK with the doctoral research presented in this thesis. For the past two years I have worked at the Technical Research Centre of Finland (VTT). This thesis would not have been possible without continuous support from association Euratom-TEKES. I am grateful in particular to Rainer and our head of research unit, Dr. Seppo Karttunen, for the confidence they have had in me since the very beginning.

Of all the people who contributed to the research, I first want to thank Dr. Marco Wischmeier from the Max-Planck-Institute for Plasma Physics (IPP), who has been my primary instructor and supporter for the last three and a half years. I am deeply grateful to him for the way he has helped me to develop towards a professional researcher, and for the substantial time he has spent discussing the physics issues with me, as well as reading my papers and this manuscript. His genuine interest in my research has encouraged me to continue the hard work during all these years.

During the doctoral work, I made several visits to IPP in Garching, Germany, where I worked on ASDEX Upgrade experiments and was supported in the modelling tasks. I wish to thank Dr. David Coster and Dr. Alex Chankin for inspiring physics discussions and for the encouragement I received during the tough first learning period, as well as later on during the thesis work. Members of the ASDEX Upgrade team supported me in the experimental work, and I thank them for all their help and their welcoming attitude. I am grateful in particular to Dr. Hans Werner Müller, Mr. Steffen Potzel and Dr. Volker Rohde for their support and time. Dr. Karl Krieger deserves special thanks for providing the crucial surface analysis data for my work. I'm also grateful to Dr. Roberto Pugno, who first proposed the modelling of carbon migration experiments to me and helped me take over the experimental work.

At VTT, I wish to thank in particular my local supervisor, Dr. Markus Airila, who helped me with the modelling and dealt with many bureaucratic issues

during the years. I am grateful for his continuously positive attitude towards my work. I also want to thank Dr. Antti Hakola for performing some of the surface analyses. There's been a really good atmosphere in our group, and I thank all my colleagues for bearing with me in the finalization of this work.

During the last year of my doctoral work, I managed to make a few short visits to the Forschungszentrum Jülich (FZJ) in Germany. I thank my hosts Dr. Andreas Kirschner and Dr. Dmitry Borodin for their hospitality during those visits and, more importantly, for their continuous support in the modelling of plasma-wall interaction.

At TKK (nowadays Aalto University), I thank Dr. Taina Kurki-Suonio and Dr. Seppo Sipilä for contributing to my first publication. I'm also thankful to Dr. Mathias Groth for nice physics discussions during my final year at TKK. Furthermore, I thank my fellow doctoral students at both TKK and IPP for the pleasant working atmosphere and for the nice times we have had outside work.

The manuscript was reviewed by Dr. Richard Pitts, ITER organization, and Dr. Jim Strachan, Princeton University. I thank both of them for their careful work and for encouraging me in my professional career.

Finally, I wish to thank my family and friends for their invaluable help. My parents have continuously supported me, and my two brothers and friends have provided both diversity and comfort in life, for which I am grateful.

The thesis work received funding from EFDA PWI and ITM taskforces, EFDA GOTiT program, and the Academy of Finland. Part of the computations were made using CSC's computing environment. Personal grants from Fortum Foundation and Magnus Ehrnrooth Foundation are gratefully acknowledged.

Espoo, September 29, 2011

Leena Aho-Mantila

Contents

List of Publications

This thesis consists of an overview and the following five publications (listed in chronological order):

I Aho-Mantila L K, Kurki-Suonio T, Chankin A V, Coster D P and Sipilä S K, "ASCOT simulations of electron energy distribution at the divertor targets in an ASDEX Upgrade H-mode discharge", Plasma Physics and Controlled Fusion **50** (2008) 065021 (13 pp)

II Aho-Mantila L, Airila M I, Wischmeier M, Krieger K, Pugno R, Coster D P, Chankin A V, Neu R, Rohde V and the ASDEX Upgrade Team, "Modelling of $^{13}CH_4$ injection and local carbon deposition at the outer divertor of ASDEX Upgrade", Physica Scripta **T138** (2009) 014019 (4 pp)

III Aho-Mantila L, Wischmeier M, Airila M I, Chankin A V, Coster D P, Fuchs Ch, Groth M, Kirschner A, Krieger K, Müller H W, Wolfrum E, and the ASDEX Upgrade Team, "Modelling of Carbon Transport in the Outer Divertor Plasma of ASDEX Upgrade", Contributions to Plasma Physics **50**, No. 3-5, 439-444 (2010)

IV Aho-Mantila L, Wischmeier M, Krieger K, Rohde V, Müller H W, Coster D P, Groth M, Kirschner A, Neu R, Potzel S, Sieglin B, Wolfrum E, The ASDEX Upgrade Team, "Effect of $\mathbf{E} \times \mathbf{B}$ driven transport on the deposition of carbon in the outer divertor of ASDEX Upgrade", accepted for publication in Journal of Nuclear Materials (2010) (4 pp)

V Aho-Mantila L, Wischmeier M, Krieger K, Müller H W, Potzel S, Rohde V, Hakola A, Coster D P, Kirschner A, Bonnin X, Borodin D, Conway G D and the ASDEX Upgrade Team, "Influence of magnetic field reversal on the divertor plasma and its impact on local carbon migration in ASDEX Upgrade", submitted for publication in Nuclear Fusion (2011) (35 pp)

Author's contribution

The publications are based on extensive simulation efforts using sophisticated numerical code packages which have been developed over the years by several contributors. The author has carried out all the simulations presented in Publications I–V, including their post-processing and analysis. This excludes the SOLPS5.0 modelling results described in Publication I, which are presented in detail in [1]. The author has carried out the integration of the codes and contributed to the associated development of the ASCOT and ERO codes. Members of the respective modelling groups have supported the author in the modelling work and are listed as co-authors in the publications.

A large part of the work has involved analysis of experimental data from ASDEX Upgrade. The author was responsible for the planning and coordination of the experiments reported in Publications IV–V, excluding the 2007 ^{13}C injection experiment which is reported in [2] and the ramp-up of methane injection rate presented in Publication V. The measurements from the plasma discharges presented in all publications have been performed by members of the ASDEX Upgrade team, and the ion-beam analyses have been made by experts at IPP and VTT. These contributors are listed as co-authors in Publications II–V. The main part of the empirical analysis and, in particular, the comparison between the experimental results and modelling, has been carried out by the author.

The author has written the main part of the text and prepared the figures presented in Publications I–V. She was the principal author in all these publications. In addition to this work, the author has contributed to Publications [2–6].

List of Symbols

$\mathbf{B}$	Magnetic field
$\mathbf{E}$	Electric field
r_L	Larmor radius
λ_D	Debye length
Z	Charge number of species
e	Elementary charge
q	Particle charge
m	Particle mass
$\mathbf{v}$	Particle velocity
v_th	Thermal particle speed
$\mathbf{v}_{\nabla\mathbf{B}}$	Guiding centre $\nabla\mathbf{B}$ drift
$\mathbf{v}_{\mathbf{E}\times\mathbf{B}}$	Guiding centre $\mathbf{E}\times\mathbf{B}$ drift
$\mathbf{u}$	Fluid velocity
c_s	Ion sound speed
M	Fluid Mach number
I_p	Plasma current
I_d	Divertor current
T	Plasma temperature (eV)
n	Plasma density
$T_\mathrm{M-B}$	Temperature in Maxwell-Boltzmann distribution
λ_coll	Collision mean-free path
ϵ_0	Vacuum permittivity
ψ	Magnetic field incidence angle
$\mathbf{E}_\mathrm{mps}$	Electric field in the magnetic presheath
V_sh	Potential drop in the magnetic and electrostatic sheaths
V_ps	Potential drop in the presheath
γ	Ratio of specific heats
Γ_se	Parallel ion flux at the sheath entrance
$\lambda_{q_\parallel}$	Radial decay length of parallel heat flux
χ	Heat conductivity
$\mathbf{q}$	Heat flux
Y_phys	Physical sputtering yield

Y_{chem}	Chemical erosion yield
E_{B}	Surface binding energy
E_{th}	Threshold impact energy for sputtering
T_{max}	Surface temperature for maximum erosion yield
Φ	Ion flux density at material surface
R_{prob}	Reflection probability
S_{prob}	Sticking probability
R	Major radius
a	Minor radius
S	Poloidal coordinate along the target
ρ	Poloidal flux coordinate
f	Distribution function
$\mathbf{\Pi}$	Parallel stress tensor
$\mathbf{j}$	Current density
d_{int}	Interaction depth

Subscripts:

$X_{\parallel}$	Component parallel to magnetic field
$X_{\perp}$	Component perpendicular to magnetic field
X_{ϕ}	Component in toroidal direction
X_{θ}	Component in poloidal direction
X_{r}	Component in radial direction
X_{i}	Component related to ions
X_{e}	Component related to electrons
X_{u}	Value at upstream location
X_{t}	Value at target

List of Abbreviations

LCFS	Last closed flux surface
PFC	Plasma-facing component
PWI	Plasma-wall interaction
SOL	Scrape-off layer
PFR	Private-flux region
H-mode	High-confinement mode
L-mode	Low-confinement mode
ELM	Edge-localized mode
LSN	Lower-single null
USN	Upper-single null
DN	Double null
HFS	High-field side
LFS	Low-field side
DS	Debye sheath
MPS	Magnetic presheath
NRA	Nuclear reaction analysis
SIMS	Secondary ion mass spectrometry
PIC	Particle-in-cell method
OSM	Onion-skin model
ADAS	Atomic Data and Analysis Structure
MD	Molecular dynamics
BCA	Binary collision approximation
HMM	Homogeneous mixing model

1. Introduction

Several decades of research have been carried out to develop a reactor that produces net energy from thermonuclear fusion of hydrogen isotopes. This work is about to culminate in the construction of ITER, a tokamak-type magnetic-confinement device that is designed to achieve burning plasma conditions, producing 10 times more energy than that which is consumed for heating the fuel [7]. Among the key issues to be tested in ITER is the viability of plasma-facing materials under the high, reactor-relevant power and particle fluxes reaching the walls. Long-term operation of a tokamak reactor requires a design which minimizes the erosion of the wall elements. For this reason, a thorough understanding of the physical mechanisms controlling the behaviour of the plasma boundary and plasma-wall interaction processes is needed. This thesis contributes to this understanding based on results from our present devices and their numerical interpretation.

Before discussing the physics of plasma-wall interaction, it is useful to describe the tokamak plasma geometry. Tokamaks are toroidally shaped plasma devices in which the motion of charged particles is constrained by magnetic fields. Because of the Lorentz force, charged particles gyrate around magnetic field lines with a radius known as the *Larmor radius*, r_L. Here, $r_\mathrm{L} = mv_\perp/qB$, where m, q and $v_\perp$ are the mass, charge, and perpendicular velocity[1] of the particle, respectively, and B is the magnetic field strength. In a tokamak, external coils are used to create a strong toroidal magnetic field, B_ϕ, which results in $r_\mathrm{L} = 0.1$–10 mm for the light fuel ions [9]. However, the plasma is not confined by B_ϕ alone. The toroidal geometry leads to gradients in the magnetic field strength, which give rise to *cross-field drifts*. Further drifts

[1] Throughout this thesis, *perpendicular* and *parallel* are with respect to the total magnetic field.

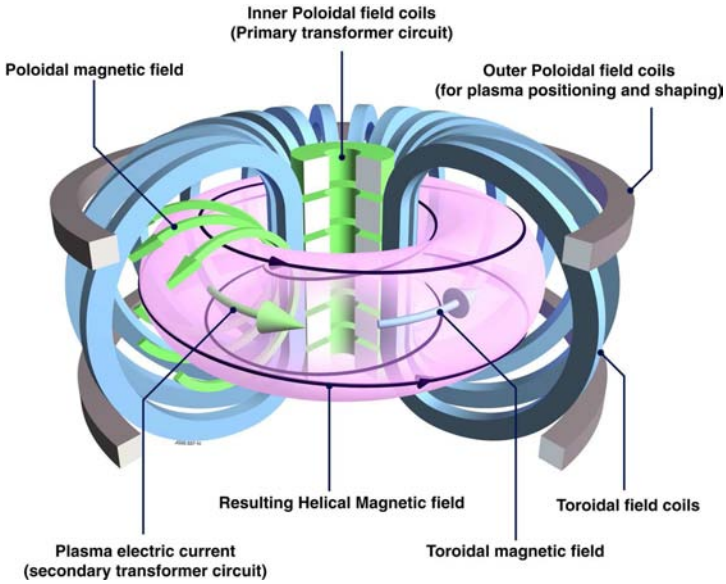

Figure 1.1: Helical magnetic field lines in a tokamak. Figure courtesy of EFDA-JET [8].

arise because of resulting electric potential variations. To keep the plasma stable, a toroidal current is driven through the plasma to create a weaker poloidal magnetic field, B_θ. The resulting helical magnetic field lines, see Figure 1.1, lie on a nested set of tubular surfaces called *magnetic flux surfaces*.

Despite the strong helical magnetic field, the confinement in a tokamak is imperfect, and plasma-wall contact occurs. The Coulomb interaction between charged particles and the cross-field drifts and turbulent motions lead to transport of energy and particles across the magnetic flux surfaces, so that they eventually reach the outermost flux surfaces and the first wall of the machine. The magnetic field lines intersecting the solid surfaces are termed *open*, to distinguish them from the *closed* magnetic field lines which define the region of confined plasma. Particles and energy which are transported radially across the *last closed flux surface*, LCFS, will be conducted and convected along open field lines to the plasma-facing components, PFCs. This causes unavoidable *plasma-wall interaction*, PWI.

PWI processes affect both the material surfaces and the plasma conditions, with potentially severe consequences for the operation of a fusion reactor. The power and particle fluxes tend to erode the wall material, reducing the PFC lifetime. The released material is ultimately re-deposited, changing the surface material composition of the PFCs or, in the case of carbon, accumulating in regions remote from plasma impact. In the plasma, eroded impurity atoms are ionized, diluting the fuel and producing energy losses through radiation. Elements with low charge number, Z, may radiate efficiently in the vicinity of the material surfaces, with the beneficial consequence that the area over which power is spread on PFCs is increased. For this reason, impurities are sometimes deliberately injected into the plasma boundary. However, on closed flux surfaces the impurities, particularly with high Z, can lead to prohibitively large energy losses from the main plasma, severely deteriorating the fusion performance. It is therefore important to achieve efficient screening of impurities from the main plasma.

Even in the case of negligible erosion of the PFCs, the boundary plasma conditions are strongly affected by the particle and energy sink produced by the plasma-wall contact. Because of the difference in thermal velocity between electrons and ions, an electric potential difference is created at the plasma-wall interface, producing an electric field which extends throughout the boundary plasma. The impinging plasma ions recombine with electrons at the wall surface, so that neutral atoms are released into the edge plasma where they radiate, collide with the ions, and become ionized. These processes yield various sinks and sources of plasma particles, momentum and energy, which in turn modify the power and particle fluxes reaching the material surfaces and thus affect the erosion of the wall components.

The various boundary plasma processes are known to be influenced by the geometry of the plasma and the PFCs. Instead of defining the LCFS by a limiting wall element, a concept known as a *divertor* has been developed over the years. A divertor is formed by running an external current, I_{d}, parallel to the plasma current, I_{p}, so that an additional poloidal magnetic field component is formed. The outermost field lines become bent and connect with the divertor targets, defining a region called the *scrape-off layer*, SOL, depicted in Figure 1.2. The divertor design aims at dispersal or reduction of the power arriving from the main plasma and efficient particle exhaust.

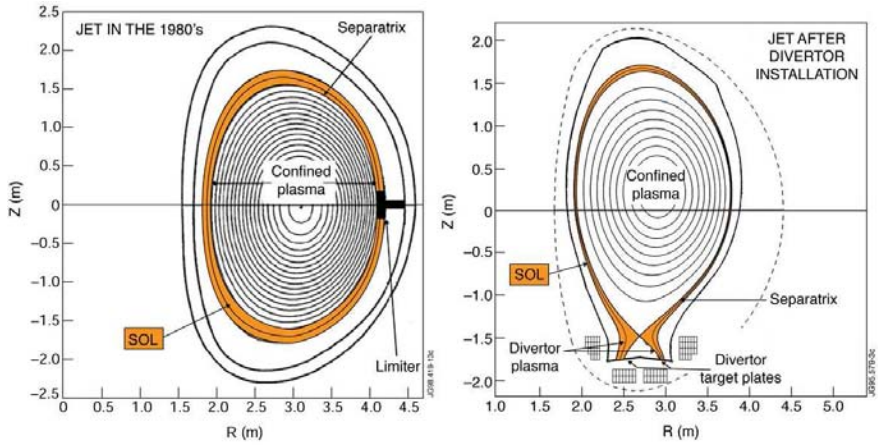

Figure 1.2: The principles of limiter and divertor configurations, with a poloidal cross-section of the torus. Figure courtesy of EFDA-JET [12].

The key objectives are, therefore, screening of impurities and compression of neutrals in the divertor region that is remote from the main plasma.

The introduction of the divertor concept led to the discovery of an improved plasma confinement regime in the 1980s. After applying high external heating to the plasma in the ASDEX tokamak, steep radial gradients of plasma temperature, T, and density, n, were observed to form at the LCFS [10]. This *pedestal* was a result of a transport barrier formed at the plasma edge, leading to a *high-confinement*, H-mode plasma that is nowadays regularly obtained in most major tokamaks. Such high-performance plasmas can lower the cost of energy production by reducing the required plasma volume in a fusion reactor, but they are typically characterized by so-called *edge-localized modes*, ELMs [11]. The ELMs are a magnetohydrodynamic phenomenon and are manifest as periodic collapses of the pedestal, which lead to abrupt bursts of particles and energy from the main plasma towards the first wall. Because of their high power flux densities, these bursts, if not controlled, will be a major concern for the endurance of the PFC materials.

Only few materials have been identified which could be used during burning plasma operation; the ones that will be tested on the various PFCs in ITER are tungsten, beryllium and carbon [13]. From this selection, carbon

has the most attractive thermomechanical properties, as it withstands large heat loads without melting. Furthermore, it can be tolerated in larger concentrations in the core compared to high-Z impurities like tungsten. The major problem associated with carbon is the formation of hydrocarbon layers which significantly increase the accumulation of radioactive tritium in the PFCs. Because of nuclear safety regulations which restrict plasma operation after $\sim$1 kg of in-vessel tritium inventory is reached [13], carbon is excluded as a wall material during the second operation phase of ITER when D-T fuel will be used. In a reactor, a further problem arises because of the reduction of thermal conductivity of carbon after neutron irradiation. Tungsten is a high-Z material which does not erode if the temperature at the plasma-wall boundary can be kept low. In future high performance devices, however, there is a risk that transient heat loads modify the surface morphology or cause prohibitively large melt layer losses on the tungsten PFCs. For these reasons, and because of the considerable experience gained by the world fusion community with carbon, it is still a widely studied PFC material option.

A thorough understanding of divertor physics and plasma-wall interaction is required to optimize the divertor design and discharge scenarios for future devices. Because of the variety, complexity, and non-linearity of boundary plasma processes, numerical simulations are needed to interpret experimental results and to extrapolate them to future devices. Several sophisticated code packages have been developed by the community for this purpose, and the code solutions have been compared with experimental measurements from existing devices. Unfortunately, these comparisons have revealed several alarming discrepancies, demonstrating that our understanding of the plasma boundary processes is not yet complete [5, 14]. In order to assess the possible deficiencies, it is necessary to validate the simulations against a sufficient range of experimental conditions.

The work presented in this thesis focuses on benchmarking of plasma boundary simulations, using well-established code packages that are used within the community both to interpret and to predict experiments. These include the SOLPS5.0 code package [15], for modelling the SOL and divertor plasma; the ERO code [16], for following the local transport, erosion and deposition of impurities; and the ASCOT code [17], which is used in this work to follow guiding-centre particle orbits in the SOL. The various simulation tools are

chosen based on the best available description of the investigated physical processes in the codes, combined with their feasibility for extensive parametric studies. The device used for obtaining the detailed experimental data is the ASDEX Upgrade tokamak, which is close to a geometrically scaled-down version of ITER [18].

The thesis work investigates in particular the assumptions required to reproduce the measured divertor plasma conditions in simulations, and the mechanisms affecting the erosion, transport and deposition of carbon on divertor surfaces. The two topics are tightly linked to each other, as the PWI processes influence the divertor plasma and the divertor conditions determine the erosion rates and affect the transport of impurities. Carbon is chosen as an impurity, because there exists a uniquely informative way of investigating its migration experimentally, by means of injecting isotopically labelled methane, $^{13}CH_4$, into the plasma [19].

The experiments investigated form the most extensive set of divertor $^{13}CH_4$ injection experiments in an ITER-like wall and plasma geometry up to date. A detailed study of the migration mechanisms is carried out by integrating the solutions from plasma fluid simulations (SOLPS5.0) with localized impurity migration simulations (ERO). In the course of the thesis work, the effect of cross-field drifts was included for the first time in the SOLPS5.0–ERO simulations. The thesis work includes a detailed comparison of the SOLPS5.0 plasma solutions against plasma discharges in *low-confinement* mode (L-mode). This type of thorough code-experiment benchmarking is carried out for the first time against ASDEX Upgrade discharges in low density and using both forward and reversed magnetic field configuration. Furthermore, a comparison between the plasma fluid solutions and electron following simulations is carried out by performing ASCOT simulations, which for the first time use a plasma background from SOLPS5.0 simulation.

The content of the thesis work is further described in the following sections. Section 2 discusses the relevant physical phenomena investigated in this thesis. Section 3 describes the experimental work which has been carried out, with reference to studies made on other tokamaks. In section 4, the code packages used in this work are presented. Section 5 summarizes the results obtained in Publications I–V. Finally, conclusions are presented in section 6.

2. The plasma boundary in divertor tokamaks

2.1 Scrape-off layer and divertor plasma

Definition of the boundary regions

Before discussing the physical processes which define the conditions in the plasma boundary, it is useful to first briefly introduce the most common magnetic geometries and the various boundary regions in divertor tokamaks.

Several external currents are typically used to shape the plasma and to create one or several *X-points*, where $B_\theta = 0$. In this type of divertor configuration, the LCFS is called the *separatrix*, as it separates the core plasma from the open field lines. The various magnetic topologies are labelled according to the number and locations of these X-points. If the separatrix contains only one X-point, the topology is defined either a *lower-single null*, LSN, or an *upper-single null*, USN. Two X-points can be formed simultaneously on the separatrix to create a *double-null* configuration, DN. However, power exhaust is not significantly facilitated with the DN configuration, and the machine costs are higher than with single null topologies. ITER will use a LSN topology, with an upper secondary X-point located outside the LCFS or inside the wall elements. A similar configuration was used in the ASDEX Upgrade experiments discussed in this thesis.

Figure 2.1 shows the magnetic field lines in one of the ASDEX Upgrade discharges investigated in this work. In ASDEX Upgrade, a *forward* magnetic field configuration is normally used, with $\mathbf{B} \times \nabla \mathbf{B}$ towards the active divertor.

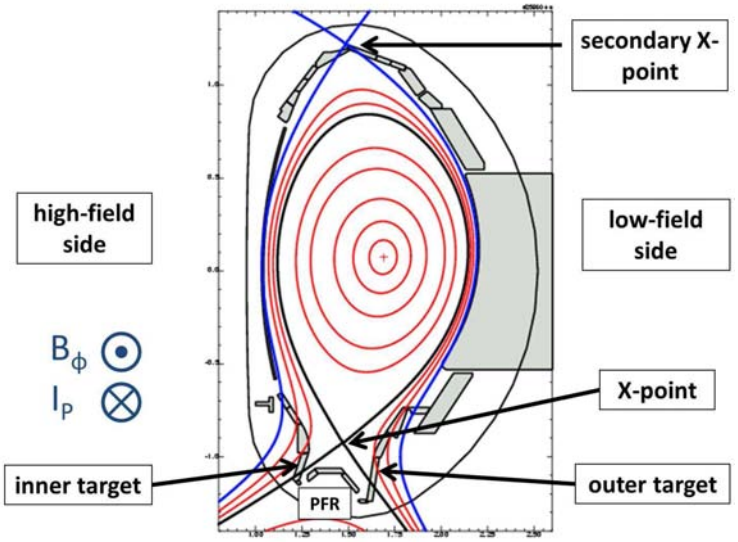

Figure 2.1: An example of a LSN magnetic configuration in ASDEX Upgrade. Directions of B_ϕ and I_p are shown for the forward field configuration.

The corresponding directions of B_ϕ and I_p are indicated in the figure. The open field lines belong to the SOL, recall Figure 1.2, excluding the region in between the two legs of the separatrix, which is called the *private-flux region*, PFR. It is customary to refer to the region of the SOL above the X-point as the *main SOL*, or *upstream*, whereas the whole region below the X-point is typically referred to as the divertor plasma, or simply the divertor.

A distinction is made between the inner and outer divertor targets, which are on the high- and low-field sides of the vessel, HFS and LFS, respectively. The magnetic flux surfaces are more compressed on the LFS compared to the HFS, which is caused by the Shafranov shift [20]. Because of the variation in B_θ, the radial spacing of the flux surfaces increases on the way to the divertor targets. This *flux expansion* increases the plasma-wetted area of the targets, reducing the target power flux densities.

Sheath potential drop at the targets

At the plasma-material boundary, a strong electric field exists which affects the plasma conditions throughout the open field line region. The electric field arises because the electrons have a significantly smaller mass than the ions and thus have a higher thermal mobility. Since the plasma must remain quasineutral, any material surface in contact with it will initially receive a higher flux of electrons than ions, which charges the surface negatively. The potential difference between the plasma and the solid surface will begin to repel the electrons and attract the ions. Assuming that the surface is electrically floating, the ion and electron fluxes will adjust so that no net current is received by the surface, but an *ambipolar flow* occurs. As a result, a potential drop is formed within a thin layer close to the surface called the *sheath*, in which the quasineutrality of the plasma is violated: $n_\mathrm{i} > n_\mathrm{e}$[1]. In the simplest case, the thickness of the sheath is characterized by the Debye length, $\lambda_\mathrm{D} = \sqrt{\epsilon_0 T/n_\mathrm{e} e^2}$, where ϵ_0 is the vacuum permittivity and e is the elementary charge. For typical tokamak divertor target plasma parameters, $\lambda_\mathrm{D} << 0.1$ mm.

Because of the large toroidal magnetic field component in tokamaks, the magnetic field lines tend to have large incidence angles on the divertor target surfaces: $\psi = 86$–90 degrees[2]. In such conditions, the sheath potential drop has been shown to occur in two qualitatively different regions [21, 22]: in the electrostatic *Debye sheath*, DS, and in a quasineutral *magnetic presheath*, MPS, see Figure 2.2. As described above, the DS exists closest to the target, with thickness $\sim \lambda_\mathrm{D}$, whereas the MPS may extend up to a few ion Larmor radii. For typical target conditions, $r_\mathrm{L} \sim 1$ mm. In the case of a very large incidence angle of $\mathbf{B}$, most of the potential drop occurs in the MPS, where the resulting electric field, $\mathbf{E}_\mathrm{mps}$, modifies the particle trajectories as shown in Figure 2.2. Regardless of how the sheath is formed, the total potential drop, V_sh, is approximately [23]:

$$\frac{eV_\mathrm{sh}}{T_\mathrm{e}} \sim 0.5 \ln\left[\left(2\pi\frac{m_\mathrm{e}}{m_\mathrm{i}}\right)\left(1+\frac{T_\mathrm{i}}{T_\mathrm{e}}\right)\right]. \tag{2.1}$$

[1] Throughout the rest of this thesis, the subscripts i and e refer to ions and electrons, respectively.

[2] Incidence angle is given here with respect to the surface normal.

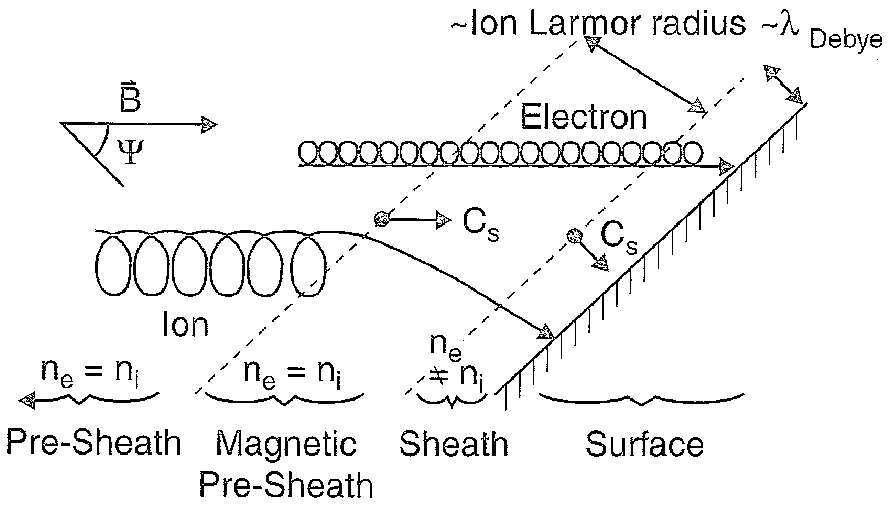

Figure 2.2: Ion and electron trajectories in the various sheath regions near the target surface. Reproduced from [23].

This expression excludes corrections due to secondary electron emission and particle reflection. V_{sh} is, thus, determined by the electron and ion temperatures at the targets (expressed in eV throughout this overview).

The presence of the sheath has several consequences for the divertor and SOL plasma, which to a first order do not depend on the fractions of potential drop occurring in the MPS and DS [23]. The potential drop is not strictly limited to these two regions; a weak *presheath* potential drop, $eV_{\mathrm{ps}} \sim -0.7T_{\mathrm{e}}$, also exists along the field lines in the SOL and PFR [23]. The plasma flow is accelerated in this presheath region in the direction towards the target. The flow speed, u, is often described by normalizing to the flow Mach number, $M = u/c_{\mathrm{s}}$, where c_{s} is the *ion sound speed*:

$$c_{\mathrm{s}} = \sqrt{\frac{ZT_{\mathrm{e}} + \gamma T_{\mathrm{i}}}{m_{\mathrm{i}}}}. \tag{2.2}$$

Here, Z is the ion charge and γ can have values in between 1 and 3, depending on the plasma collisionality and magnetic geometry [24]. At the entrance to the MPS, the flow velocity must be equal to or higher than the ion sound speed, $M \geq 1$, a condition known as the *Bohm criterion* [25].

In addition to the effect on the flow velocity, the sheath influences the electron and ion temperatures in the SOL plasma. The total energy transmission through the sheath per ion–electron pair is 7–$8T_e\Gamma_{se}$, where Γ_{se} is the parallel ion flux at the sheath entrance [23]. However, due to the repulsive electric field, only those electrons with energies above eV_{sh} at the sheath entrance are lost to the target, so that the electron energy distribution is depleted from its high-energy tail. The sheath electric field transfers part of the electron energy to the ions, which are accelerated. Therefore, the electron population in the SOL is cooled by the sheath.

The SOL is often modelled using a fluid approach, which breaks down in the MPS and DS regions. Therefore, it is customary to treat the sheath by applying boundary conditions for the parallel velocity, heat transmission and plasma potential at the sheath entrance. Possible deviations from the above classical models have been identified in the past, arising from cross-field drifts and their gradients [26, 27], non-Maxwellian electron velocity distributions [28], surface roughness [29], various inelastic and collisional processes in the MPS [28, 30], and magnetic fields almost parallel to the surface [31] (see also references in these papers). Simulations using, e.g., the particle-in-cell method, PIC [32, 33], can be performed to obtain a more accurate description of the plasma-wall transition layer and to verify the boundary conditions. Such studies were, however, excluded from this thesis work.

Power and particle transport in the SOL

One of the primary objectives of the divertor is to disperse or reduce the power that is transported from the main plasma into the SOL [34]. When volumetric particle, energy and momentum losses are small, the power loads on the divertor targets are determined by the competition of parallel and radial transport processes. The flows of energy and particles in these two directions determine the *radial decay lengths*[3] of parallel power fluxes and plasma density in the SOL, which characterize the thickness of the SOL plasma. In the following, the discussion is restricted to parallel and radial transport, neglecting, for the moment, the effect of flows in the third, *diamagnetic* direction [35].

[3]The decay length is equal to the gradient scale length, e.g. $\lambda_{q_\parallel} = q_\parallel / \nabla_\perp q_\parallel$.

Particle transport is sensitive to the distribution of particle sources and sinks in the SOL. The solid surfaces in contact with the magnetic field lines are sinks for the plasma particles. Ions and electrons recombine at the targets and are released back into the plasma as neutrals, which become ionized and produce particle sources. Therefore, unlike the energy source which is distributed along the separatrix, the particle source in the SOL is influenced in addition by these ionization zones. In between the sources and the sinks, there is net transport of particles along the field lines. Energy is transported along the field lines either by conduction or convection. Convection carries energy particularly in between the ionization sources and the targets [35]. The conducted parallel heat flux, $q_{\parallel}$, in a collisional plasma is given by

$$q_{\parallel s} = -\chi_{\parallel s} \nabla_{\parallel} T_s, \tag{2.3}$$

where s refers to either electrons or ions and $\chi_{\parallel}$ is the parallel heat conductivity [36]. The latter depends on the species mass and is significantly higher for electrons than for ions. Furthermore, $\chi_{\parallel \mathrm{e}}$ increases with temperature and decreases with collisionality:

$$\chi_{\parallel \mathrm{e}} \propto \frac{T_{\mathrm{e}}^{5/2}}{n_{\mathrm{e}}} \propto \lambda_{\mathrm{coll,e}} v_{\mathrm{th,e}}, \tag{2.4}$$

where $\lambda_{\mathrm{coll,e}}$ and $v_{\mathrm{th,e}}$ are, respectively, the electron collision mean-free path and thermal speed [35, 37].

The parallel transport tends to bring particles and energy directly to the divertor targets, but competitive transport in the radial direction broadens the power loads. Radial transport of both particles and heat in the SOL is observed to be anomalously high in all tokamaks, exceeding the classically expected transport levels, which include collisions and drifts, by even several orders of magnitude. It is now universally accepted that this anomalous transport is caused by plasma turbulence involving density, temperature, and potential fluctuations [38, 39]. It is intermittent in nature and consists of filamentary structures which travel at high speeds in the radial direction, enhancing radial transport. Observations made in the past have indicated that the cross-field SOL transport increases with plasma collisionality and varies in the radial direction, increasing towards the outer SOL [40, 41].

To predict the conditions in future devices, a proper description of the transport levels is required. The largest uncertainties involve the turbulent radial transport, for which no scaling is yet available. It is a common procedure in 2D SOL modelling, which typically treats the plasma as a fluid, to describe the radial transport by means of effective radial velocities or diffusivities [35]. The radial transport coefficients are adjusted by comparing the simulation results against the experimentally measured temperature and density profiles in various devices and conditions. Recently, a collisionality-dependent formulation of radial transport was attempted in edge fluid simulations, with promising results with respect to reproducing observed trends in divertor conditions as a function of plasma density [42].

Finally, it should also be noted that there are uncertainties in the parallel transport. It has been suggested that fluctuations could affect transport in the parallel direction [35, 43]. Furthermore, the SOL collisionality is often insufficiently high to ensure the validity of the collisional heat conduction equation (2.3), which gives $|q_{\|e}| \to \infty$ when $\lambda_{\mathrm{coll,e}} \to \infty$. This last question has been studied in detail in this thesis work and will be discussed further in Section 4.1.

Divertor regimes

Neutrals recycling at the wall elements produce various particle, momentum and energy sinks and sources in the SOL plasma. The dominant volumetric power losses due to neutrals result from radiative de-excitation (line radiation), charge-exchange reactions, and dissociation and ionization reactions. The divertor design aims to confine these power losses to the divertor volume, so that large parallel temperature gradients can be produced in the SOL. This allows the existence of a hot core plasma together with tolerable power loads at the divertor targets.

Various divertor operation regimes can be identified according to the level of recycling at the divertor targets. At the lowest plasma densities and, hence, the highest divertor plasma temperatures, obtained by minimal fuelling, the walls will initially absorb part of the impinging neutrals, acting therefore as an additional 'pump'. Over a certain time period, which depends on

the surface material and discharge density, the walls become fully saturated by the neutrals. The neutrals are then released from the walls with fluxes identical to the impinging ion fluxes, so that 100% recycling of the plasma occurs. In typical tokamak conditions, the neutrals ionize close to the targets and add to the particle fluxes arriving from the main SOL.

When the SOL plasma density is low, the recycling sources and the volumetric power losses in the divertor are small. In such conditions, there are no significant temperature gradients along the field lines, yielding a hot target plasma, with typically $T > 20$ eV. The power is lost in this regime mostly by the heat transmission through the sheath. Such conditions define a *low-recycling* divertor plasma regime, also known as the *sheath-limited* regime.

As the discharge density is increased, the particle fluxes and, consequently, recycling sources at the targets increase and the divertor plasma becomes more dense and collisional. Due to finite parallel heat conductivity, equation (2.4), parallel temperature gradients are formed in the SOL (equation (2.3)). Volumetric energy losses reduce the temperature at the targets further. The conservation of total pressure along the field lines requires that the drop in the target temperature is accompanied by an increase in target density. Unlike in the sheath-limited regime, where the target density, n_t, increases linearly with the upstream density, n_u, the dependence is now approximately cubic, $n_\mathrm{t} \propto n_\mathrm{u}^3$. Such conditions define a *conduction-limited regime*, also known as the *high-recycling* regime.

Edge plasma modelling has attempted to reproduce the various experimentally observed divertor plasma regimes. Qualitatively the reduction of T_e with increasing recycling is straightforwardly obtained, but even the most sophisticated 2D simulations available have failed to match quantitatively the observed high-recycling conditions at the targets [5,14]. In a detailed study of a medium-density ASDEX Upgrade discharge, the simulations yielded cooler and denser divertor plasma conditions compared to experiments [1,44,45]. It was suggested that in medium plasma collisionality, the commonly used fluid description would fail as a consequence of kinetic effects [14]. In particular, the presence of an increased supra-thermal electron population in the divertor plasma could increase the target heat loads [46] and explain part of the discrepancies with temperature measurements [47]. However, the inability

of the codes to reproduce measurements over a wide range of collisionalities [5] requires that further physics ingredients lacking in the analysis are considered.

By far the most distinct discrepancies have been observed when modelling divertor plasmas which, unlike the ones described above, are no longer *attached* to the divertor targets. Experimental observations show that as the temperature at the target drops below a few eV, the fluxes of electrons and ions on the divertor targets usually begin to decrease, despite the increasing density of the discharge and an increasing radiation measured in the divertor [48]. This process is known as *divertor detachment*, and is defined by the necessary condition that a loss of total pressure occurs along the field lines from upstream down to the target. Detachment is considered to occur as a result of increasing volumetric energy and momentum losses, including low-temperature phenomena such as volume recombination and ion-neutral friction [23, 49]. The roll-over in divertor particle fluxes with increasing plasma density is observed also in simulations [42]. However, several experimental features, including the measured plasma density threshold for divertor detachment, cannot be reproduced by our present models [50, 51]. This implies that the detachment process is both quantitatively and qualitatively not understood [51]. The collisionless electrons mentioned earlier have been suggested as a player in the detachment process, by affecting the ionization of neutrals [52].

High recycling and detached plasmas are essential for reducing the power loads on the divertor targets. Detachment of the divertor strike points will be mandatory in future fusion reactors with high parallel power fluxes. However, full detachment of the divertor plasma reduces the divertor *closure*, decreasing the compression of neutrals and the screening of impurities. The implications of the latter for future reactors depend on the use and behaviour of injected impurities. Because of the reduction in plasma confinement and the risk of disruptions at high plasma densities associated with full detachment [53], scenarios with only partially detached divertor plasmas are currently envisaged for future devices like ITER. In addition to neutrals, low-Z impurities can significantly increase the volumetric energy losses in the divertor and reduce the density threshold for detachment. In most present-day tokamaks, the erosion of wall elements yields a substantial number of im-

purities which dominate radiative losses in the edge plasma. When using high-Z wall elements, the lack of intrinsic impurities must be compensated by injecting external impurities into the divertor. Candidate species for such *impurity seeding* include N, Ne and Ar [54].

In-out asymmetries

In conventional divertor tokamaks, which often use a LSN topology with $\mathbf{B} \times \nabla\mathbf{B}$ direction towards the divertor, the measured power and particle fluxes are often asymmetrically distributed between the inner and outer target. In these scenarios, the inner target is typically in a higher recycling regime than the outer, and the outer target receives the highest power fluxes. These *in-out asymmetries* are observed to vary between different machines. Therefore, when looking for an explanation the first considerations include effects of the magnetic geometry on the poloidal distribution of the power source. Because of the toroidal geometry, the flux surfaces have a wider area on the LFS compared to the HFS of the tokamak, so that larger fractions of power are transported across the LFS separatrix. Furthermore, if the cross-field transport is assumed to be proportional to radial gradients, the Shafranov shift causes the power transport to be strongest near the outer midplane [23]. There are also indications of *ballooning*-type cross-field transport, which leads to larger radial transport on the LFS [55–58]. As a result, the power from the core is preferentially transported to the outer target.

The aforementioned effects on the divertor plasma asymmetries do not depend on the direction of the tokamak magnetic field. However, it is experimentally observed that the target conditions are modified by reversal of the toroidal magnetic field (see e.g. [59] and references therein). This is thought to occur mainly because of cross-field drifts, which influence both the power and particle transport in the SOL [60]. When considering the asymmetries, important examples of these drifts are the gradient drift,

$$\mathbf{v}_{\nabla\mathbf{B}} = \frac{1}{2} r_{\mathrm{L}} \frac{\mathbf{B} \times \nabla\mathbf{B}}{B^2} v_{\perp}, \tag{2.5}$$

and the $\mathbf{E} \times \mathbf{B}$ drift,

$$\mathbf{v}_{\mathbf{E}\times\mathbf{B}} = \frac{\mathbf{E} \times \mathbf{B}}{B^2}. \tag{2.6}$$

Here, both drift velocities are expressed in the form that applies to the individual guiding centres of the plasma particles, and should not be confused with the respective fluid expressions [60].

The gradient drift is in the opposite directions for electrons and ions, and therefore drives charge separation. Due to the toroidal geometry, tokamaks have an intrinsic non-zero $\nabla\mathbf{B}$, which yields gradient drifts in the vertical direction. This is compensated by a return flow along the field lines, known as the *Pfirsch-Schlüter flow*. The $\mathbf{E}\times\mathbf{B}$ drift, on the contrary, is independent of the charge and mass of the plasma particle, and its direction and magnitude can vary significantly with the plasma conditions. A poloidal electric field, $\mathbf{E}_\theta$, such as that formed due to the pre-sheath potential drop, will cause a radial $\mathbf{E}_\theta \times \mathbf{B}$ drift. In addition, strong radial temperature gradients can be encountered in the SOL, in which case radial electric fields, E_r, are produced, leading to $\mathbf{E}_\mathrm{r}\times\mathbf{B}$ drifts in the poloidal direction. The latter can drive pressure asymmetries in between the two targets, which are compensated by a return parallel flow in the main SOL.

Present-day edge simulation codes can take into account the effects of the magnetic geometry, ballooning-like transport, and the cross-field drifts. However, they typically fail to reproduce simultaneously both the power and the particle asymmetries between the divertor targets [5,51,61]. In addition, large discrepancies are observed when comparing the measured parallel ion flows in the main SOL to those modelled by 2D edge codes. While the experiments show significant main SOL flows with $M \sim 0.5$ when $\mathbf{B} \times \nabla\mathbf{B}$ direction is towards the divertor [58, 62], the parallel ion flows calculated by the codes are typically 2–10 times smaller [63–65]. This has been suggested to be due to mismatches in the modelled and measured radial electric field in the SOL; the calculated Pfirsch-Schlüter flows are higher when using measured values of E_r compared to using the simulated values of E_r [66, 67]. The underestimation of main SOL E_r by the codes is thought to result from discrepancies between modelling and experiments in the two divertors [14].

2.2 Plasma-material interaction

Erosion mechanisms

A solid surface will be subject to *physical sputtering* by the plasma and neutrals, provided that a sufficient amount of energy is transferred to an atom in the near surface layer by the impinging particles [68]. A quantitative measure of sputtering is given by the *sputtering yield*, Y_{phys}, which is the average number of particles released per projectile ion/atom. The minimum transferred energy required to sputter an atom is equal to the surface binding energy, E_{B}, which for the primary ITER PFC material options ranges between 3.38 eV (Be) and 8.8 eV (W). Collisions within the lattice can, however, transfer only a fraction of the incident energy, and the energy transfer process typically involves a collision cascade. Therefore, a larger impact energy compared to E_{B} is required for physical sputtering of the target material. This energy dependence is characterized by the *threshold impact energy*, E_{th}, below which the sputtering yield decreases rapidly [69].

The energy transfer in collisions depends on the projectile/target mass ratio, and is most efficient for particles with similar masses. Incidence energies above several hundreds of eV are required for the light hydrogen isotopes to sputter heavy elements such as W, whereas lighter materials such as carbon can be sputtered by the plasma fuel with E_{th} below 50 eV. High-Z materials would thus be favourable, if the plasma temperature close to the material surfaces could be kept continuously low. However, significant erosion may still occur due to energetic particles originating e.g. from charge exchange reactions. Because of the dependence of sputtering on the mass ratio, solid surfaces are most efficiently eroded by the heavy plasma impurities originating from the wall itself or from impurity seeding. Furthermore, the high-Z impurities can become multiply charged and accelerated to high impact energies by the sheath potential, which can lead to significant self-sputtering yields [70].

Particles with high impact energies can penetrate deep into the lattice, which decreases their efficiency in transferring energy to the surface atoms. Therefore, Y_{phys} decreases towards high energies. When the solid surfaces have

a perfect crystalline structure, the physical sputtering yield increases with the incidence angle of the projectile, since more energy can be transferred to the near surface layer for grazing incidence compared with normal incidence. In a typical tokamak divertor, however, topography effects such as the surface roughness of the material tend to diminish the angular dependence of the sputter yield [71]. Furthermore, the magnetic presheath tends to bend the ion trajectories so that the ions impinge with angles close to the surface normal, despite the oblique magnetic field angle (recall Figure 2.2).

Physical sputtering is a generally well understood process, and the sputtering yields have been evaluated for many projectile/target combinations based on computer simulations and laboratory measurements [72–74]. The main uncertainties are related to the effects of the surface topography and the variations of E_B for solids with more than one material component [75]. The uncertainties of the sputter yield are largest for impact energies close to the threshold energy, where the yield varies rapidly [69, 76].

Certain elements can undergo enhanced erosion because of their chemical affinity with hydrogenic isotopes or oxygen impurities. Carbon in particular is known to be subject to significant *chemical erosion*, due to the formation of hydrocarbon molecules. In comparison with physical sputtering, chemical erosion is a much more complicated process, and its analysis relies heavily on measurements made in accelerators, linear devices and tokamak edge plasmas [77]. The latter are needed to obtain data in tokamak-relevant ion flux and impact energy range. However, there are uncertainties in the interpretation of the limited measurements that are feasible in tokamaks, including, for example, spectroscopy (see Section 3.1). Furthermore, variations in the surface material composition are not accounted for when collecting the data from tokamak experiments. Consequently, a considerable scatter is observed in the chemical erosion yields given in literature, yielding a notable uncertainty for modelling which requires this data as input.

The following processes have been identified to be involved in the chemical erosion of carbon by low-energy hydrogen [78]. Carbon atoms are hydrogenated in the lattice, which is known as *reaction of thermalized ions*. At surface temperatures avove 400 K, thermal release of CH_3 radicals takes place, whereas at temperatures above 600 K, the recombinative release of H_2

molecules begins to reduce the chemical erosion yield [79, 80]. This thermal reaction can be *enhanced by radiation damage*, which is caused by kinetic energy transfer from incident ions to lattice atoms. At low temperatures, no thermal release of hydrocarbons occurs. However, because of the much smaller binding energy of hydrocarbons ($E_{\mathrm{B}} \sim 1$ eV) compared with carbon ($E_{\mathrm{B}} = 7.4$ eV), incident ions can easily erode the hydrocarbons from the surface. This *ion induced desorption of hydrocarbon radicals* can release a variety of different hydrocarbon molecules [81].

Because of the low E_{B} of hydrocarbons, chemical erosion has a significantly lower energy threshold than physical sputtering. Impact energies above 50 eV are required to obtain 0.5% physical sputtering yield of carbon by deuterium [82]; the same yield of chemical erosion, Y_{chem}, is obtained already at sub-eV impact energies [81]. The chemical erosion yield for carbon has a maximum at an elevated temperature, $T_{\mathrm{max}} = 700$–900 K, and decreases at temperatures higher than T_{max} due to the release of hydrogen molecules. Measurements carried out in various tokamak experiments show that at high ion flux densities, Φ, the erosion yield decreases according to $\Phi^{-0.54}$ [83]. The inclusion of flux dependence in chemical erosion led to an order of magnitude reduction in the past predictions of target erosion in ITER for the case of carbon high heat flux divertor targets [84].

Physical sputtering and chemical erosion are known as continuous erosion mechanisms on a solid surface in contact with plasma. Several transient erosion mechanisms have been identified in addition. Off-normal events such as plasma disruptions and ELMs can abruptly increase the heat loads on the solid surfaces, leading to melting of metal PFCs and sublimation of carbon PFCs [13]. The former in particular presents a serious concern for future tokamak operation, since macroscopic melting of metallic surfaces can inject large quantities of impurities into the confined plasma and radically deform the topology of the melted component [85, 86]. Exposed tile edges receive high heat loads, which can generate *hot spots* even under steady discharge conditions. In addition, microscopic surface deformities or regions of poor electrical conductivity can trigger *electrical arcs* – high currents of short duration, arising from the sheath potential between the plasma and the PFC. Arcs can cause fast evaporation and erosion of the PFC material even in the absence of transient events [87]. However, in recent studies at ASDEX

Upgrade a correlation between ELMs and arcing was observed [88]. These discontinuous PWI processes are, however, outside the scope of this thesis.

Deposition on material surfaces

The eroded impurities will eventually return to the material surfaces, where they may be reflected back to the plasma or become re-deposited on the surface. The *reflection probability*, R_{prob}, gives the probability for an incident particle to be reflected from the surface; an often used complementary measure of reflection is the *sticking probability*, $S_{\mathrm{prob}} = 1 - R_{\mathrm{prob}}$. The reflection probability varies for different projectile/target combinations and depends on the incidence angle and energy of the projectile. In general, R_{prob} decreases with increasing impact energy, as the particles are likely to penetrate deeper into the lattice. The higher the mass ratio, $m_{\mathrm{target}}/m_{\mathrm{projectile}}$, the higher R_{prob}, since light atoms can easily bounce off the heavy surface atoms in elastic collisions. The reflection probabilities of many projectile/target combinations have been evaluated by computer simulations (see Section 4.2).

Erosion and re-deposition processes will modify the lattice structure of the substrate and can readily lead to the formation of surface layers with variable composition. This can degrade the thermomechanical properties of the PFC [89] and lead to changes in erosion yields [90]. Thick, re-deposited layers can be delaminated during plasma operation or venting of the machine, releasing particulates known as *dust*. Mobilizable dust poses a safety problem for a nuclear device, in particular if tritium is co-deposited in the layers [13]. Limited experience has been obtained of the properties of mixed materials relevant to ITER; ASDEX Upgrade has been operated with C and W simultaneously in the machine (see e.g. [91, 92]), and the combination of Be and C has been investigated in JET [93, 94]. At the time of writing, a complete upgrade of the JET in-vessel components has just been completed and operation has begun with an ITER-like wall comprising main chamber surfaces in Be and W divertor targets [95]. Hence, there are large uncertainties in the expected behaviour of the ITER PFC combination in a burning plasma environment.

In this thesis work, the deposition of carbon is studied in particular. Carbon is problematic as a PFC material because of the co-deposition of tritium with hydrocarbon molecules [96]. For this reason, carbon PFCs are planned to be used in ITER only during the operation in hydrogen and helium, when forgiving materials are needed to allow testing of various operational scenarios [97]. The behaviour of the various types of carbon layers can differ significantly; laboratory experiments indicate that the chemical erosion yield of freshly deposited hydrocarbon layers is significantly enhanced compared with bulk graphite [90]. This has been further suggested by an extensive interpretative modelling program performed for TEXTOR experiments, discussed in Section 3.2. It was concluded that a significantly *enhanced re-erosion* of the deposits must take place during the growth of the carbon layers on plasma-wetted areas [98]. This was suggested to be due to synergy effects between the plasma fuel and the hydrogen in the co-deposited layers, or due to the additional hydrogen released in dissociation of the hydrocarbon molecules [99].

The present work is further complicated by the fact that tungsten is used as the substrate material in the experiments, and knowledge of the formation of mixed C/W layers is limited. Because of the mass difference, the reflection probability is higher for C on W compared to C on C. For the same reason, the sputtering yield of carbon in a mixed C/W layer can be higher compared to a pure carbon substrate. At high fluences, carbon can form a protective layer on top of tungsten, preventing the erosion of the substrate material [75]. This is likely to occur with incidence angles close to the surface normal, rather than more glancing angles.

Impurity migration

After leaving the material surface, the eroded impurities can re-deposit locally or be transported in the plasma into more distant regions. This behaviour, known as material *migration*, ultimately determines both the net erosion of the various PFCs and the mixing of the materials. The migration of impurities depends on the PFC material properties, the edge plasma conditions, fundamental transport processes, and the magnetic field and machine geometry. These key factors involve several uncertainties and open questions, for which reason the picture of global impurity migration is very incomplete [100].

Physical and chemical erosion introduce different types of impurity sources into the plasma. Physically sputtered particles leave the surface as neutral atoms with a Thompson energy distribution according to the surface binding energy and the impacting energy of the projectile [23]. Chemical erosion of carbon can produce various thermal neutral molecular sources, including hydrocarbon radicals, methane molecules and higher hydrocarbons [78]. In each case, the released particles will follow ballistic neutral trajectories until they are ionized or dissociated by the plasma. The ionization/dissociation probability depends on the plasma parameters, and the reaction cross-sections have been evaluated for several impurities, including the various hydrocarbons [101, 102]. In the low-energy range, charge exchange reactions with fuel ions can be significant, whereas at higher energies electron impact ionization becomes important.

The ionization depth is a key parameter determining the fraction of impurities which are locally re-deposited. Ionization within a distance from the surface comparable with the impurity ion Larmor radius can lead to *prompt re-deposition* within the first gyration orbit [103, 104]. In the case of an oblique magnetic field angle, the magnetic presheath can also bring the impurity ions promptly back to the material surface from within a few r_{L} [105]. Prompt re-deposition is expected to be more important for the heavy, high-Z elements which ionize rapidly and have a larger r_{L} compared to low-Z elements like carbon. These processes are related to the *local-scale* migration, which determines the net erosion of PFCs [19].

If the impurities are not promptly re-deposited, they will leave the surface and be subject to the various boundary plasma processes. Neutral particles can travel significant distances in regions where the ionization probability is low. The ions follow more complex trajectories which can be affected by plasma flows, radial transport and cross-field drifts [100]. Furthermore, the multiple re-deposition and re-erosion processes can lead to impurity migration into remote, plasma-shadowed regions. This is particularly a problem with carbon, which can be transported in several hydrocarbon states, thus having very complex migration pathways which may lead to tritium accumulation in regions inaccessible to in-situ cleaning methods [106].

The present understanding of global impurity migration is built on experimental results from existing tokamaks [19,100], see also Section 3.2. Interpretation of various measurements in several devices has lead to the conclusion that the main wall is typically a net erosion source, from where the lost material is transported into the divertor [106]. When the ion ∇B drift direction is towards the active divertor, most of the material is observed to deposit at the inner target. It has been suggested that main chamber flows and an $\mathbf{E} \times \mathbf{B}$ drift through the PFR could be key factors in producing the observed erosion/deposition patterns [107, 108]. However, quantitative picture of the various mechanisms is still incomplete, and the interpretation of experiments typically lacks solid first-principle models of the transport mechanisms and redeposition processes. Therefore, continuing efforts to elucidate the migration processes on the various scale lengths are required, especially for predicting the critical plasma-wall interaction issues in future devices.

3. Experimental investigations

3.1 Measurements in ASDEX Upgrade

The studies in this thesis focus on the German divertor tokamak ASDEX Upgrade. This is a medium-size tokamak with a typical plasma major radius $R = 1.65$ m and a horizontal minor radius $a = 0.5$ m. It has been designed to investigate reactor-relevant physical processes, and a large emphasis in the scientific program is given to the study of ITER-relevant design issues, including the plasma boundary and the first wall [18]. Consequently, ASDEX Upgrade has a vertical target lower divertor geometry and a plasma shape close to the ITER configuration. In addition, it can be operated with reactor-relevant power densities; up to 20 MW external heating was used in the 2009 campaign [109].

As a part of the program priorities, ASDEX Upgrade has undergone a significant transition from a carbon machine to the only full-tungsten fusion device in the world [110]. The change of the PFCs was made stepwise from 1999 until the 2007 experimental campaign, when finally all the PFCs were tungsten-coated graphite tiles [111]. After the transition, high performance discharges could be achieved even without boronizing the material surfaces [112] to reduce the impurity content of the plasma [113], which is a very promising result regarding the full-metal material option for next-step reactors. Boronization of the plasma-facing surfaces was found to almost completely suppress low-Z edge radiation, while in the absence of boronization, low-Z radiation due to residual carbon was still observed in the divertor. During high power heating phases, radiative cooling methods by artificial impurity seeding are required to reduce

the divertor power loads to levels that are tolerable for the tungsten coatings [114].

In the context of the present work, ASDEX Upgrade experiments were conducted to investigate impurity migration via tracer ^{13}C injection and to provide the best characterization of the SOL and divertor plasma conditions by diagnostic measurements. The tracer experiments are discussed in Section 3.2, while a brief overview of the plasma characterization is given here.

Validation of the SOL and divertor plasma simulations against experiments requires good diagnostic coverage of the crucial boundary plasma regions. These include the main SOL, which is diagnosed in ASDEX Upgrade at the outer plasma midplane, and the two divertor legs. The key parameters for determining the various divertor regimes are the electron temperature and the plasma density and/or the ion flux density, which are measured in all these locations. To enhance the spatial resolution of the measurements, the positions of the outer major radius and divertor strike points are typically scanned by a few centimetres during dedicated characterization discharges.

The geometrical locations of the diagnostic measurements can be mapped onto the flux coordinates according to the magnetic equilibrium solution, which in ASDEX Upgrade is typically derived by the CLISTE code [115] or by function parametrization [116, 117]. The equilibrium solvers have a radial uncertainty of several millimetres at the outer midplane separatrix position, which can lead to significant uncertainty in power and particle fluxes into the SOL, as deduced from the upstream temperature and density measurements. Therefore, power balance is typically investigated using separate bolometer measurements of radiated power in various regions which are compared to the measured ohmic and additional heating power.

Interpretation of the diagnostic measurements can be complicated, for example, because of low data quality, or because the underlying theoretical models may not be valid in the measured plasma conditions. Therefore, several diagnostics are ideally used to measure the same plasma parameters, in order to have complementary data in the analysis. In the present work, the required low-density L-mode conditions prohibited the use of standard neutral beam injection. Therefore, some of the routine diagnostic measurements of upstream profiles that rely on charge exchange reactions could not be made.

Figure 3.1: In-vessel view of ASDEX Upgrade. Figure courtesy of V. Rohde / IPP Garching.

The plasma midplane was characterized by various diagnostics, including the lithium beam [118], Thomson scattering, electron cyclotron emission [119] and reciprocating probes to measure T_e, n_e, and parallel ion flows [120, 121]. At the divertor targets, flush-mounted Langmuir probes [122] were used to measure the crucial plasma parameters at the sheath entrance. An infrared camera was used for measuring the target surface temperatures and for deriving the target power loads, which could be compared with the power loads calculated from the Langmuir probe measurements [123]. Ionisation pressure gauges [124] were used to measure sub-divertor neutral flux densities. The only information on the 2D distribution of plasma parameters was obtained by spectroscopic measurements of line radiation and by bolometer measurements of total radiation. In the divertors, the line radiation from deuterium, carbon and hydrocarbons was measured along a poloidally distributed array of lines-of-sight [125]. To compare the measurements with the modelling, synthetic diagnostics were used in the simulations.

In addition to characterizing the plasma conditions, the spectroscopic measurements were used to monitor the injection of methane into the divertor. The measured total emission from the CH molecules can be used to deduce the flux of methane molecules, according to the methane dissociation chain to CH molecules for various plasma conditions. Here, the emission from the CH A-X transition is used, with an associated wavelength range known as the CH Gerö band. Typically, only the so-called standard CH band at 429.4–430.9 nm is used, with some variations between different machines [126]. The relation between the flux and the total CH emission is given by the so-called D/XB value, which describes the rate of dissociations with respect to excitations to the measured transition levels. The method has been used, for example, to quantify chemical erosion yields [127]. However, in the present work, the CH emission was used only to identify the duration, stability, and to certain degree the shape of the methane puffs, without quantitative comparison to modelling.

3.2 Tracer injection experiments

The present understanding of material migration relies heavily on experimentally determined erosion/deposition patterns along the first wall. These are usually based on surface analyses carried out for selected first wall tiles which have been removed from the torus in between experimental campaigns. However, interpretation of such results is challenging, because the re-deposition layers result from impurity migration under various types of plasma discharges, including transient events, and magnetic geometries. Spectroscopy can be used to analyse the emission of impurities in specific discharge conditions, but only a few devices have 2D spectroscopic systems and only limited information on the migration processes can be obtained from these measurements. To study the plasma-material interactions in well-characterized discharge conditions, further in-situ diagnostics systems have been developed, including Quartz microbalance deposition monitors [128] and rotating collectors [129]. In addition, various probes can be exposed to the plasma in dedicated discharges and removed promptly afterwards for post-mortem analysis [130]. The limitation of these measurements is that they are spatially restricted and typically cannot be used on the crucial PFC components such as the divertor strike point areas.

A uniquely informative way of exploring material migration is to inject a known amount of a *tracer* material into the plasma under well-defined discharge conditions, followed by a post-mortem analysis of the relevant PFC components to measure the deposition patterns [19]. The word tracer has a two-fold meaning here. It is an element that is not naturally present in the tokamak, and can thus be distinguished from other elements in surface analyses [131]. It is also an element present in the plasma with a concentration that is sufficiently small not to affect the plasma conditions. Several tracer gases have been used in the past for such studies, including $^{13}CH_4$ [132], $^{13}C_2H_4$ [133], SiD_4 [134] and WF_6 [99]. The benefit of the first two is that methane and ethylene are natural impurity sources in any tokamak with carbon in the PFCs, but the isotopic labelling allows ^{13}C to be separated from the intrinsic ^{12}C in surface analyses. The method of injecting ^{13}C was pioneered in TEXTOR in the end of 1990s [132] and has since then been used in various tokamaks, including ASDEX Upgrade, DIII-D,

JET and JT-60U. The following gives a brief overview of the experimental outcome.

In the limiter device TEXTOR, a significant number of ^{13}C injection experiments have been carried out focusing on local erosion and deposition of impurities [99]. The tracer has been injected from both spherical limiters with graphite and tungsten substrates [133, 135] and from roof-like limiters with various substrate materials (C, W, Mo, Al) [132,136]. The limiters were placed in the bottom of the torus, with the innermost edge located 0–20 mm from the LCFS. The benefit of such *local* studies is that the deposition layers on the limiters could be analysed in detail using various surface analysis techniques, accompanied by 2D spectroscopic images of the impurity puffs.

The TEXTOR experiments revealed an increase in the net local re-deposition of ^{13}C for carbon substrates compared to metals [136], and a further increase with increasing surface roughness of the graphite substrate [135]. The most striking result, however, was that the local re-deposition was extremely small in the experiments. The *deposition efficiency*, which is the number of deposited ^{13}C atoms divided by the number injected, varied between 0.1–9%. In order to reproduce these small re-deposition fractions in modelling, full reflection of hydrocarbons had to be assumed together with enhanced re-erosion yields. These important assumptions are often included in the discussion of PWI processes [13,100]. However, presently the assumptions lack a thorough benchmarking on other devices and a detailed physical explanation.

Besides the TEXTOR experiments, all other ^{13}C studies have been carried out in divertor tokamaks. A large fraction of the experiments have focused on migration on a *global* scale, with injection from either the top of the torus or from the outer midplane, to mimic an erosion source from the main chamber wall. Typically, a LSN configuration has been used and a full poloidal distribution post-mortem analysis of ^{13}C has been performed to identify the migration pathways. Experiments in JET with a full carbon wall and Ohmic [137] and H-mode [138] plasmas have shown that ^{13}C originating from the main chamber wall is preferentially deposited in the lower inner divertor, but with significant deposition in some cases also in the outer divertor. Global migration experiments in ASDEX Upgrade using L- and H-mode plasmas with various degrees of W coating on the first wall [4, 139, 140] have resulted in

larger variations in the poloidal deposition pattern, with significant amounts of ^{13}C found even in the secondary upper divertor. Variation in the in/out deposition was observed in the lower divertor, which was suggested to be due to the change in substrate material [4]. In the carbon tokamak DIII-D, $^{13}CH_4$ was injected in a toroidally symmetric way into the crown of L-mode [141] and H-mode [142] plasmas, showing a distinct preference towards deposition in the lower inner divertor.

Prior to this thesis work, a few tracer experiments have been carried out to investigate the migration of ^{13}C originating from the divertor targets. The outer divertors in particular could be notable sources of erosion, due to the high power and particle loads to the low-field side strike points. The first such experiment was carried out in 2003 in ASDEX Upgrade, with $^{13}CH_4$ injection into the carbon divertor under H-mode conditions [143]. The majority of the ^{13}C was found locally deposited close to the injection (100% deposition efficiency according to the paper[1]). Another $^{13}CH_4$ injection from the lower outer target in a JET H-mode discharge in 2004 showed a local deposition efficiency of 17–30% [3,144], being still much higher than the typical local deposition efficiencies in TEXTOR. A third experiment was recently performed in DIII-D using an unbalanced DN configuration and $^{13}CH_4$ injection into the secondary divertor plasma, to mimic Be sputtering in the secondary divertor of ITER [145]. Again, the highest amounts of deposited ^{13}C were found in the near vicinity of the injection. The global migration pathways have thus been observed to differ between impurities eroded from the main chamber and those eroded from the outer divertor.

Understanding in detail the local migration of impurities in the outer divertor can be considered to be important for several reasons. The first ITER divertor is currently foreseen to have carbon exclusively on the strike point areas [97], but the migration of carbon onto the surrounding tungsten surfaces can lead to the formation of mixed C/W layers and thus modify the surface material properties. During the D–T phase of ITER, tritium co-deposition may occur with the beryllium which is eroded from the secondary divertor [19]. The retention of tritium outside the primary divertor can be problematic because of less effective cleaning methods projected for those regions [86], motivating further the studies of local migration and re-deposition. Finally, understand-

[1] Publication V discusses uncertainties in the deposition efficiency.

ing impurity migration in the divertor constitutes an important piece of the global migration picture, contributing to understanding the differences observed between in/out deposition in the various global migration experiments described earlier.

The majority of the work presented in this thesis focuses on understanding the local migration of carbon in the outer divertor of ASDEX Upgrade. The migration has been investigated experimentally in 2007–2009 by means of $^{13}CH_4$ injection into the divertor SOL from 1 or 2 poloidal locations along the outer target. The experiments were performed at the end of the experimental campaigns, followed by an opening of the vessel which allowed the relevant tiles to be removed for subsequent surface analyses. To provide the best possible discharge conditions for the numerical analysis (see Section 4.1) low-density L-mode discharges were used. These have the major benefit that ELMs and disruptions are absent, facilitating the interpretation. In addition, high-recycling divertor plasma regimes which are problematic for the plasma modelling (recall Section 2.1) can be avoided.

By limiting the deposition studies to a localized area which typically includes only a few selected divertor tiles, see Figure 3.2, the time-consuming post-mortem surface analyses could be carried out with a high spatial resolution, similar to the TEXTOR experiments. In the experiments discussed in this thesis, both nuclear reaction analysis, NRA [2], and secondary ion mass spectrometry, SIMS [4], have been used to derive well-resolved 2D patterns of the re-deposited ^{13}C. Apart from the earlier H-mode experiment in ASDEX Upgrade [143], such 2D distributions are unique measurements for a divertor environment, enabling a detailed benchmarking of the modelled local deposition mechanisms[2]. In addition to the ion beam measurements, a colorimetry method was used in [2] to analyse the distribution of deposited carbon on areas shadowed from the plasma due to surface roughness. The method is based on the property of amorphous hydrocarbon films to reflect light partially, showing interference colours that depend on the layer thickness [147]. This enables the deposition to be analysed with respect to small variations in the surface topography when illuminating the samples from various directions.

[2] Very recently, a similar 2D analysis has been carried out for a ^{13}C injection experiment at JET [146].

Figure 3.2: ^{13}C deposition pattern in the divertor in the 2008 experiment with a reduced injection rate. Figure courtesy of V. Rohde / IPP Garching.

Although ^{13}C injection studies are probably the most informative means of investigating the migration of impurities [19], they suffer from certain weaknesses. Firstly, in order to measure the deposition on the PFCs, the experiments must be performed just before a scheduled opening of the machine, which typically occurs only once per year or even more rarely. Thus, progress on the experimental front is slow. Secondly, the deposition layer may have been subject to several current ramp-up and ramp-down phases which complicates the interpretation[3]. Furthermore, the molecular sources are not strictly representative of natural erosion sources, even if methane constitutes a large fraction of the typical chemically eroded molecules [78]. Finally, it has been questioned whether low enough injection rates have been used in the past experiments to ensure that the injection does not perturb the local plasma conditions[4] [149–151]. This last question is addressed in Publication V, see also Section 5.

[3]The fractions of the current ramp-up and ramp-down phases when the plasma is in X-point configuration vary between different machines and discharge programs.

[4]Perturbation of plasma parameters is questioned in particular when injecting the gas through a hole. Alternatives to injection holes exist nowadays, such as the porous plug gas injection system at DIII-D [148].

4. Numerical approaches

4.1 Modelling of the boundary plasma

The most extensively used method to model the SOL and divertor plasma conditions is fluid modelling [35]. Instead of calculating the individual trajectories of the plasma particles and their mutual interaction which, on present computers, cannot be carried out for the whole boundary plasma, fluid simulations can be used to describe the variation of average fluid quantities such as temperature, density, and particle and power fluxes. The fluid equations are derived from the Fokker-Planck kinetic equation:

$$\frac{\partial f}{\partial t} + \mathbf{v} \cdot \nabla f + \frac{q}{m} (\mathbf{E} + \mathbf{v} \times \mathbf{B}) \cdot \nabla_{\mathbf{v}} f = \left.\frac{\partial f}{\partial t}\right|_{\text{coll}} + S, \tag{4.1}$$

which describes the evolution of the particle distribution function, $f(\mathbf{r}, \mathbf{v}, t)$, in the space-velocity-time coordinate frame. The equation includes the effects of multiple, small-angle Coulomb collisions, $(\partial f/\partial t)_{\text{coll}}$; here we include also a particle creation/destruction term, S, to account for the effects of various plasma–neutral and plasma-impurity reactions. By taking various velocity moments of the plasma kinetic equation, one can derive the plasma fluid equations. The most famous derivation has been given by Braginskii [36]. Following the notation in [15], we get the *continuity equation*,

$$\frac{\partial n}{\partial t} + \nabla \cdot (n\mathbf{u}) = S_n, \tag{4.2}$$

where S_n is the particle source; the *momentum conservation equation*,

$$\frac{\partial (m_{\text{i}} n \mathbf{u})}{\partial t} + \nabla \cdot (m_{\text{i}} n \mathbf{u}\mathbf{u}) = -\nabla (p + \mathbf{\Pi}_{\text{i}}) + \mathbf{j} \times \mathbf{B} + \mathbf{S}_{m_{\text{i}}\mathbf{u}}, \tag{4.3}$$

where $\mathbf{\Pi}_\mathrm{i}$ is the parallel stress tensor, $\mathbf{j}$ is the electric current density, and $S_{m_\mathrm{i}\mathbf{u}}$ is the momentum source term[1]; the *energy conservation equation for ions*,

$$\frac{\partial}{\partial t}\left(\frac{3}{2}nT_\mathrm{i}+\frac{m_\mathrm{i}n}{2}\mathbf{u}^2\right)+\nabla\cdot\left[\left(\frac{5}{2}nT_\mathrm{i}+\frac{m_\mathrm{i}n}{2}\mathbf{u}^2\right)\mathbf{u}+\mathbf{\Pi}_\mathrm{i}\cdot\mathbf{u}+\mathbf{q}_\mathrm{i}\right] = (Zen\mathbf{E}-\mathbf{R})\cdot\mathbf{u}-Q_\mathrm{ei}+S_{E_\mathrm{i}}, \quad (4.4)$$

where $\mathbf{q}_\mathrm{i}$ is the ion heat flux, $\mathbf{R}$ accounts for resistive heating, Q_ei is the energy exchange term between electrons and ions, and S_{E_i} is the ion energy source term; and the *energy conservation equation for electrons*,

$$\frac{\partial}{\partial t}\left(\frac{3}{2}nT_\mathrm{e}\right)+\nabla\cdot\left(\frac{5}{2}nT_\mathrm{e}\mathbf{u}+\mathbf{q}_e\right)=-en\mathbf{E}\mathbf{u}_\mathrm{e}+\mathbf{R}\cdot\mathbf{u}+Q_\mathrm{ei}+S_{E_\mathrm{e}}, \quad (4.5)$$

where $\mathbf{q}_e$ is the electron heat flux, $\mathbf{u}_\mathrm{e}$ is the electron fluid velocity and S_{E_e} is the electron energy source term.

Typically, the variation of plasma parameters in the toroidal direction is neglected as being small, and the fluid quantities are solved in the parallel and radial directions on a 2D poloidal plane. As the radial transport is known to be anomalous, recall Section 2.1, the classical expressions for the radial particle and heat fluxes are replaced in 2D fluid modelling by anomalous fluxes. One important aim of code-experiment validation is to find the set of transport assumptions which best agrees with the measured plasma conditions, typically requiring that extensive parameter variations are performed in the simulations. Such work is necessary to derive scaling laws for predictive modelling of future devices, for which no experimental information is available. It should be noted, however, that the transport in the fluid codes is assumed to be laminar, and the neglect of temporal variation due to turbulent transport is a potentially significant, yet unresolved, weakness of the approach [35].

An alternative approach to the 2D modelling described above is to use an onion-skin model, OSM [23,152]. OSM solves 1D fluid equations on each flux surface in the SOL according to imposed values of temperature, density and flow velocity at the two target plates. The cross-field transport between the

[1]Note that this is the total momentum conservation equation. Electron inertia is typically neglected when deriving the electron momentum conservation equation.

flux surfaces is treated as sources and sinks in the equations. The transport levels do not need to be described *a priori*, which significantly reduces the computational efforts required to find a suitable model for a set of experimental data. The trade-off in such an approach is that the radial profiles of the target plasma parameters must be known in advance, which limits OSM to an interpretive model. The profiles of T_e and $\Gamma_{\parallel}$ are typically measured in experiments, but often with significant uncertainties. Furthermore, additional assumptions are needed to describe the variation of T_i for example.

The work presented in this thesis focuses on validating a set of codes that can be used as predictive tools. The benefit of using such codes in interpretive work is that they typically include the best available physics models, since a large part of present-day code development efforts are directed to support the design of future fusion devices. Therefore, a 2D multifluid code package, solving the full plasma+neutral+impurity mixture, is used to model the boundary plasma in ASDEX Upgrade. There exist several codes, from which B2/B2.5 [153], EDGE2D [154] and UEDGE [155] have been most extensively compared to experimental observations. These codes can be coupled to kinetic neutral simulations, using codes like Eirene [156], DEGAS [157] or NIMBUS [158]. The various coupled versions of B2/B2.5 and Eirene are commonly known as the SOLPS code package [15,159]. It is most extensively developed with a predictive aim and is, thus, used to model the boundary plasma in ITER [160].

The present work uses the SOLPS5.0 code package version. It is based on the B2.5 multifluid code, which calculates the parallel transport of particles by solving a modified and extended set of the Braginskii equations for electrons, ions and neutrals [15, 161]. Unlike the older B2 code used in the SOLPS4.* series, B2.5 includes calculation of drifts ($\mathbf{E} \times \mathbf{B}$, diamagnetic) and currents [162], which can be important for correct modelling of the in-out asymmetries (recall Section 2.1). The Eirene code, which can be coupled iteratively to the plasma fluid code, solves the 3D Boltzmann transport equations for the neutral distribution function [156]. Two versions of Eirene are available in SOLPS5.0: the 'old' version from 1996 and the 'new' version from 1999 [159], which has the benefit of a more advanced treatment of atomic and molecular physics and reflection models at the wall elements. In addition to the B2.5-Eirene part, the code package includes a grid generat-

ing code CARRE [163] and a graphical display program for setting up new magnetic configurations, called DG. The plasma parameters are solved on a quasi-orthogonal 2D mesh, an example of which is shown in Figure 4.1 for ASDEX Upgrade.

Various models for plasma-wall interaction can be specified in the simulations by using boundary conditions. The solutions extend until the entrance of the magnetic presheath, where modified Bohm-Chodura boundary conditions are used for the ion flow velocity and heat fluxes [26]. The sputtering yields are based on tabulated data, discussed further in the next section, and the probabilities for re-deposition and recycling are specified by the user. The transport of various impurities, such as C and He, is calculated assuming that all ions have a common fluid temperature, T_i. In the simplified neutral fluid model contained within B2.5, this common temperature is assumed also for the neutral species.

It should be noted that, in the course of the present work, the various versions of the code package have been developed and the physics models have improved in some cases. These features were not, however, included in the work presented in this thesis. The SOLPS5.0 version has been upgraded to allow feasible modelling of high-Z impurities such as W by using bundled charge states [164] and to better describe material mixing at the wall elements [165, 166]. A new implementation of drift models has been incorporated, leading to a new version, SOLPS5.2 [167], which is observed to better reproduce certain H-mode plasma conditions compared to SOLPS5.0. The Eirene code has been developed to include more ITER-relevant physics such as neutral-neutral collisions and radiation opacity [168], and these enhancements have been merged into SOLPS4.0 to produce the SOLPS4.2-3 versions which are used in ITER modelling. Finally, dynamic grid adaptation allowing for simulation of localized phenomena with better spatial resolution has been under development to produce the SOLPS6.0 version [169, 170].

In Section 2.1, the effects of low collisionality on the divertor plasma conditions were discussed. The expressions used in fluid modelling for parallel heat conduction, recall Equation (2.3), and viscosity are known to break down in the long mean-free-path limit, $\lambda_\mathrm{coll} \to \infty$ [23]. This thesis focuses in particular on kinetic effects on the parallel heat fluxes [171]. A common procedure

in fluid codes is to limit $q_{\parallel}$ given by Equation (2.3) (+ convective part) to a certain fraction of the free-streaming heat flux. The specified *flux limiters* are typically spatially constant and defined by the code user. In the fully collisional (fluid) and collisionless (convective) regimes, they should not influence the solutions. However, in the medium-collisionality regimes the codes have been shown to yield steeper parallel temperature gradients when a flux limiter is introduced, reducing the target temperatures [15]. This rather crude accounting of collisionless effects is a potential weakness of the fluid codes.

Whilst comparison of the fluid simulations with fully self-consistent kinetic calculations is not yet feasible, test particle simulations can be used to a certain extent to investigate kinetic effects in the SOL. The present work includes a comparison of a SOLPS5.0 solution for a medium-collisionality plasma with kinetic orbit-following simulations using the ASCOT code [17, 172]. ASCOT is a Monte Carlo code which simulates test particles in a prescribed background plasma[2], obtained, in the present work, by interpolating the plasma parameters from the SOLPS5.0 plasma solution onto a Cartesian 2D grid in ASCOT. The code calculates the 3D guiding-centre orbits of charged particles, including the effects of cross-field drifts [173]. The influence of Coulomb collisions is modelled by Monte Carlo operators derived from the Fokker-Planck equation. They change the energy and velocity direction of the test particles, assuming that the background plasma is Maxwellian [174, 175]. In the present work, the particles are traced until they first impinge on the wall boundaries, and the evolution of their energies is recorded during their propagation. Such simulations can thus be used to follow the energy distribution of a given particle ensemble on the way to the divertor targets.

4.2 Impurity migration simulations

The fluid codes discussed in the previous section can be used to model the transport of impurities in the edge plasma, making the fluid approximation also for the impurity species [107]. To follow the detailed impurity trajectories, particle-following codes such as DIVIMP [152] have been applied in the

[2]The features of ASCOT are described according to the status in code development during Publication I.

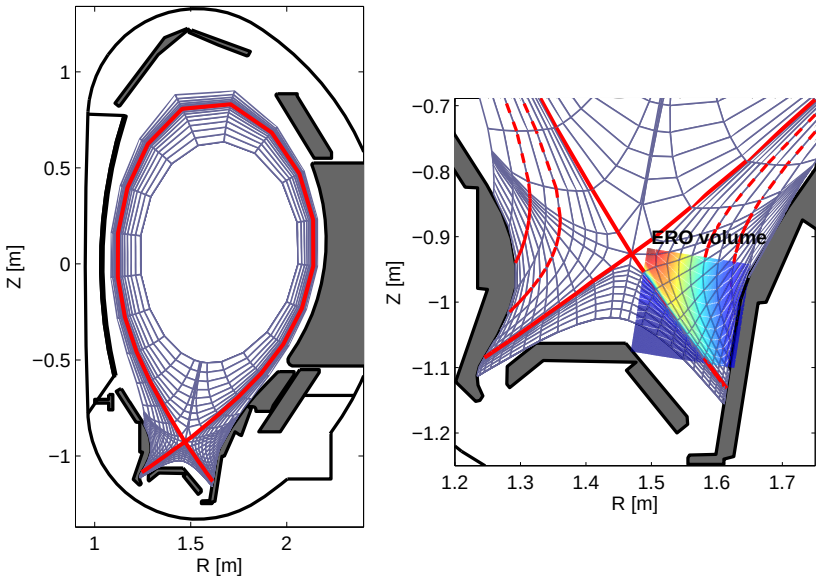

Figure 4.1: SOLPS5.0 (left) and ERO (right) simulation regions.

past. However, to describe the formation of re-deposited layers and migration through multiple erosion steps, specialized codes which calculate the detailed PWI processes are required. In this thesis work, interpretation of the local ^{13}C deposition patterns necessitated following the 3D transport of impurities and calculating the erosion and deposition on the divertor surface. This was performed using the ERO code [176] on a SOLPS background plasma. The original version of ERO [16, 130] has undergone several changes over the years, and it is still being continuously upgraded to keep it up to date with the recent advances in understanding of PWI processes. The following describes the main features of the ERO code version during the present work.

The traced particles in ERO include the particles eroded from the substrate and those from a possible external source, such as an injection. Each source is treated using test particles which represent a large number of real particles, and the Monte Carlo method is used to describe the interaction of the impurities with the plasma. The plasma background is prescribed and a Maxwellian energy distribution in the plasma is assumed. The ionization of the impurities is calculated primarily using rate coefficients from the Atomic Data and

Analysis Structure, ADAS [177,178]. The various dissociation and ionization reactions of hydrocarbons are taken into account using rate coefficients from Janev and Reiter [101].

The neutrals are typically assumed to follow straight trajectories without interacting with the plasma, until they become ionized. In addition, one can include collisions with neutral particles in the simulations. Ion trajectories are calculated from the Lorentz force by using the Boris integration method [33]. They thus include the Larmor gyration and the cross-field drifts due to electric and magnetic fields. The ions experience Coulomb collisions with the background plasma, giving rise to a friction force determined by the Spitzer relaxation time constants. Thermal forces arising from temperature gradients are calculated separately [36, 179] and a cross-field diffusion coefficient can be specified by the user.

Reflection of the impurity ions and atoms returning to the material surface is calculated in most cases using data from the TRIM code [180,181]. TRIM is based on the binary collision approximation, BCA, which treats the ion-solid interaction as a sequence of independent binary collisions between the projectile and the surface atoms [182]. The BCA codes are not, however, reliable for modelling the low impact energy range and reflection of molecules, in which cases data from molecular dynamics simulations, MD, are needed [183,184]. Results from MD calculations can be used to determine an effective sticking probability for the hydrocarbons that is specified in an input file. More general implementation of MD data in ERO was only partially done during the present work [185], which leaves uncertainties in the modelling of hydrocarbons, discussed further below.

There are two options for calculating the evolution of the material surface under plasma and impurity impact in ERO [178,186]. The conventional way is to use a homogeneous mixing model, HMM, which assumes that the redeposited impurities are homogeneously mixed with the substrate material in an interaction layer of user-specified thickness, d_{int}. Only the material contained within this interaction layer can be eroded; the required d_{int} therefore increases with the incident flux and with the time step chosen for the surface evolution. Another option, not used in this thesis work, is to carry out depth-resolved simulation of the material mixing by coupling ERO to the

SDTrimSP code [187]. SDTrimSP is based on the BCA [188], and the coupled version has been modified to include a model for chemical erosion [186]. Regardless of which of the two methods is chosen, the PWI processes are calculated within laterally distributed orthogonal cells, whose dimensions are specified by the user.

The physical sputtering yield caused by the background plasma is calculated in ERO according to the impact-energy dependent Bohdansky formula [72, 74][3], assuming a normal incidence of the impinging particles and taking into account acceleration by the sheath potential difference [190]. The traced impurities can further sputter the material surface with yields which depend on their actual incidence angles according to Yamamura [73]. For the chemical erosion yield, the user can specify to use either the surface-temperature dependent Roth formula [83] or a fixed value.

ERO is typically applied to model limited surface areas, since the computational expense of whole device simulations would be unbearable with the detailed approach used in ERO. Several versions of ERO exist, which have been specifically adapted to different machine geometries and regions of interest. For tokamaks, a version tailored for modelling limiter surfaces [99] and a separate version for the divertor surfaces [178] exist. Linear devices have also been modelled using a dedicated version [191]. The major difference between the two tokamak versions is that the variation of plasma parameters in front of a limiter can be calculated analytically by ERO, whereas the plasma background in the divertor must be specified by the user, using the methods described in Section 4.1.

The limiter version of ERO has been most extensively benchmarked against experimental data and it has been used in the interpretation of the local tracer injection experiments in TEXTOR [99], recall Section 3.2. In particular, the necessary assumptions in modelling carbon impurities have been explored in various test limiter environments. As discussed in Section 2.2, the benchmarking has shown that a low or even negligible effective sticking of hydrocarbons must be assumed, together with an enhanced re-erosion yield of the re-deposited carbon, in order to match the measured low deposition

[3] Very recently, sputtering yields based on new empirical formulae by Eckstein [189] have been included in ERO.

efficiencies [98]. This conclusion is supported by EDDY simulations of the same experiments [192]. In [186], ERO-SDTrimSP simulations were shown to reproduce the difference in measured ^{13}C deposition on carbon and tungsten surfaces better than ERO-HMM.

ERO has been used to model the erosion and deposition in a divertor geometry using various background plasma models. In [193], a 2D version of ERO was applied to model erosion and deposition in the JET divertor using plasma backgrounds from OSM calculations. The first attempt to model $^{13}CH_4$ injection in ASDEX Upgrade was made with a background plasma obtained with SOLPS5.0 [2]. A similar benchmarking was carried out in [3] for JET using a plasma solution from EDGE2D-NIMBUS [107]. Very recently, an OSM model was again applied for modelling carbon deposition in a detached divertor plasma of JET [194]. Predictive ITER simulations [178, 195, 196] were performed with a plasma solution obtained from SOLPS4.2 simulations [197].

In the present work, solutions from SOLPS5.0 simulations are used to describe the plasma background for ERO calculations. The plasma solutions have been carefully adjusted to match the measured conditions in the ERO simulation volume and the description of the background plasma in ERO has been improved in the course of this work, as discussed in Section 5. These integrated SOLPS5.0-ERO simulations therefore attempt to represent the most realistic description of local impurity transport in a vertical divertor geometry up to date.

5. Results

5.1 Validation of the plasma fluid solutions

A significant part of the work presented in this thesis has focused on validating the SOLPS5.0 simulations of plasma discharges in ASDEX Upgrade. The first part of the validation was carried out in comparison with test particle simulations using the ASCOT code and was reported in Publication I. The SOLPS5.0 plasma solutions in that comparison were derived outside this thesis work [1]. The second and longer part of the validation work consisted of benchmarking SOLPS5.0 simulations against experimental data from ASDEX Upgrade, and the results were reported stepwise in Publications III-V. For this purpose, several dedicated experiments were performed in ASDEX Upgrade.

Comparison with kinetic simulations was motivated by the observations made in [1] when comparing SOLPS5.0 simulations with experimental data from a medium-collisionality ASDEX Upgrade H-mode discharge. The simulations were found to yield a cooler and denser outer divertor plasma compared to what was measured with target Langmuir probes during an inter-ELM phase. It was suggested that the collisionality of heat-carrying electrons might not be sufficient to ensure a Maxwellian energy distribution at each location in the divertor plasma. Instead, the energy distributions could have an increased weight in the supra-thermal tail, increasing the average energy at the targets compared with that expected from a normal Maxwellian. This could affect the sheath potential, having thus wider consequences on the divertor plasma conditions through changes in the $\mathbf{E} \times \mathbf{B}$ drifts.

ASCOT simulations were carried out in Publication I to investigate the evolution of the energy distribution of an electron ensemble launched at the outer midplane. The electrons were launched at three different radial locations, from just outside the separatrix to a centimetre away from it[1], and with three different initially Maxwellian energy distributions, corresponding to temperature $T_{\mathrm{M-B}} = mT_{\mathrm{u}}$, where m=1,2,3. The electrons were subject to Coulomb collisions and parallel electric field in a plasma background defined by the SOLPS5.0 solutions of an inter-ELM period, and followed until they reached the divertor targets. The parallel density and temperature gradients were largest on the innermost flux surface, resulting in temperatures below 5 eV at both targets. The field-line averaged collisionality was approximately the same on all flux surfaces.

The existence of a significant hot tail in the electron energy distribution at the target was found to depend on the magnitude of parallel temperature gradients in the divertor plasma. On the innermost flux surface with a strong $\nabla_{\parallel} T_{\mathrm{e}}$ below the X-point, the energy distribution recorded at the target was non-Maxwellian, having an increased weight of the suprathermal tail. The suprathermal electrons carried 70% of the total energy recorded at the outer target, and their presence was found to significantly increase the target heat loads from that expected from a thermalized ensemble. The hot electron losses were found to originate from various locations upstream; prompt kinetic losses from the outer midplane could not alone explain the large suprathermal component at the target, but collisionless electrons originating from the X-point region had to be considered in addition. On the outermost flux surfaces, the collisionality of the plasma upstream of the X-point was found to be sufficient to bring even initially suprathermal electron ensembles close to the field-line averaged T_{e}. Because of the smaller $\nabla_{\parallel} T_{\mathrm{e}}$ in the divertor, the effect of suprathermal electrons on target heat loads was small on these flux surfaces.

The results show that the energy composition of electron losses is very sensitive to the distribution of n_{e} and T_{e} along the field lines. The gradients in these parameters are largely determined by the recycling and ionization of neutrals in the divertor. In this work deviations from the fluid model were observed in particular when the divertor plasma was in high-recycling regime.

[1]These locations correspond to a poloidal flux coordinate, ρ, in the range 1.001–1.02.

Kinetic behaviour of electrons can, therefore, be significant for parallel heat fluxes in a medium-collisionality SOL, but it cannot be assessed simply based on the average collisionality of the SOL. However, as the ASCOT simulations were made using a prescribed plasma background, no attempt could be made to describe the target electron energy distribution self-consistently. Therefore, quantitative implications of these kinetic effects could not be assessed within this work.

Because of the difficulties experienced when modelling the high-recycling as well as detached regimes [5] (recall also Section 4.1), the code-experiment validation in the following publications (II–V) focused on low-density discharges. The experiments were prepared with the aim of obtaining low-recycling divertor plasmas. As described in Section 2.1, parallel temperature gradients are small in that regime, which tends to make kinetic effects less important for the divertor solutions.

The plasma solutions in publications II–V were developed for the purpose of following impurity migration in the outer divertor, to be discussed in Section 5.2. A realistic description of the migration processes necessitated a high level of agreement between the measured outer divertor plasma conditions and those modelled with SOLPS5.0. Therefore, the assumptions on e.g. cross-field transport and plasma-wall interaction were adjusted in a way that yielded the best agreement between modelled and measured plasma conditions on the LFS of the torus. This approach can be considered acceptable as long as possible deficiencies in the inner divertor model can be estimated to be local. Furthermore, the full uncertainty range of the upstream measurements, including the separatrix position and radiated power, was explored to find a solution that best agrees with the outer target measurements. A consistency check between the various diagnostic measurements was performed to assess the validity of the solution.

The first experiments to be modelled were conducted in low-density L-mode, with a low-recycling outer divertor plasma. SOLPS5.0 simulations were carried out first with the new Eirene-99 version and with impurities, but no cross-field drifts activated. These simulations revealed a peaking and overestimation of the density at the outer target, which could be remedied only by switching on cross-field drifts in the code. In Publication III, the cross-field

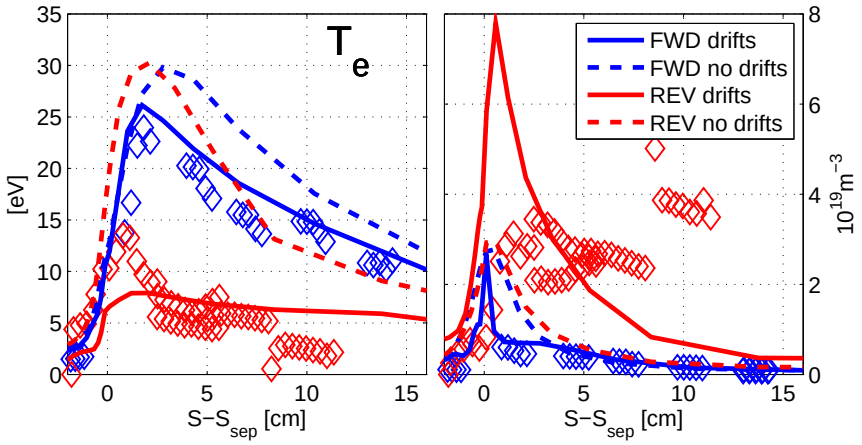

Figure 5.1: Effect of cross-field drifts on the plasma solutions calculated with SOLPS5.0, for forward (FWD) and reversed (REV) field L-mode configurations. The calculated profiles of temperature (left) and density (right) are plotted along the poloidal S-coordinate that follows the target surface. S_{sep} refers to the value of S at the separatrix location. The Langmuir probe measurements are shown by the blue and red diamonds for forward and reversed field, respectively.

drifts were shown to flatten the target density profile, so that a good level of agreement with the measured density was obtained.

To further investigate the effect of cross-field drifts, a similar low-density L-mode experiment was carried out with reversed toroidal magnetic field and plasma current. As a consequence, the outer divertor plasma was observed to become much denser compared to the forward field configuration, increasing the recycling fluxes at the outer target. Furthermore, the density was observed not to decay outside the strike point, but a steady profile along the outer target was measured. The SOLPS5.0 simulations with cross-field drifts activated were able to reproduce this change in the outer target density with the field reversal, as shown in Publication IV and in Figure 5.1. However, the density profile along the outer target was found to be more peaked than in the experiments.

Finding a plasma solution which agrees not only with the measured density but also with the measured electron temperature at the outer target was at

low density found to be challenging. A high radial electron heat diffusivity and a lower input power than indicated by the measurements had to be assumed to bring down both upstream and target T_e. These assumptions are described in detail in Publication V, where it is shown that the decrease in input power is consistent with the measurement uncertainties and suggested also by other experimental data. Finally, the plasma solutions were shown to agree with all experimental data in the outer divertor, indicating a good consistency between the various diagnostic measurements.

In reversed field, neither n_e nor T_e modelled with SOLPS5.0 could be accurately matched with the measured profiles along the outer target, even when all the uncertainties in the experimental data were considered and assumptions in radial transport coefficients and plasma-wall interaction processes were varied. A good agreement with the measured total outer target power and particle fluxes was, however, obtained.

Finally, a thorough validation of the forward and reversed field SOLPS5.0 solutions was presented in Publication V, including the various measurements made in the main SOL and in both divertor legs. In forward field, the inner target was in a high-recycling regime; the simulations gave higher particle fluxes compared with the measurements, but a satisfactory agreement was obtained with the measured low T_e. The measured conditions on the low-field side were well reproduced, except for the parallel ion flows which were underestimated in the simulations by a factor of 2–3. In reversed field, the inner target was observed to be in a medium-recycling regime, with high-recycling conditions measured at the inner strike point. The simulations also yielded a medium-recycling inner divertor plasma, but the high recycling zone and the measured large D_ϵ emission were not reproduced. A satisfactory agreement between the modelled and measured in-out asymmetries was obtained with respect to power and particle fluxes. Furthermore, a good quantitative match to the measured parallel ion flows in the main SOL in reversed field was obtained in the modelling.

Overall, the validation work identified an important role of cross-field drifts on the divertor plasma conditions when modelling low-density discharges in ASDEX Upgrade, as illustrated in Figure 5.1. Detailed validation of SOLPS5.0 solutions against such low-density discharges in both forward and reversed

field was presented for the first time. It was shown that in forward field, a good agreement with LFS measurements could be found within the experimental uncertainty range, for the case of a low-recycling outer divertor plasma. In reversed field with a medium-recycling outer divertor, a similarly good agreement could not be found. Nevertheless, the experimental data was reproduced within a factor of 2 in reversed field.

5.2 Local migration of carbon impurities

The migration of carbon in the outer divertor plasma was investigated in a series of L-mode $^{13}CH_4$ injection experiments in ASDEX Upgrade, described in Section 3.2. The first such experiment took place in 2007, and the measurements of local carbon deposition in that experiment were reported in [2]. A second experiment was carried out in 2008 with reversed toroidal magnetic field and plasma current. The outcome of the experiment was reported in Publication II, but the plasma conditions obtained were not sufficiently steady for detailed modelling. In the course of this thesis work, two more experiments were successfully performed, including a forward field experiment in 2008 and a reversed field experiment in 2009. The experiments were modelled in Publications II–V using the integrated SOLPS5.0–ERO simulations described in Section 4.2.

The modelling focused on understanding the role of plasma conditions in the local outer divertor migration of carbon. In Publication II, a first analysis of the relevant transport mechanisms was carried out. It was observed that neutral dissociation products can increase deposition on wall elements which are not magnetically connected with the main ionization locations. The fraction of this *upstream* deposition was found to be sensitive to the strength of the plasma friction force and, therefore, to plasma collisionality. Experimentally, the deposition tails were found to deviate along the target from the magnetic field direction, in a direction that was observed to reverse with the field reversal. The simulations could not, however, reproduce this apparent drift effect, when only the electric fields in the Debye sheath and magnetic presheath were taken into account.

In Publication III, the electric field models were extended to include the potential variations outside the magnetic presheath, as calculated in the SOLPS5.0 simulations. It was found that both radial and poloidal electric field components exist in the divertor plasma, producing a drift along the target surface and in the direction normal to it. The effect of such drifts is illustrated in Figure 5.2 for the various directions of B_ϕ and I_p. In forward field, the modelling showed an increase in local carbon deposition because of the $\mathbf{E} \times \mathbf{B}$ drift, as more ions returned to the target surface. In addition, the $\mathbf{E} \times \mathbf{B}$ drift was found to be a key mechanism enhancing upstream deposition, unlike the thermal forces that were suggested in Publication II. This observation underlined the importance of correct modelling of the variations in plasma parameters close to the target, which affect the magnitude and direction of the electric field. As pointed out in Section 5.1, good agreement with experimental profiles could only be obtained when including drift effects in the plasma simulations.

In order to further benchmark the drift models, a new experiment in reversed field was presented and modelled in Publication IV. The modelled deposition patterns were found to deviate now in the opposite direction from the magnetic field lines compared to forward field, which was in satisfactory agreement with experimental observation. However, unlike in the first reversed field experiment discussed in Publication II, the new experimental results showed no deviation in the far end of the deposition tails. This small difference was not captured in the modelling. In addition to the reversed hydrocarbon drifts illustrated in Figure 5.2, the deposition patterns were found to reflect the changes in divertor plasma conditions driven by the field reversal. More precisely, the increase in the divertor collisionality with the field reversal was found to reduce the deposition upstream from the injection, which was seen in both simulations and experiment.

In Publication IV, the injection rates used in the experiments were recalibrated, allowing a first quantitative comparison between modelled and measured deposition efficiencies. In forward field, deposition efficiencies in the range 24–32% were obtained. The experiments showed a factor of 2 decrease in deposition efficiency with the field reversal. The modelling agreed qualitatively with the reduction in deposition efficiency by the field reversal. However, in both field directions a higher deposition efficiency at the lowermost

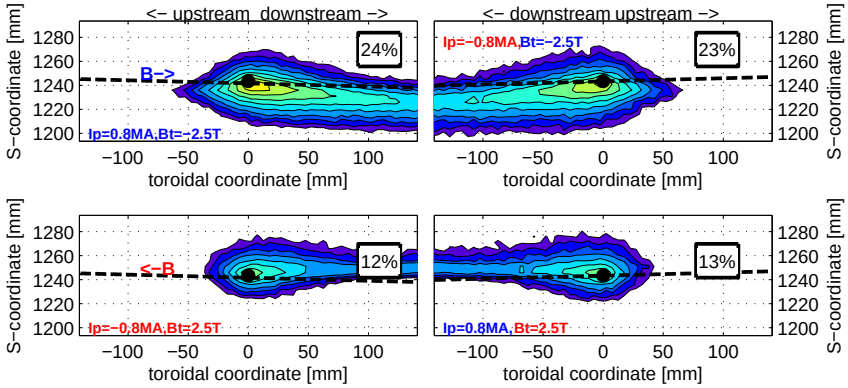

Figure 5.2: Illustration of drift effects on the deposition of carbon. The 2D deposition patterns are modelled with ERO by specifying different B_ϕ and I_p directions but using the same (forward field) plasma solution from SOLPS5.0 (and thus the same $\mathbf{E}$ in each case). Hydrocarbons are assumed to be fully reflected, to emphasize the effect of the plasma transport on the pattern. The numbers give the local deposition efficiency in each case. The upper and lower left figures correspond to the forward and reversed field configurations in ASDEX Upgrade, respectively.

injection location was obtained in the modelling compared to experiments. In forward field, this discrepancy was only in the deposition in the near vicinity of the exit hole, whereas in reversed field, the modelling overestimated the deposition at all locations. Several possible reasons for the discrepancies were suggested, including flaking of the deposit during tile removal, uncertainties in reflection models for hydrocarbons, effects of neighbouring tile edge, and local perturbation of the plasma.

In Publication V, the transport of various hydrocarbon molecules was investigated. Analysis of the modelled particle trajectories showed that the majority of the hydrocarbons returning to the surface have not penetrated deeper into the plasma than the magnetic presheath region, from where they are brought back to the surface and deposit close to the injection location. Carbon atoms deposit forming a circular pattern around the exit hole, whereas particles travelling outside the MPS are fully dissociated to ionized carbon, travel furthest away and re-deposit defining the characteristic pattern observed at the target. The pattern was thus found to reflect the transport properties

of ions in the plasma region modelled with SOLPS5.0, whereas a significant contribution to the deposition efficiency could come from the hydrocarbons.

Various hydrocarbon reflection models were tested in ERO simulations, including fully reflected and fully sticking hydrocarbons. The hydrocarbons were also assigned molecule- and energy-dependent reflection coefficients, which necessitated a simultaneous increase in their prompt re-erosion yields. Using a single reflection model, agreement with measured deposition efficiencies was not obtained for all the valves and experiments simultaneously. The effects of the magnetic presheath model and tile geometry used in the simulations were pointed out as likely to influence the solution for hydrocarbon deposition.

Publication V included the new results from the second forward field experiment, in which similar plasma conditions but a lower injection rate of $^{13}CH_4$ was used compared with the first experiment. The injection rate was not found to influence the transport directions, suggesting that any large perturbation of the local electric field had not occurred with the higher injection rate. Spectroscopic measurements indicated that the possible perturbation was limited close to the exit hole location. The deposition efficiency was, however, found to reduce by a factor of 2 with the reduction of injection rate. The reduction in deposition occurred at all locations; the extension of the tails decreased in particular. The simulations showed no change in the deposition efficiency, which could be because of inadequate modelling of C/W mixing or current ramp up / ramp down phases in the discharges.

From the results one may conclude that the effects of plasma friction and $\mathbf{E} \times \mathbf{B}$ drifts on carbon migration are significant. This emphasizes the importance of including drift effects when modelling impurity migration in the divertor. Such work has been urged [198] but was not included in kinetic simulations of divertor impurity migration before the present work. The transport due to an $\mathbf{E} \times \mathbf{B}$ drift can influence the direction and rate of impurity "walking" [107] that is due to the subsequent re-erosion and re-deposition steps in the divertor, and can therefore affect the net leakage of impurities from the divertor and mixing of materials inside the divertor. To validate the assumptions on hydrocarbon re-deposition efficiency, a careful analysis of the magnetic presheath using, for example, PIC simulations is suggested.

6. Conclusions

Detailed numerical analysis of dedicated plasma characterization discharges and tracer injection experiments in ASDEX Upgrade showed that the plasma conditions and impurity migration in the outer divertor are significantly influenced by cross-field drifts. Interpretive SOLPS5.0–ERO simulations demonstrated that the local migration pathways are largely determined by the $\mathbf{E}\times\mathbf{B}$ drift in the divertor and by the friction force caused by the plasma flow. These are both affected by the reversal of the magnetic field which, due to the reversal of drifts, changes the plasma conditions in the divertor. Accurate modelling of the spatial distribution of plasma parameters in the divertor was thus concluded necessary to reproduce the measured deposition patterns in simulations.

To validate the SOLPS5.0 plasma fluid solutions, comparison with an extensive set of experimental data from low-density L-mode discharges in forward and reversed field was made. It was observed that in forward field, with a low-recycling outer divertor plasma, a good agreement with all measurements on the LFS could be obtained, provided that cross-field drifts were activated in the simulations. Nevertheless, discrepancies in the radial profiles were found when modelling a similar reversed field discharge, with medium recycling in both inner and outer divertor. An exception was found when comparing the measured and modelled parallel ion fluxes on the outer midplane, which were quantitatively matched only in reversed field.

Simulations with the Monte Carlo code ASCOT were carried out in addition for a medium-density H-mode discharge, revealing that in medium collisionality, a significant fraction of electrons can reach the divertor target with suprathermal energy. These hot electrons could substantially increase the target heat loads with respect to those which would be expected from a ther-

mal, Maxwellian population. The energy composition of electron losses was found to be very sensitive to the distribution of the background electron density and temperature along the field lines. Therefore, the deviations from a fluid model can not be assessed based on simple estimates that consider only field-line averaged collisionality or prompt kinetic losses from the outer midplane. Detailed kinetic modelling is, thus, required. Deviations from the fluid model were found to be significant in the case of a large temperature gradient along the field lines just outside the separatrix, associated with a high-recycling divertor plasma.

In conclusion, reliable fluid plasma solutions for the divertor could be identified only when the recycling of neutrals in the divertor was low enough to prevent significant temperature drop on the way from upstream to the target. This was observed independent of the level of agreement between measured and modelled main SOL ion flows. The agreement with the measurements in the outer divertor was significantly improved when cross-field drifts were activated in the simulations.

Based on the above discussion, the SOLPS5.0–ERO simulations could be best validated in comparison to the forward field experiments in low density. A detailed inspection of the modelled trajectories of the injected methane molecules revealed that in low-recycling divertor conditions, a large fraction of hydrocarbons dissociates already within a few ion Larmor radii of the surface, where their transport is dominated by the strong magnetic presheath electric field. The majority of hydrocarbon deposition occurs therefore in the near vicinity of the injection location. Since a significant fraction of the released molecules arrive at the surface as hydrocarbons, the assumptions made on their reflection and re-erosion influences the modelled net erosion/deposition rates. Detailed modelling of the magnetic presheath, including the effects of tile gaps and protruding edges, was suggested for simulations of hydrocarbon re-deposition.

Further away from the source, it is either carbon atoms or carbon ions which define the local deposition pattern. The dissociation or ionization to carbon ions occurs outside the magnetic presheath, where the transport is controlled mostly by the divertor plasma conditions. The migration pathways were thus found to be determined by carbon ions and can be considered to apply to

impurities in general. The field reversal was observed to change the migration of impurities in both toroidal and poloidal directions having, thus, wider implications for the leakage of impurities out of the divertor and for material mixing along a target which is composed of several materials. A change in transport towards the surface could be observed as well, leading to smaller re-deposition efficiencies in reversed compared to forward field.

The observed changes in carbon migration could be attributed to the changes in the $\mathbf{E} \times \mathbf{B}$ drift of carbon ions and plasma friction. This underlines the importance of realistic modelling of the distribution of plasma density and temperature in the divertor plasma. Overall, the good agreement between the SOLPS5.0–ERO simulations and measured local impurity migration in low-density discharges can be considered as a promising result with respect to integrated modelling of material migration.

References

[1] Chankin A V *et al*, 2006 *Plasma Physics and Controlled Fusion* **48** 839–868

[2] Pugno R *et al*, 2009 *Journal of Nuclear Materials* **390-391** 68–71

[3] Airila M I *et al*, 2009 *Physica Scripta* **2009(T138)** 014 021

[4] Hakola A *et al*, 2010 *Plasma Physics and Controlled Fusion* **52(6)** 065 006

[5] Wischmeier M *et al*, 2011 *Journal of Nuclear Materials* **In Press, Corrected Proof**

[6] Makkonen T *et al*, 2011 *Journal of Nuclear Materials* **In Press, Corrected Proof**

[7] Shimada M *et al*, 2007 *Nuclear Fusion* **47(6)** S1

[8] Pitts R, Buttery R and Pinches S, 2006 *Physics World* **19(20)**

[9] Wesson J, 2004 *Tokamaks*, chap. 2.5. Clarendon Press - Oxford, 3rd edn., 42

[10] Wagner F *et al*, 1982 *Physical Review Letters* **49(19)** 1408–1412

[11] Zohm H, 1996 *Plasma Physics and Controlled Fusion* **38(2)** 105

[12] 2011. *EFDA-JET web page*. www.jet.efda.org

[13] Roth J *et al*, 2009 *Journal of Nuclear Materials* **390-391** 1–9

[14] Chankin A and Coster D, 2009 *Journal of Nuclear Materials* **390-391** 319–324

[15] Schneider R *et al*, 2006 *Contributions to Plasma Physics* **46(1-2)** 3–191

[16] Kirschner A *et al*, 2000 *Nuclear Fusion* **40** 989

[17] Heikkinen J A *et al*, 2001 *Journal of Computational Physics* **173** 527–48

[18] Herrmann A, 2003 *Fusion Science and Technology Special Issue* **44(3)**

[19] Stangeby P, 2011 *Journal of Nuclear Materials* **In Press, Corrected Proof**

[20] Wesson J, 2004 *Tokamaks*, chap. 3.7. Clarendon Press - Oxford, 3rd edn., 119

[21] Chodura R, 1982 *Physics of Fluids* **25(9)** 1628–1633

[22] Chodura R, 1986 *Physics of Plasma-Wall Interactions in Controlled Fusion*. Plenum Press, New York, 99

[23] Stangeby P, 2000 *The Plasma Boundary of Magnetic Fusion Devices*. IOP Publishing Ltd

[24] Riemann K U, 1992 *Contributions to Plasma Physics* **32(3-4)** 231–236

[25] Bohm D, 1949 *The Characteristics of electrical discharges in magnetic fields*. McGraw-Hill, New York, 1st edn.

[26] Stangeby P C and Chankin A V, 1995 *Physics of Plasmas* **2(3)** 707–715

[27] Tskhakaya D and Kuhn S, 2002 *Contributions to Plasma Physics* **42(2-4)** 302–308

[28] Tskhakaya D and Kuhn S, 2004 *Contributions to Plasma Physics* **44(5-6)** 564–570

[29] Cohen R and Ryutov D, 2000 *Contributions to Plasma Physics* **40(3-4)** 456–470

[30] Tskhakaya D *et al*, 2009 *Journal of Nuclear Materials* **390-391** 335–338

[31] Tskhakaya D and Kuhn S, 2003 *Journal of Nuclear Materials* **313-316** 1119–1122

[32] Tskhakaya D *et al*, 2007 *Contributions to Plasma Physics* **47(8-9)** 563–594

[33] Birdsall C K, 1985 *Plasma Physics via Computer Simulation*. McGraw-Hill, New York

[34] Pitcher C S and Stangeby P C, 1997 *Plasma Physics and Controlled Fusion* **39(6)** 779

[35] Fundamenski W, 2010 *Power Exhaust in Fusion Plasmas*, chap. 7.1. Cambridge University Press

[36] Braginskii S I, 1965 In M A Leontovich, ed., *Reviews of Plasma Physics*, vol. 1. Consultants Bureau, New York, 205

[37] Spitzer L and Härm R, 1953 *Physical Review* **89(5)** 977–981

[38] Boedo J, 2009 *Journal of Nuclear Materials* **390-391** 29–37

[39] Naulin V, 2007 *Journal of Nuclear Materials* **363-365** 24–31

[40] LaBombard B *et al*, 2000 *Nuclear Fusion* **40(12)** 2041

[41] Garcia O E *et al*, 2007 *Plasma Physics and Controlled Fusion* **49(12B)** B47

[42] Wiesen S *et al*, 2010 *Journal of Nuclear Materials* **In Press, Corrected Proof**

[43] Havlíčková E *et al*, 2010 *Journal of Nuclear Materials* **In Press, Corrected Proof**

[44] Chankin A V *et al*, 2007 *Journal of Nuclear Materials* **363-365** 335–340

[45] Chankin A V *et al*, 2009 *Nuclear Fusion* **49**. 015004

[46] Batishchev O V *et al*, 1997 *Physics of Plasmas* **4** 1672–80

[47] Horacek J *et al*, 2003 *Journal of Nuclear Materials* **313-316** 931–935

[48] Loarte A *et al*, 1998 *Nuclear Fusion* **38(3)** 331

[49] Krasheninnikov S I, Pigarov A Y and Sigmar D J, 1996 *Physics Letters A* **214(5-6)** 285–291

[50] Wischmeier M *et al*, 2004 *Contributions to Plasma Physics* **44(1-3)** 268–273

[51] Wischmeier M *et al*, 2009 *Journal of Nuclear Materials* **390-391** 250–254

[52] Coster D, 2011 *Journal of Nuclear Materials* **In Press, Corrected Proof**

[53] ITER Physics Expert Group on Divertor *et al*, 1999 *Nuclear Fusion* **39(12)** 2391

[54] Kallenbach A *et al*, 2011 *Journal of Nuclear Materials* **In Press, Corrected Proof**

[55] Erents S K *et al*, 2000 *Plasma Physics and Controlled Fusion* **42(8)** 905

[56] Gunn J *et al*, 2007 *Journal of Nuclear Materials* **363-365** 484–490

[57] Pitts R A, Horacek J and the TCV Team, 2007 In *Proceedings of the 34th EPS Conference on Plasma Physics*. O4.007

[58] LaBombard B *et al*, 2004 *Nuclear Fusion* **44(10)** 1047

[59] Pitts R *et al*, 2005 *Journal of Nuclear Materials* **337-339** 146–153

[60] Chankin A, 1997 *Journal of Nuclear Materials* **241-243** 199–213

[61] Wischmeier M *et al*, 2008 *Contributions to Plasma Physics* **48(1-3)** 249–254

[62] Asakura N, 2009 *Plasma and Fusion Research* **4** 021–021

[63] Erents S K *et al*, 2004 *Plasma Physics and Controlled Fusion* **46(11)** 1757

[64] Bonnin X *et al*, 2005 In ECA, ed., *Proceedings of the 32nd EPS Conference on Plasma Physics Tarragona*, vol. 29C. ECA. P-2.110

[65] Groth M *et al*, 2009 *Nuclear Fusion* **49(11)** 115 002

[66] Chankin A *et al*, 2007 *Nuclear Fusion* **47(5)** 479

[67] Chankin A *et al*, 2007 *Nuclear Fusion* **47(8)** 762

[68] Sigmund P, 1969 *Physical Review* **184(2)** 383–416

[69] Eckstein W *et al*, 1993 *Nuclear Instruments and Methods in Physics Research Section B: Beam Interactions with Materials and Atoms* **83(1-2)** 95–109

[70] Roth J, 1990 *Journal of Nuclear Materials* **176-177** 132–141

[71] Küstner M *et al*, 1998 *Nuclear Instruments and Methods in Physics Research Section B: Beam Interactions with Materials and Atoms* **145(3)** 320–331

[72] Bohdansky J, 1984 *Nuclear Instruments and Methods in Physics Research Section B: Beam Interactions with Materials and Atoms* **2(1-3)** 587–591

[73] Yamamura Y, Itikawa Y and Itoh N, 1983. *IPPJ-AM-26*

[74] Eckstein W *et al*, 1993. *IPP-report 9/82*

[75] Roth J, 2005 *Nuclear Fusion Research, Understanding Plasma-Surface Interactions*, chap. 9, Review and Status of Physical Sputtering and Chemical Erosion of Plasma Facing Materials. Springer

[76] Eckstein W *et al*, 2004 *Journal of Nuclear Materials* **328(1)** 55–61

[77] Davis J and Haasz A, 1997 *Journal of Nuclear Materials* **241-243** 37–51

[78] Roth J, 1999 *Journal of Nuclear Materials* **266-269** 51–57

[79] Horn A *et al*, 1994 *Chemical Physics Letters* **231(2-3)** 193–198

[80] Wittmann M and Küppers J, 1996 *Journal of Nuclear Materials* **227(3)** 186–194

[81] Roth J, 2006 *Physica Scripta* **2006(T124)** 37

[82] Eckstein W, 2002. *IPP-report 9/132*

[83] Roth J *et al*, 2004 *Nuclear Fusion* **44(11)** L21

[84] Roth J *et al*, 2005 *Journal of Nuclear Materials* **337-339** 970–974

[85] Krieger K *et al*, 2011 *Journal of Nuclear Materials* **In Press, Corrected Proof**

[86] Pitts R *et al*, 2011 *Journal of Nuclear Materials* **In Press, Corrected Proof**

[87] Federici G *et al*, 2001 *Nuclear Fusion* **41(12)** 1967

[88] Rohde V *et al*, 2011 *Journal of Nuclear Materials* **In Press, Corrected Proof**

[89] Doerner R, Baldwin M and Causey R, 2005 *Journal of Nuclear Materials* **342(1-3)** 63–67

[90] von Keudell A *et al*, 1999 *Nuclear Fusion* **39(10)** 1451

[91] Krieger K, Maier H and Neu R, 1999 *Journal of Nuclear Materials* **266-269** 207–216

[92] Mayer M *et al*, 2009 *Journal of Nuclear Materials* **390-391** 538–543

[93] Coad J *et al*, 2005 *Fusion Science and Technology* **48(1)**

[94] Matthews G *et al*, 2005 In *Proceedings of the 3Oth EPS Conference on Plasma Physics*. P3.198

[95] Paméla J *et al*, 2007 *Journal of Nuclear Materials* **363-365** 1–11

[96] Roth J *et al*, 2008 *Plasma Physics and Controlled Fusion* **50(10)** 103 001

[97] Pitts R A *et al*, 2009 *Physica Scripta* **2009(T138)** 014 001

[98] Kirschner A *et al*, 2004 *Journal of Nuclear Materials* **328(1)** 62–66

[99] Kirschner A *et al*, 2011 *Journal of Nuclear Materials* **In Press, Corrected Proof**

[100] Pitts R A *et al*, 2005 *Plasma Physics and Controlled Fusion* **47(12B)** B303

[101] Janev R K and Reiter D, 2002. *Jül report Jül-3966*

[102] Janev R K and Reiter D, 2003. *Jül report Jül-4005*

[103] Fussmann G *et al*, 1994 In *Plasma Physics and Controlled Nuclear Fusion Research (Proc. 15th Conf., Seville, 1994)*, vol. 2. 143

[104] Naujoks D *et al*, 1996 *Nuclear Fusion* **36(6)** 671

[105] Brooks J N, 1990 *Physics of Fluids B: Plasma Physics* **2(8)** 1858–1863

[106] Kreter A *et al*, 2009 *Journal of Nuclear Materials* **390-391** 38–43

[107] Strachan J *et al*, 2008 *Nuclear Fusion* **48(10)** 105 002

[108] Ueda Y *et al*, 2009 *Nuclear Fusion* **49(6)** 065 027

[109] Kallenbach A *et al*, 2011 *Nuclear Fusion* **51(9)** 094 012

[110] Neu R *et al*, 2009 *Physica Scripta* **2009(T138)** 014 038

[111] Neu R *et al*, 2007 *Plasma Physics and Controlled Fusion* **49(12B)** B59

[112] Gruber O *et al*, 2009 *Nuclear Fusion* **49(11)** 115 014

[113] Winter J, 1996 *Plasma Physics and Controlled Fusion* **38(9)** 1503

[114] Kallenbach A *et al*, 2009 *Nuclear Fusion* **49(4)** 045 007

[115] McCarthy P *et al*, 2003 In *Proceedings of the 30th EPS Conference on Plasma Physics*. P1.64

[116] McCarthy P J, 1992 *An Integrated Data Interpretation System for Tokamak Discharges*. Ph.D. thesis, University College Cork

[117] Schneider W *et al*, 2000 *Fusion Engineering and Design* **48(1-2)** 127–134

[118] Fischer R *et al*, 2008 *Plasma Physics and Controlled Fusion* **50(8)** 085 009

[119] Hicks N K *et al*, 2009 In J Lohr, ed., *the 15th Joint Workshop on Electron Cyclotron Emission and Electron Cyclotron Resonance Heating (EC-15)*. World Scientific, Singapore

[120] Hutchinson I H, 1988 *Physical Review A* **37(11)** 4358–4366

[121] Müller H *et al*, 2005 In *Proceedings of the 32nd EPS Conference on Plasma Physics*. P1.009

[122] Weinlich M and Carlson A, 1997 *Physics of Plasmas* **4(6)** 2151–2160

[123] Kallenbach A *et al*, 2007 In *Proceedings of the 34th EPS Conference on Plasma Physics*. P1.063

[124] G H and H-S B, 1998 *Vacuum* **51(1)** 39–46

[125] Harhausen J, 2008 *Interpretation of D_α Imaging Diagnostics Data on the ASDEX Upgrade Tokamak*. Ph.D. thesis, Ludwig-Maximilians-Universität München

[126] Brezinsek S *et al*, 2007 *Journal of Nuclear Materials* **363-365** 1119–1128

[127] Brezinsek S *et al*, 2004 *Physica Scripta* **2004(T111)** 42

[128] Esser H G *et al*, 2003 *Fusion Engineering and Design* **66-68** 855–860. 22nd Symposium on Fusion Technology

[129] Coad J P *et al*, 2009 *Physica Scripta* **2009(T138)** 014 023

[130] Naujoks D *et al*, 1993 *Nuclear Fusion* **33(4)** 581

[131] Rubel M J *et al*, 2004 *Journal of Nuclear Materials* **329-333(Part 1)** 795–799

[132] Wienhold P *et al*, 2001 *Journal of Nuclear Materials* **290-293** 362–366

[133] Brezinsek S *et al*, 2009 *Physica Scripta* **2009(T138)** 014 022

[134] Kögler U *et al*, 1997 *Journal of Nuclear Materials* **241-243** 816–820

[135] Kreter A *et al*, 2008 *Plasma Physics and Controlled Fusion* **50(9)** 095 008

[136] Kreter A *et al*, 2007 *Journal of Nuclear Materials* **363-365** 179–183

[137] Likonen J *et al*, 2003 *Fusion Engineering and Design* **66-68** 219–224

[138] Likonen J *et al*, 2011 *Journal of Nuclear Materials* **In Press, Corrected Proof**

[139] Vainonen-Ahlgren E *et al*, 2005 *Journal of Nuclear Materials* **337-339** 55–59

[140] Vainonen-Ahlgren E *et al*, 2007 *Journal of Nuclear Materials* **363-365** 270–275

[141] Allen S *et al*, 2005 *Journal of Nuclear Materials* **337-339** 30–34

[142] Wampler W *et al*, 2007 *Journal of Nuclear Materials* **363-365** 72–77

[143] Pugno R *et al*, 2005 *Journal of Nuclear Materials* **337-339** 985–989

[144] Coad J *et al*, 2007 *Journal of Nuclear Materials* **363-365** 287–293

[145] Elder J *et al*, 2011 *Journal of Nuclear Materials* **In Press, Corrected Proof**

[146] Likonen J *et al*, 2011 *Physica Scripta* **submitted**. 13th International Workshop on Plasma-Facing Materials and Components for Fusion Applications

[147] Wienhold P, Weschenfelder F and Winter J, 1994 *Nuclear Instruments and Methods in Physics Research Section B: Beam Interactions with Materials and Atoms* **94(4)** 503–510

[148] McLean A G *et al*, 2009 *Review of Scientific Instruments* **80(4)** 043501

[149] Koltunov M and Tokar M Z, 2011 *Plasma Physics and Controlled Fusion* **53(6)** 065 015

[150] Tokar M Z, Ding R and Koltunov M, 2010 *Plasma Physics and Controlled Fusion* **52(7)** 075 003

[151] Ding R *et al*, 2011 *Journal of Nuclear Materials* **In Press, Corrected Proof**

[152] Stangeby P and Elder J, 1995 *Nuclear Fusion* **35(11)** 1391

[153] Braams B J, 1987. *A multifluid code for simulation of the edge plasma in tokamaks*. NET report EUR-FU/XII-80/87/68

[154] Taroni A *et al*, 1992 *Contributions to Plasma Physics* **32(3-4)** 438–443

[155] Rognlien T D *et al*, 1994 *Contributions to Plasma Physics* **34(2-3)** 362–367

[156] Reiter D, 2011. *Eirene manual*. www.eirene.de

[157] Stotler D and Karney C, 1994 *Contributions to Plasma Physics* **34(2-3)** 392–397

[158] Cupini E, 1984. *NIMBUS-Monte Carlo simulation of neutral particle transport in fusion devices*. EUR-FU/XII-324/9

[159] Bonnin X, Kukushkin A and Coster D, 2009 *Journal of Nuclear Materials* **390-391** 274–277

[160] Kukushkin A *et al*, 2007 *Journal of Nuclear Materials* **363-365** 308–313

[161] Balescu R, 1988 In *Transport processes in Plasmas*. North Holland, New York, 230

[162] Baelmans M, 1993. *Jül report Jül-2891*

[163] Marchand R and Dumberry M, 1996 *Computer Physics Communications* **96** 232–246

[164] Bonnin X and Coster D, 2011 *Journal of Nuclear Materials* **In Press, Corrected Proof**

[165] Coster D P, Bonnin X and Warrier M, 2006 *Physica Scripta* **2006(T124)** 9

[166] Coster D *et al*, 2007 *Journal of Nuclear Materials* **363-365** 136–139

[167] Rozhansky V *et al*, 2009 *Nuclear Fusion* **49(2)** 025 007

[168] Kotov V, Reiter D and Kukushkin A S, 2007. *Jül report Jül-4257*

[169] Coster D *et al*, 2002 In *Proceedings of 19th Fusion Energy Conference*. Lyon

[170] Bonnin X *et al*, 2002 *Contributions to Plasma Physics* **42(2-4)** 175–180

[171] Fundamenski W, 2005 *Plasma Physics and Controlled Fusion* **47** R163–R208

[172] Hynönen V, 2008 *Orbit-following simulation of fast ions in ASDEX Upgrade tokamak in the presence of magnetic ripple and radial electric field*. Ph.D. thesis, Helsinki University of Technology

[173] Hynönen V *et al*, 2007 *Plasma Physics and Controlled Fusion* **49** 151–74

[174] Kurki-Suonio T *et al*, 2006 *Plasma Physics and Controlled Fusion* **48** 1413–24

[175] Sipilä S K, 1993. *Simulation of charged particle orbits in a tokamak*. Licentiate thesis, Helsinki University of Technology

[176] The ERO code is property of Forschungszentrum Jülich

[177] Summers H P, 2004. *The ADAS User Manual, version 2.6*. http://www.adas.ac.uk

[178] Kirschner A *et al*, 2009 *Journal of Nuclear Materials* **390-391** 152–155

[179] Kögler U and Winter J, 1997. *Jül report Jül-3361*

[180] Biersack J and Haggmark L, 1980 *Nuclear Instruments and Methods* **174(1-2)** 257–269

[181] Biersack J P and Eckstein W, 1984 *Applied Physics A: Materials Science and Processing* **34** 73–94

[182] Eckstein W and Urbassek H, 2007 In *Sputtering by Particle Bombardment*, vol. 110 of *Topics in Applied Physics*. Springer Berlin / Heidelberg, 21–31

[183] Alman D A and Ruzic D N, 2004 *Physica Scripta* **2004(T111)** 145

[184] Urbassek H M, 1997 *Nuclear Instruments and Methods in Physics Research Section B: Beam Interactions with Materials and Atoms* **122(3)** 427–441

[185] Airila M *et al*, 2009 *Journal of Nuclear Materials* **390-391** 175–178

[186] Droste S *et al*, 2008 *Plasma Physics and Controlled Fusion* **50(1)** 015 006

[187] Droste S *et al*, 2006 *Contributions to Plasma Physics* **46(7-9)** 628–634

[188] Mutzke A *et al*, 2011. *SDTrimSP Version 5.00, IPP-report 12/8*

[189] Eckstein W, 2008 *Vacuum* **82(9)** 930–934

[190] Abramov V *et al*, 1989 *Journal of Nuclear Materials* **162-164** 462–466

[191] Borodin D *et al*, 2011 *Journal of Nuclear Materials* **In Press, Corrected Proof**

[192] Ohya K and Kirschner A, 2009 *Physica Scripta* **2009(T138)** 014 010

[193] Kirschner A *et al*, 2003 *Plasma Physics and Controlled Fusion* **45(3)** 309

[194] Airila M *et al*, 2011 *Journal of Nuclear Materials* **In Press, Corrected Proof**

[195] Kirschner A *et al*, 2007 *Journal of Nuclear Materials* **363-365** 91–95

[196] Kirschner A *et al*, 2009 *Physica Scripta* **2009(T138)** 014 011

[197] Federici G *et al*, 2003 *Journal of Nuclear Materials* **313-316** 11–22

[198] Shimada M *et al*, 2009 *Journal of Nuclear Materials* **390-391** 282–285

PUBLICATION I

ASCOT simulations of electron energy distribution at the divertor targets in an ASDEX Upgrade H-mode discharge

In: Plasma Physics and Controlled Fusion 50
(2008) 065021 (13 pp).

Plasma Phys. Control. Fusion **50** (2008) 065021 (13pp) doi:10.1088/0741-3335/50/6/065021

ASCOT simulations of electron energy distribution at the divertor targets in an ASDEX Upgrade H-mode discharge

L K Aho-Mantila[1], T Kurki-Suonio[1], A V Chankin[2], D P Coster[2] and S K Sipilä[1]

[1] Helsinki University of Technology, Association Euratom-TEKES, FIN-02015 TKK, Finland
[2] Max-Planck-Institut für Plasmaphysik, EURATOM Association, D-85748 Garching, Germany

E-mail: leena.aho-mantila@tkk.fi

Received 29 October 2007, in final form 14 March 2008
Published 19 May 2008
Online at stacks.iop.org/PPCF/50/065021

Abstract

Electron energy distribution at the divertor targets was calculated with the Monte Carlo code ASCOT for an ASDEX Upgrade H-mode discharge. The scrape-off layer (SOL) plasma background was obtained from the edge fluid code SOLPS. The orbit-following of test particles was performed assuming a fixed Maxwellian plasma background, accounting for the effects of the magnetic geometry, Coulomb interaction with the background and a prescribed electric potential. The energies recorded from the electrons impinging on the divertor targets indicated that, close to the plates, there should be strong deviations from the thermal Maxwell–Boltzmann distribution. In addition, details of the magnetic geometry and parallel plasma temperature and density profiles were observed to significantly impact the target energy distributions. The obtained discrepancy between the Monte Carlo and fluid results indicates a lack of self-consistency in fluid modelling due to kinetic effects in a medium-collisionality SOL.

(Some figures in this article are in colour only in the electronic version)

1. Introduction

The dynamics of a tokamak plasma can be investigated on a large scale by modelling the plasma as a fluid. This approach yields reasonable results provided that the plasma has sufficiently high collisionality for the fluid treatment to be valid. Most of the present-day edge plasma codes such as B2-Eirene [1] and EDGE2D-Nimbus [2, 3] employ the fluid picture. However, due to the low collisionality of the scrape-off layer (SOL), a lot of the crucial edge plasma phenomena may result from kinetic behaviour of the plasma particles that, for one, cannot be accounted for

0741-3335/08/065021+13$30.00

by employing fluid dynamics [4]. Complete kinetic modelling presents a tremendous challenge for current edge plasma codes and, for this reason, it is of urgent importance to investigate to what extent the fluid model remains justified in the plasma edge [5, 6].

This paper aims at determining whether the assumption of a Maxwell–Boltzmann energy distribution of electrons holds in a medium-collisionality SOL. The orbit-following Monte Carlo code ASCOT [7] is employed in simulating the guiding-centre motion of electrons travelling from the outer plasma midplane through an ASDEX Upgrade (AUG) high-confinement mode (H-mode) SOL plasma to the divertor plates. The interaction of the test particles with the fixed plasma background supplied by the SOLPS code [1] is implemented via Monte Carlo operators for small-angle Coulomb collisions, with the underlying assumption of a Maxwell–Boltzmann energy distribution in the plasma background. In addition, the electric potential profile calculated with SOLPS is employed in order to account, to a certain extent, for the SOL parallel electric field. The degree of thermalization of the electron ensemble is estimated by inspecting the energy distributions recorded at the divertor plates, hereafter referred to as *target distributions*. The results are completed with a detailed investigation of the collisional properties of the electrons along the field lines.

The target distributions obtained with ASCOT are observed to be affected by both the upstream and target background plasma temperatures. In addition, the distribution of energy and particles along the field lines has a significant effect on the thermalization of SOL electrons. Overall, it is observed that the collisionality of the SOL is insufficient for thermalizing all the electrons propagating to the target, and the deviations from the Maxwell–Boltzmann distribution are severe enough to render the fluid model inappropriate for the medium-collisionality edge plasma.

The paper is organized as follows. Section 2 describes the SOL properties in the H-mode discharge under investigation. In section 3, the reader is first briefly introduced to the ASCOT simulation environment, and the set-up for the electron simulations is presented. The simulation results are given and discussed here. The conclusions are presented in section 4.

2. Hot electrons in H-mode SOL

H-mode discharges are characterized by the formation of a transport barrier in the plasma edge. Due to the high confinement achieved with the barrier, the core plasma density and pressure are increased from the low-confinement (L-)mode. This produces steep radial density and temperature gradients to the plasma edge, marking out a region known as the plasma *pedestal*. Outside the pedestal, the SOL has relatively low density. H-mode is typically achieved with divertor tokamaks. In divertor operation, also significant parallel temperature and density gradients are observed in the SOL as a result of ionization of neutrals recycled from the target. With respect to the parallel motion of the SOL particles, these gradients could be too steep for fluid behaviour to persist at each poloidal location in SOL.

Of particular concern in SOL modelling is the possible kinetic behaviour of electrons. Electrons are the dominating species in the formation of the sheath potential at material surfaces that determines to a large extent the radial electric field and, hence, the $E \times B$ drift in the divertor and SOL region. Measurements of the sheath potential typically rely on the assumption of a Maxwellian electron energy distribution and may fail to give correct results in the presence of collisionless electrons (see [8] and references therein). Furthermore, hot electrons with velocities $v = 3 - 5v_{\mathrm{th}}$ contribute most to the parallel electron heat flux [4, 9] and, thus, even small deviations from the Maxwell–Boltzmann distribution significantly affect the target

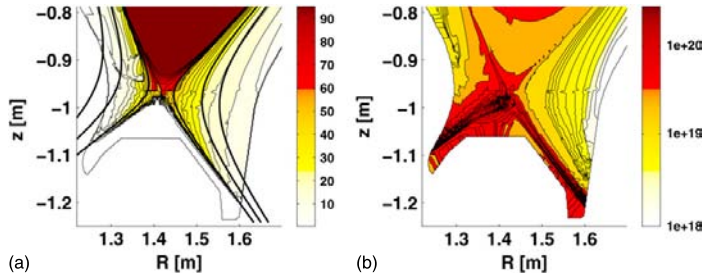

Figure 1. Electron temperature (eV) (*a*) and density (m^{-3}) (*b*) profiles showing the strong parallel gradients estimated by SOLPS for the divertor region. In (*a*), also the flux surfaces with $\rho = 1.001$, 1.01 and 1.02 are shown as thick black lines.

temperature, density and heat deposition, ultimately influencing the SOL transport. Recently, these kinetic effects have been of considerable concern in edge modelling [10].

2.1. ASDEX Upgrade discharge #17151

The H-mode plasma background investigated in this paper is the AUG discharge #17151 at the time slice of 4.138 s, corresponding to an inter-ELM period. The toroidal plasma current is 0.8 MA, and the toroidal magnetic field at the centre of the chamber is 2.0 T. The central electron density is 7.2×10^{19} m^{-3}, decreasing to 1.4×10^{19} m^{-3} at the separatrix. The ASCOT simulations take into account only one background ion species, deuterium.

The relevant edge plasma parameters are obtained from a SOLPS [1] fluid solution based on a vast amount of experimental data from this discharge. The SOLPS modelling of this discharge is described in detail in [11]. The edge profiles produced by SOLPS are especially adjusted to match measurement data for the outer midplane and outer target and, hence, should be most accurate on the low-field side. For this reason, the main focus of this paper is also on the outer target distributions.

Figure 1 shows the 2D SOLPS electron temperature and density profiles, after being interpolated to the Cartesian ASCOT grid [7]. Above the X-point, the interpolation of background parameters from SOLPS grid [12] to ASCOT is done bilinearly in (ρ, θ), while elsewhere the values result from linear interpolation between SOLPS cell corners. SOLPS predicts steep gradients close to the targets, mainly due to ionization of neutral particles.

Figure 2 shows the parallel profile of the electric potential just outside the separatrix, as calculated by SOLPS. ASCOT calculates the electric field effects from this prescribed potential, excluding any additional charge imbalance created during the simulations (see [13] and references therein). Calculating the electric field self-consistently is, unfortunately, beyond the capabilities of ASCOT. The resulting fixed parallel electric field is observed to first accelerate the electrons travelling towards the plates and, only after passing the X-point, become strongly electron-repelling.

In table 1, estimates for the field line-averaged collisionality near the separatrix are given. The numbers describe the collisionality of a suprathermal electron, emerging from the core at the outer midplane (collision frequencies defined in [14]). The SOL collisionality ν^* is defined here as the magnetic connection length, L_c, divided by the collisionless mean-free-path, λ_c (being hence the inverse of the *Knudsen number* $K = \lambda_c / L_c$). According to the estimates, the electron–ion collisionality is weak especially on the way to the outer divertor plate, and

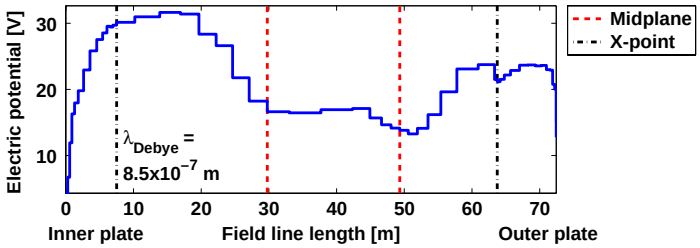

Figure 2. Parallel electric potential profile just outside the separatrix, as calculated by SOLPS. The field line length is measured from the inner divertor plate.

Table 1. Field line-averaged plasma parameters together with various estimates for the collisionality along the flux surfaces of interest. The calculations are performed for an energetic electron with $E = 3k_B T_{omp}$, where T_{omp} is the background temperature at the outer midplane, see table 2.

	From omp to inner target			From omp to outer target		
Flux surface	1.001	1.01	1.02	1.001	1.01	1.02
Average parameters:						
Connection length [m]	55.2	43.9	39.9	30.8	20.1	16.7
Average electron density [10^{18}m^{-3}]	34.6	11.6	6.55	37.1	10.3	6.05
Average electron temperature [eV]	58.7	26.8	20.6	56.2	27.0	20.4
Average ion density [10^{18}m^{-3}]	33.8	11.3	6.16	36.4	9.88	5.61
Average ion temperature [eV]	96.3	66.2	61.6	90.0	71.0	63.5
Electron–electron collisions:						
Mean-free-path, λ_c [m]	9.9	5.7	5.4	9.3	6.4	5.8
No of pitch-changing collisions	2.7	3.7	3.5	1.6	1.5	1.4
No of energy-changing collisions	2.9	4.0	3.8	1.7	1.6	1.5
Collisionality, ν^*_{ee}	5.6	7.7	7.4	3.3	3.1	2.9
Electron–ion collisions:						
Mean-free-path, λ_c [m]	17.6	9.7	17.5	16.6	10.9	19.1
No of pitch-changing collisions	3.1	4.6	2.3	1.9	1.8	0.9
No of energy-changing collisions	0.0	0.0	0.0	0.0	0.0	0.0
Collisionality, ν^*_{ei}	3.1	4.6	2.3	1.9	1.8	0.9

the collisions merely change the pitch of the electron, not the energy. The electron–electron collisionality can, however, be significant with ν^* around 2.9–3.3 on the low-field side and 5.6–7.7 on the high-field side.

3. ASCOT simulations

3.1. Description of the ASCOT code

ASCOT [7] is an orbit-following Monte Carlo code, developed in the 1990s as a collaboration between TKK and VTT (Technical Research Center of Finland). It calculates the guiding-centre orbits of charged particles by integrating the guiding-centre equations of motion over discrete time steps [15]. In between the guiding-centre steps, the velocity components and/or position of the particle are altered by Monte Carlo operators that account for effects such as

Coulomb collisions, radio-frequency heating and anomalous transport. The Coulomb collision operators, which are the only relevant Monte Carlo operators for the present modelling, are derived from the Fokker–Planck equation assuming non-relativistic field particles with Maxwell–Boltzmann energy distribution. Separate collision operators are used for evaluating the change in particle energy and pitch (see detailed description in [15, 16]).

ASCOT employs prescribed magnetic and plasma background data that typically comes from experiments (AUG, JET). The magnetic background data is usually two-dimensional, but even toroidal variation can be taken into account in order to model ripple effects [15]. The 2D data grid is Cartesian, with 600×600 grid points. The plasma background data are either taken as a flux function ($\rho < 1$) or interpolated into the 2D Cartesian grid ($\rho > 1$). This paper presents the first ASCOT simulations that rely completely on plasma parameters outside the separatrix.

The test particles are simulated with ASCOT until they hit a material structure, such as the vessel wall or divertor target, or when one of the computational end criteria is met. The latter are set by the user as required by the specific problem. In our electron simulations essentially either of two things can happen: (1) the electron hits the target plate, or (2) the electron is thermalized and becomes part of the SOL bulk plasma. Since there is no reason to follow the latter particles until they diffuse to the wall or divertor, a maximum simulation time of 0.2 s is set for each electron. Furthermore, each particle is also assigned a CPU time maximum of 800 s for anomalous situations where a particle might get numerically stuck, for instance, in a grid irregularity. Limiting the CPU time is of particular importance in these electron simulations, because of the large amount of computation required for calculating the light-particle orbits on open field lines where acceleration of interaction time scales [7] is infeasible.

3.2. Simulation parameters

The parallel temperature and density profiles in SOL differ between flux surfaces. For investigating how the various conditions affect the thermalization of a midplane electron ensemble, several initial locations from just outside the separatrix to a centimetre away from it are considered ($\rho = 1.001$, 1.01 and 1.02). According to table 1, the electron–electron collisionality should be of the same order on all these flux surfaces. Table 2 shows the relevant background parameters on the midplane and at the target locations. The flux surface just outside the separatrix has, besides the longest connection length, also the strongest variation of plasma parameters.

The electrons have initially a uniform pitch distribution, corresponding to isotropic velocity distribution. For the initial energy distribution, three cases are considered: $T_{\mathrm{M-B}} = mT_{\mathrm{omp}}$, where T_{omp} is the local electron temperature at the point of initialization and $m = 1, 2, 3$. The higher temperatures are used to model situations in which the electron population emerging from inside the separatrix is not thermalized to the local SOL temperature, but carries excess energy from the core. For good statistics of the high-energy tail, the electrons are initialized uniformly in energy up until $10k_{\mathrm{B}}T_{\mathrm{M-B}}$, having weight factors given by the Maxwell–Boltzmann distribution.

In order to accurately account for abrupt variations in both SOL background parameters and the motion of the test particles, considerable care is given for adjusting the time step in the electron simulations. The length of the time step Δt is restricted by the following criteria: (1) Δt should not be longer than $N_{\mathrm{tb}} = 1/250$ times the *bounce time*, i.e. the time to complete an orbit (applicable only above X-point). (2) Δt must be smaller than 1/10 of the collision time, t_{coll}. (3) During Δt, the parallel velocity or various drifts do not move the guiding centre poloidally further than 0.05 or $2\pi N_{\mathrm{tb}}$ times the plasma minor radius, respectively. The latter

Table 2. Background electron parameters on the simulated flux surfaces. 'ot' and 'it' refer to the outer and inner divertor plate, respectively, and 'omp' refers to the initial location at the outer midplane.

ρ	T_{omp} [eV]	T_{it} [eV]	T_{ot} [eV]	n_{omp} [m^{-3}]	n_{it} [m^{-3}]	n_{ot} [m^{-3}]
1.001	79.8	2.2	4.1	1.40×10^{19}	2.31×10^{20}	2.34×10^{20}
1.01	34.1	6.3	12.6	8.17×10^{18}	1.94×10^{19}	2.12×10^{19}
1.02	24.7	9.9	13.8	6.09×10^{18}	7.28×10^{18}	1.08×10^{19}

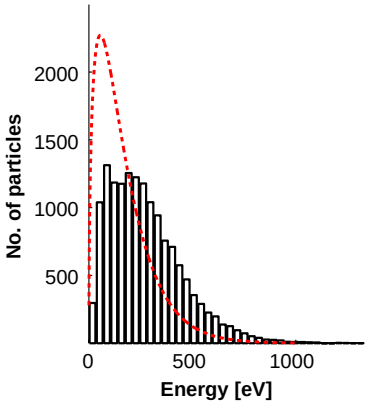

Figure 3. Outer target energy distribution, presented as a histogram (bin width 35 eV), for thermal electrons initialized at the outer midplane with $\rho = 1.02$ and followed through a homogeneous background plasma ($n_{\mathrm{e}} = n_{\mathrm{i}} = 1.5 \times 10^{19}\,\mathrm{m}^{-3}$, $T_{\mathrm{e}} = T_{\mathrm{i}} = 111\,\mathrm{eV}$ and $E_{\parallel} = 0$). The background plasma energy distribution is represented by the dashed line. The average energy of the target distribution is 270 eV, and the target distribution has a peak around $3k_{\mathrm{B}}T/2$.

restriction is rarely needed in the simulations, as the drift velocities for electrons are very low compared with v_{th}.

3.3. Electron simulations in SOL

3.3.1. Special features in SOL environment. The proper working of the ASCOT collision operators was verified by simulating the electrons first on closed field lines. After a sufficiently long simulation time, the electrons propagating in an isothermal plasma with constant density were brought to a Maxwell–Boltzmann energy distribution. Setting then the same conditions to the open field lines and recording the energies at the target plates revealed that the energy of an initially Maxwellian electron ensemble was actually increased during the propagation in SOL. Figure 3 shows the distribution recorded at the target, for an initially thermal ensemble at the outer midplane.

The two observations may seem contradictory at first, but can be explained by considering the simulation set-up. Firstly, the electrons reach the target plates at various time instants. At each poloidal location in SOL, there is a critical parallel velocity above which an electron is likely to be brought directly to the target. The ensemble of electrons launched at a specific instant of time is, hence, constantly depleted by the removal of electrons experiencing a favourable upward shift in energy while propagating through the SOL. Secondly, the depletion

Table 3. Statistics from the simulation results at $\rho = 1.01$ and $\rho = 1.02$, when total number of electrons initialized is $N_{\mathrm{omp}} = 20\,000$. All energy values are in electron volts, and the statistical error in the target energies is ∼5%.

ρ	$T_{\mathrm{M-B}}$	$E_{\mathrm{omp,ave}}$	N_{it}	N_{ot}	$E_{\mathrm{it,ave}}$	$E_{\mathrm{ot,ave}}$
1.01	T_{omp}	51	5589	14 412	25.2	44.9
	$2T_{\mathrm{omp}}$	102	5652	14 349	26.2	46.2
	$3T_{\mathrm{omp}}$	154	5618	14 383	30.4	52.2
1.02	T_{omp}	37	4823	15 178	19.6	49.3
	$2T_{\mathrm{omp}}$	74	4885	15 116	20.0	50.4
	$3T_{\mathrm{omp}}$	111	4948	15 053	24.0	55.5

of energy is not taken into account in the plasma, where the background temperature remains fixed. Hence, the cold electrons remaining in the SOL soon replenish the vacant higher energies in the Maxwell–Boltzmann distribution via collisions, and the distribution observed at the target becomes shifted from that of the background. This evident lack of self-consistency in ASCOT results restricts the quantitative analysis, but should not prevent benchmarking the fluid model in the edge.

The effect of several physical mechanisms on the thermalization of SOL electrons was investigated, and the following results were obtained: (1) Excluding test electron collisions with the background ions has practically no effect on the target energy distributions and, hence, the ion temperature and density profiles can be concluded to have a negligible role in the energy distribution of SOL electrons. This is an expected result, as the electron–ion energy exchange has a very low time scale, recall table 1. (2) Including anomalous radial transport with transport coefficient of maximum 1 $\mathrm{m}^2\,\mathrm{s}^{-1}$ does not affect the target distributions. (3) Including a fixed parallel electric field in the model increases the simulation times but has a negligible effect on the target distributions.

3.3.2. Target energy distributions at $\rho = 1.01 - 1.02$. The suite of simulations with realistic background parameters shows that only one quarter to one third of the electrons end up on the inner divertor plate, while the rest are brought to the outer plate. This can be concluded to be a direct consequence of the connection lengths to the targets differing roughly by a factor of 2, recall table 1. Table 3 shows the statistics of the simulation results for the two outermost flux surfaces, $\rho = 1.01 - 1.02$. The fraction of electrons impinging on the outer target ($N_{\mathrm{ot}}/N_{\mathrm{omp}}$) varies somewhat with the flux surface, but does not depend on the initial energy of the distribution. The average target energies are much higher than the divertor temperatures predicted by SOLPS fluid calculations, and they are found to weakly increase with the initial energy of the ensemble. Inner target energies lower than the outer target energies are in accordance with the estimated target electron temperatures, recall table 2.

The target energy distributions at $\rho = 1.01$, for the case of thermal initial ensemble, are shown in figure 4. Target distributions at $\rho = 1.02$ are similar in form. At the outer target, the distribution is close to Maxwellian with temperature around T_{omp}. A fraction of the electrons seems to have increased their energies on the way to the target, similarly to the case shown in figure 3. At the inner target, the distribution has a large, almost thermalized component. In addition, there is an excessive number of electrons in the high-energy tail of the distribution. The effect of the hot electron component on the target heat load is, however, small even with initially suprathermal ensembles.

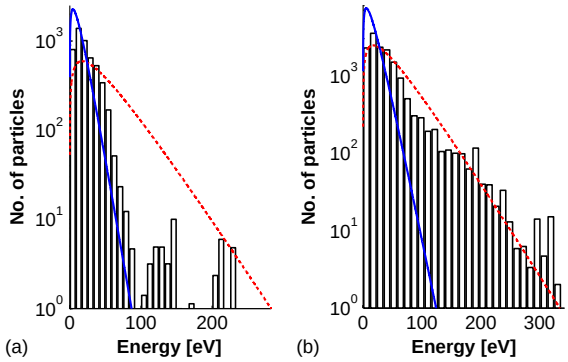

Figure 4. Electron target energy distributions, presented as histograms (bin widths 8.4 eV and 11.6 eV at the inner and outer plate, respectively), on the flux surface 0.5 cm apart from the outer midplane separatrix, $\rho = 1.01$. The solid line represents the background Maxwell–Boltzmann energy distribution at the plate, as predicted by the SOLPS code. The dashed line gives the initial energy distribution of those electrons recorded at the target, corresponding to T_{omp}.

Table 4. Statistics from the simulation results at $\rho = 1.001$ when total number of electrons initialized is 20 000. A fraction of the electrons (≈10%) was lost due to the simulation time limitation, but this could be shown not to affect the principal results. All energy values are in electron volts, and the statistical error in the target energies is ∼5%.

ρ	$T_{\mathrm{M-B}}$	$E_{\mathrm{omp,ave}}$	N_{it}	N_{ot}	$E_{\mathrm{it,ave}}$	$E_{\mathrm{ot,ave}}$
1.001	T_{omp}	120	5010	13 136	8.6	17.3
	$2T_{\mathrm{omp}}$	240	5128	13 069	11.3	20.9
	$3T_{\mathrm{omp}}$	359	4884	13 333	26.2	40.1

3.3.3. Target energy distributions at $\rho = 1.001$. Distinctly different results are obtained for the innermost flux surface with $\rho = 1.001$ than for those at the outermost locations. Table 4 shows the statistics of these simulations. The distribution of electrons between the two target plates is again found to be independent of the initial energy of the ensemble. The average target energies, however, increase significantly as more energetic initial ensembles are investigated. At the inner target, for example, the average energy in the $m = 3$ case retains the three times higher value than that in the $m = 1$ (thermal) case.

Figure 5 shows the target energy distributions at $\rho = 1.001$, for the initially thermal case. At both plates, a high thermal peak at low energies corresponding to the divertor temperature is observed. At the outer plate, the thermal peak is accompanied by a significant number of electrons at suprathermal energies. Compared with the outermost flux surfaces, the distributions at $\rho = 1.001$ seem drastically different in form. The division into two components is apparently related to the temperature difference between the midplane and the target and, this being relatively small at $\rho = 1.01$–1.02, such a division is scarcely visible at the outermost locations.

Close to the separatrix, the number of hot electrons is observed to increase at both targets when $m > 1$, increasing also the target heat loads. In table 5, the energy brought to the targets by suprathermal electrons ($E > 30$ eV) is compared with that of the thermal electrons ($E < 30$ eV), for the three different cases with $m = 1, 2, 3$. The hot electron component is found to be dominating even with the thermal initial ensemble, as 71% of the outer target

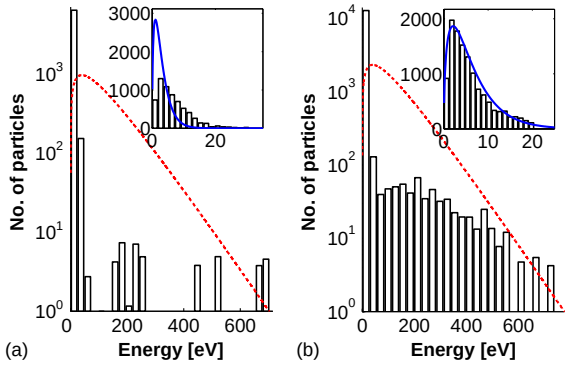

Figure 5. Electron target energy distributions, presented as histograms (bin widths 24.2 and 28.4 eV), on the flux surface closest to the separatrix, $\rho = 1.001$. The inset shows a zoom-in to the lowest energies (bin widths 1.2 and 1.8 eV). Representation otherwise as in figure 4.

Table 5. The total energy of the thermal peak ($E < 30$ eV), E_{th}, compared with the total energy of the suprathermal electrons ($E > 30$ eV), E_{sth}, for $\rho = 1.001$. 'it' and 'ot' refer to the inner and outer target, respectively. The suprathermal energy portion is significant, increasing with more energetic initial distributions. The thermal energy portion remains constant.

$T_{\mathrm{M-B}}$	$E_{\mathrm{it,th}}$ [keV]	$E_{\mathrm{it,sth}}$ [keV]	$E_{\mathrm{it,sth}}/E_{\mathrm{it,tot}}$	$E_{\mathrm{ot,th}}$ [keV]	$E_{\mathrm{ot,sth}}$ [keV]	$E_{\mathrm{ot,sth}}/E_{\mathrm{ot,tot}}$
T_{omp}	35	8	0.19	66	161	0.71
$2T_{\mathrm{omp}}$	35	23	0.40	66	207	0.76
$3T_{\mathrm{omp}}$	32	96	0.75	64	470	0.88

energy comes from this portion of electrons. Increasing the initial energy of the ensemble does not increase the energy of the thermal component at the target.

3.3.4. Identifying the collisional properties. Figure 6 shows the electron temperature and density profiles together with the electron–electron collisionality along the field lines at $\rho = 1.001$–1.02, on the way from the outer midplane to the outer target. At $\rho \geqslant 1.01$, the gradients in plasma parameters are quite small and the collisionality remains steady until the X-point is reached. According to the simulation results, recall table 3, the collisionality is sufficient to bring the initially suprathermal electron ensembles to the field line-averaged electron temperature. However, only at $\rho = 1.01$ does the abrupt increase in collisionality close to the target seem sufficient to thermalize a notable number of electrons to the target temperature.

The profiles at $\rho = 1.001$ differ from those further outside the separatrix. Above the X-point, the electron–electron collisionality is low and the background temperature remains rather high. Below the X-point, the collisionality increases to the same level as at $\rho = 1.01$, accompanied by a significant drop in the background temperature. Here, most of the electrons must be thermalized to the low target temperature, as was the case with $\rho = 1.01$ also. The tremendous effect of the remaining hot electron component on the target heat load at $\rho = 1.001$, recall table 5, apparently stems from the large temperature difference between the midplane and the target.

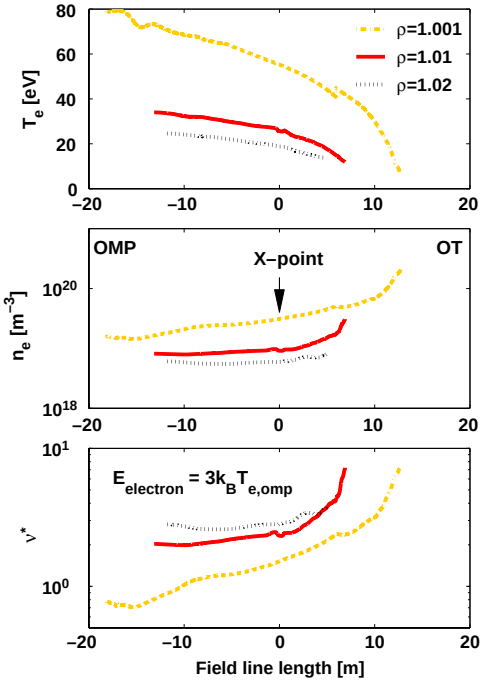

Figure 6. The two uppermost figures show the electron temperature and density in the SOL plasma along the simulated field lines, from the outer midplane to the outer target. The steepest gradients are observed in the region below the X-point (field line length $\geqslant 0$), due to ionization of neutral particles. The lowest figure shows the collisionality of a suprathermal electron with energy $E = 3k_{\mathrm{B}}T_{\mathrm{omp}}$, propagating along these field lines. For the sake of reference, the scale length L_{c} is taken to be the connection length at $\rho = 1.02$.

Table 6. Prompt kinetic losses, E_{kin}, recorded by ASCOT from 20 000 electrons initialized at the outer midplane with $\rho = 1.001$, compared with the theoretical energy content of a completely thermalized ensemble, E_{th} (assuming $N_{\mathrm{it}}/N_{\mathrm{ot}} = 3/7$ based on table 4).

$T_{\mathrm{M-B}}$	$E_{\mathrm{it,kin}}$ [keV]	$E_{\mathrm{it,kin}}/E_{\mathrm{it,th}}$	$E_{\mathrm{ot,kin}}$ [keV]	$E_{\mathrm{ot,kin}}/E_{\mathrm{ot,th}}$
T_{omp}	0.4	0.004	4.2	0.03
$3T_{\mathrm{omp}}$	101	2.2	335	2.9
$5T_{\mathrm{omp}}$	573	12	1565	14
$7T_{\mathrm{omp}}$	1326	28	3708	32

A more detailed inspection of the hot electron component observed at $\rho = 1.001$ reveals that it is only partly composed of collisionless electrons. Discarding those electrons that cool to the thermal energy from the simulation decreases dramatically the number of electrons recorded at the target. Table 6 shows the number of collisionless target electrons when initial ensembles with $m = 1, 3, 5, 7$ are used. From the initially thermal ensemble, only seven electrons reach the plates with energy continuously above 20 eV. This is a negligible number compared with

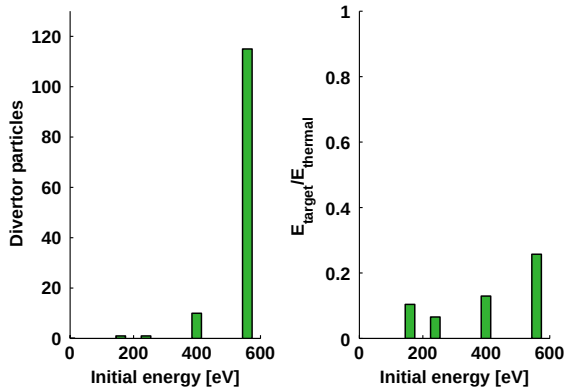

Figure 7. (Left) Number of kinetic electrons (energy continuously above 20 eV) recorded at the outer target, from the monoenergetic ensemble of 1000 electrons with $v = v_{\parallel}$ launched at the outer midplane ($\rho = 1.001$). (Right) Contribution of kinetic electrons to the target heat load, assuming a Maxwellian midplane plasma, compared with the theoretical heat load of electrons with $E = 3k_{\mathrm{B}}T_{\mathrm{ot}}/2$ in a completely thermalized ensemble of the same size.

the size of the suprathermal component observed in the target distributions, recall figure 5, accounting for only a small percentage of the target heat load. Significant prompt losses are observed only after increasing the initial energy above $T_{\mathrm{M-B}} = 3T_{\mathrm{omp}}$. This is further depicted in figure 7, showing prompt kinetic losses to the outer target from monoenergetic ensembles ($E_{\mathrm{ini}} = (1\text{–}7) \times k_{\mathrm{B}}T_{\mathrm{omp}}$). Although the fraction of high-energy electrons in a Maxwellian midplane plasma decreases with energy, the contribution of kinetic electrons to the target heat load increases with energy above $E_{\mathrm{ini}} = 3k_{\mathrm{B}}T_{\mathrm{omp}}$.

As the magnitude of the hot component at $\rho = 1.001$ cannot be explained by prompt losses, most of the suprathermal energy must come from the plasma at locations further downstream from the midplane. Setting a maximum of 20 eV for the background temperature experienced by the electrons in the $m = 1$ case removes the hot electron component from the target distributions, indicating that the origin of hot electrons must be somewhere around the X-point or upstream from it, where the plasma is sufficiently hot. Figure 8 shows the number of kinetic electrons recorded at the outer target, from 1000 monoenergetic electrons initialized at various locations both above and below the X-point, having initial pitch close to 1 (directed towards the outer divertor). The results indicate an energy threshold around 200 eV, below which the electrons do not have a chance of remaining collisionless. Higher initial energies give a finite probability for even the electrons above the X-point to remain kinetic.

The simulations indicate that, in addition to prompt kinetic losses from the outer midplane, also the high X-point temperature contributes to the hot electron component at the target. The effect of prompt losses becomes significant only with electron ensembles having initial energy above the thermal energy. At the outermost flux surfaces with $\rho \geqslant 1.01$, the high collisionality above the X-point prevents significant prompt losses and, for this reason, the average target energy remains constant even with initially more energetic ensembles. For modelling purposes, these are crucial results, as the target distributions are shown to have strong dependence on the plasma properties, not only at but also in between the midplane and target plates.

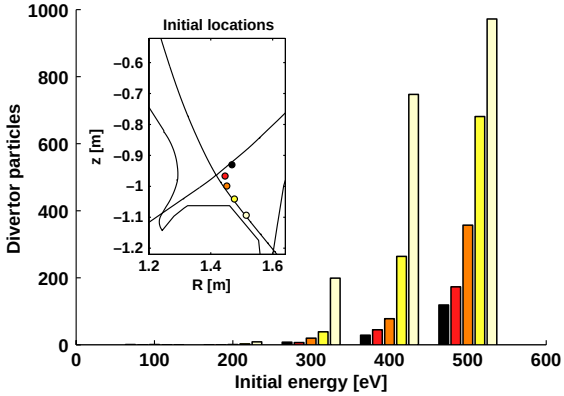

Figure 8. Kinetic electrons (energy continuously above 20 eV) recorded at the outer target, from the monoenergetic ensemble of 1000 electrons with $v = v_{\parallel}$ launched at various locations in the vicinity of the X-point ($\rho = 1.001$).

4. Conclusions

The orbit-following particle simulation code ASCOT was employed in modelling an electron ensemble in a tokamak plasma, travelling through the SOL to the divertor plates. The purpose was to investigate whether hot electrons emerging from the core plasma can propagate collisionless to the target and how the target heat load obtained with the Monte Carlo model agrees with the fluid model for the edge plasma. A well-diagnosed AUG H-mode discharge exhibiting strong temperature and density gradients in the SOL was chosen as a background for the modelling. The relevant parameters were obtained from a representative SOLPS fluid solution.

Several flux surfaces were considered, having the same collisionality on average ($\nu^* \approx 3.3$ (LFS), $\nu^* \approx 6.7$ (HFS)) but varying temperature and density profiles along the field line. Just outside the separatrix (at $\rho = 1.001$), the target distributions obtained with ASCOT had a large thermal peak that was accompanied by a smaller suprathermal electron component. The hot electron component was found to be largest at the outer target, where it significantly increased the target heat load. Further outside the separatrix (at $\rho = 1.01$–1.02), it was difficult to distinguish any thermalization to target temperature. In slight contrast, the initially suprathermal ensembles were brought to the same target distribution as the initially thermal ensemble. The statistics for the three radial positions are shown in tables 3 and 4, and the target distributions are depicted in figures 4 and 5.

After considering the temperature and density profiles along the field lines, presented in figure 6, the physics responsible for the obtained distributions could be understood. Steady collisionality along the field lines proved sufficient to bring even initially suprathermal electron ensembles close to the field line-averaged T_e. Thermalization to the target temperature occurred below the X-point, provided that the divertor plasma had sufficiently high collisionality. Nevertheless, when accompanied by a large temperature gradient, even the most collisional divertor plasmas allowed hot electrons to reach the target. Just outside the separatrix, this resulted in average target energies well above those predicted by the fluid calculations. The hot component in an otherwise thermal target distribution was shown to consist of electrons

remaining kinetic from various regions upstream of the target, and only a small fraction of the heat loads resulted from prompt kinetic electrons from the launching point at the outer midplane.

The ASCOT simulations presented in this paper were not, however, self-consistent. This means that quantitative conclusions about the energy distribution close to the divertor target cannot be made. In reality, the loss of suprathermal electrons to the targets would cool the divertor plasma, rendering it more collisional and more able to thermalize the electrons. In addition, non-Maxwellian energy distribution could change the electric field from that calculated by SOLPS, which would further affect the electron trajectories [13]. However, the large discrepancy obtained between the ASCOT results and the fluid model stresses the fact that kinetic effects must be considered in edge modelling.

From the results obtained one may conclude that the energy composition of electron losses is very sensitive to the distribution of the background electron density and temperature along the field lines. Close to the target, the plasma parameters are affected mainly by the ionization of neutral particles, and the SOLPS solution for this case suggested rather strong gradients near the strike point, recall figure 6. In the ASCOT simulations, the abrupt change in collisionality in the divertor region was found to determine the zone from where the bulk of the losses can occur. Detailed knowledge of the magnetic geometry and of the ionization pattern in the divertor region is thus essential for realistic modelling of the background plasma and the electron losses associated with it.

Acknowledgments

This work, supported by the European Communities under the contract of Association between EURATOM/Tekes, was carried out within the framework of the European Fusion Development Agreement. The views and opinions expressed herein do not necessarily reflect those of the European Commission. The computations presented in this document have been made with CSC's computing environment. CSC is the Finnish IT centre for science and is owned by the Ministry of Education.

References

[1] Schneider R *et al* 2006 *Contrib. Plasma Phys.* **46** 3–191
[2] Taroni A *et al* 1992 *Contrib. Plasma Phys.* **32** 438–43
[3] Simonini R *et al* 1994 *Contrib. Plasma Phys.* **34** 368–74
[4] Batishchev O V *et al* 1997 *Phys. Plasmas* **4** 1672–80
[5] Fundamenski W 2005 *Plasma Phys. Control. Fusion* **47** R163–208
[6] Day M *et al* 1996 *Contrib. Plasma Phys.* **36** 419–23
[7] Heikkinen J A *et al* 2001 *J. Comput. Phys.* **173** 527–48
[8] Horacek J *et al* 2003 *J. Nucl. Mater.* **313–316** 931–5
[9] Chodura R 1992 *Contrib. Plasma Phys.* **32** 219–30
[10] Chankin A V *et al* 2007 *Nucl. Fusion* **47** 479–89
[11] Chankin A V *et al* 2006 *Plasma Phys. Control. Fusion* **48** 839–68
[12] Marchand R and Dumberry M 1996 *Comput. Phys. Commun.* **96** 232–46
[13] Rozhansky V *et al* 2006 *Nucl. Fusion* **46** 367–82
[14] Boozer A H and Kuo-Petravic G 1981 *Phys. Fluids* **24** 851–9
[15] Hynönen V *et al* 2007 *Plasma Phys. Control. Fusion* **49** 151–74
[16] Kurki-Suonio T *et al* 2006 *Plasma Phys. Control. Fusion* **48** 1413–24

PUBLICATION II

Modelling of $^{13}CH_4$ injection and local carbon deposition at the outer divertor of ASDEX Upgrade

In: Physica Scripta T138 (2009) 014019 (4 pp).

Phys. Scr. **T138** (2009) 014019 (4pp) doi:10.1088/0031-8949/2009/T138/014019

Modelling of $^{13}CH_4$ injection and local carbon deposition at the outer divertor of ASDEX Upgrade

L Aho-Mantila[1], M I Airila[2], M Wischmeier[3], K Krieger[3], R Pugno[3], D P Coster[3], A V Chankin[3], R Neu[3], V Rohde[3] and the ASDEX Upgrade Team

[1] Helsinki University of Technology, Association Euratom-TEKES, FI-02015 TKK, Finland
[2] VTT Technical Research Centre of Finland, Association Euratom-TEKES, FI-02044 VTT, Finland
[3] Max-Planck Institut für Plasmaphysik, IPP-EURATOM Association, D-85748 Garching, Germany

E-mail: leena.aho-mantila@tkk.fi

Received 28 October 2009
Accepted for publication 5 November 2009
Published 30 December 2009
Online at stacks.iop.org/PhysScr/T138/014019

Abstract
Numerical modelling of $^{13}CH_4$ injection into the outer divertor plasma of the full tungsten, vertical target of ASDEX Upgrade is presented. The SOLPS5.0 code package is used to calculate a realistic scrape-off layer plasma background corresponding to L-mode discharges in the attached divertor plasma regime. The ERO code is then used for detailed modelling of the hydrocarbon break-up, re-deposition and re-erosion processes. The deposition patterns observed at two different poloidal locations are shown to strongly reflect the cross-field gradients in divertor plasma density and temperature, as well as the local plasma collisionality. Experimental results with forward and reversed B_T, accompanied by numerical modelling, also point towards a significant poloidal hydrocarbon $\mathbf{E} \times \mathbf{B}$ drift in the divertor region.

PACS numbers: 52.25.Vy, 52.40.Hf, 52.55.Fa, 52.55.Rk, 52.65.Kj, 52.65.Pp

(Some figures in this article are in colour only in the electronic version.)

1. Introduction

Understanding the interaction between edge plasma and material surfaces is crucial for the design of future fusion reactors. Carbon-based materials have good thermal properties which make them an attractive choice for those plasma-facing components (PFCs) that receive the highest heat loads during the plasma operation. The major difficulty with carbon is its tendency to erode and re-deposit forming hydrogen-rich layers that contribute to long-term tritium retention [1]. In order to reliably predict the tritium inventory from co-deposition in PFCs in future devices, detailed numerical modelling of carbon erosion, transport and re-deposition processes is required. This contribution focuses on SOLPS5.0 and ERO simulations of carbon injected in the form of $^{13}CH_4$ methane into the outer divertor plasma of the ASDEX Upgrade (AUG) tokamak [2, 3].

2. Experiments

In AUG, carbon transport in the divertor region has been investigated by puffing $^{13}CH_4$ into the outer divertor scrape-off layer (SOL) plasma in lower-single null vertical target configuration. The modelling presented here concentrates on a forward field L-mode experiment with line-averaged density $\bar{n}_e = 3.2 \times 10^{19}\,\mathrm{m}^{-3}$, $I_p = +800\,\mathrm{kA}$ and $B_T = -2.5\,\mathrm{T}$, carried out during 11 repeated discharges (#22573-#22585, 2 unsuccessful) at the end of the AUG 2007 experimental campaign with tungsten-coated PFCs [3]. In addition, recent results from a reversed field experiment in 2008 consisting of three discharges (#23651-2, #23654) with $\bar{n}_e = 4{-}5 \times 10^{19}\,\mathrm{m}^{-3}$, $I_p = -800\,\mathrm{kA}$ and $B_T = +2.5\,\mathrm{T}$ are discussed. The trace impurity was injected through two valves located at the same toroidal position but 71 mm poloidally apart (see also figure 2). The nominal injection rates were $3/1 \times 10^{18}\,\mathrm{s}^{-1}$ for the upper valve (UV) and $6/1 \times 10^{18}\,\mathrm{s}^{-1}$ for the lower valve (LV) in forward/reversed field. The

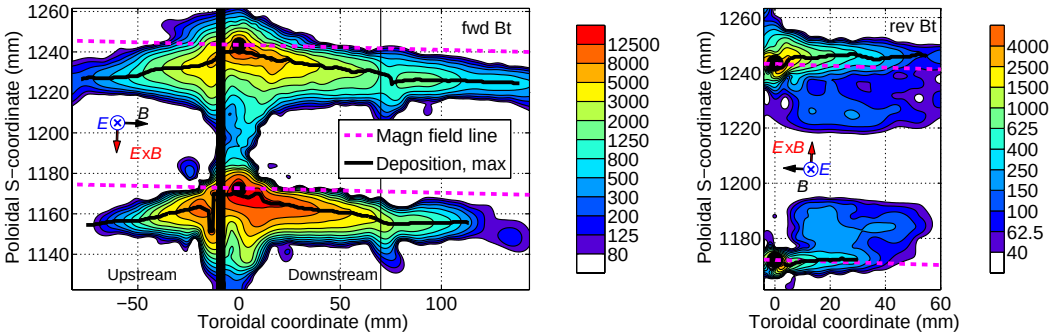

Figure 1. NRA measurements of ^{13}C deposition (10^{15} at cm^{-2}). The figure on the right shows the deposition layer in the AUG experiment with reversed B_T and I_p. For comparison, previously published results in forward field [3] are shown on the left. The black vertical lines represent the gaps between neighbouring tiles.

forward field divertor plasma was in low-recycling regime with $T_e \sim 15$ eV and $n_e \sim 1 \times 10^{18}$ m^{-3}, whereas the reversed field divertor plasma was in high-recycling regime with $T_e \sim 5$ eV and $n_e \sim 1 \times 10^{19}$ m^{-3}.

The lateral distribution of locally deposited ^{13}C was measured by nuclear reaction ion-beam analysis (NRA) for both the forward and the reversed field experiment, see figure 1. Due to uncertainties in the methane injection rates, the analysis may overestimate the net deposition (at most by a factor of 4). The main observations in forward field were full local deposition of the injected carbon, significant fraction (40%) of carbon found toroidally upstream from the injection valve, and a clear deviation of the deposition tail poloidally downwards from the direction of the magnetic field [3]. In reversed field, 80% (UV) and 36% (LV) of injected ^{13}C was measured on the tiles, upstream deposition was strongly suppressed (UV 16%, LV 10% of deposited ^{13}C) and the deposition tail was in the upward poloidal direction. A possible explanation for the poloidal transport could be a sheath $\mathbf{E} \times \mathbf{B}$ drift that reverses its direction with reversal of B_T. However, the discrepancies in local plasma conditions between the two experiments do not allow quantitative analysis of the transport. The present modelling aims at reproducing the above key observations neglecting, for example, colorimetry results on surface roughness effects in forward field [3].

3. Numerical modelling

Modelling of the forward field AUG methane injection experiment is carried out using two separate codes. The SOL plasma is first modelled with the two-dimensional (2D) plasma fluid—Monte Carlo neutrals code package SOLPS5.0 [4], matching the input power and the experimental outer midplane and divertor plasma conditions as closely as possible. Cross-field profiles of T_e, n_e and Γ (ion flux density) along the targets are obtained from Langmuir probes, and spectroscopic signals D_α and CIII have been measured in the divertor region along a poloidally distributed array of lines-of-sight. The effect of $\mathbf{E} \times \mathbf{B}$ and diamagnetic drifts is neglected in the SOL modelling. The calculated values for n_e, T_e, T_i and $u_\parallel$ (ion parallel flow) are then used to describe the plasma background for the detailed impurity modelling with the 3D divertor version of the ERO code [5], assuming

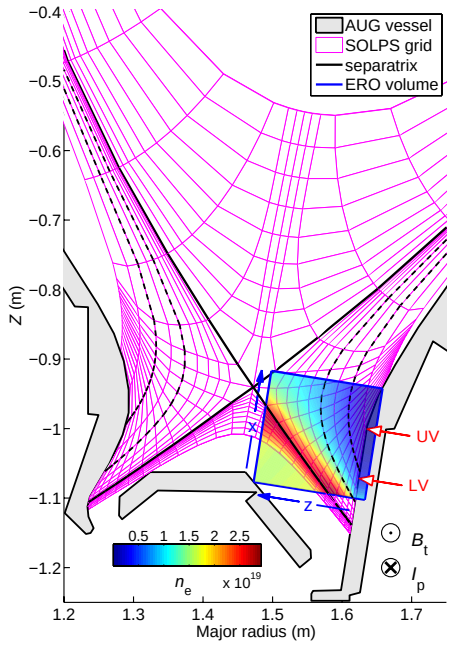

Figure 2. Location of the ERO simulation volume for the upper puffing valve and part of the SOLPS grid used for modelling the forward field injection. The surface plot shows the plasma density calculated with SOLPS, after interpolation to the ERO grid.

toroidal symmetry. Figure 2 shows the location of the ERO simulation volume with respect to the SOLPS grid and the valves.

ERO models the dissociation and ionization reactions of the injected CH_4 with Monte Carlo operators using rate coefficients calculated according to Janev–Reiter data [6]. The transport of ionized particles under the influence of electromagnetic forces is calculated taking the gyro-motion of the test particles and Coulomb collisions with the background plasma into account. The reflection of neutral and ionized carbon from the tungsten surface is calculated according to TRIM results [7]. For the hydrocarbons, the two opposite sticking assumptions $S = 1$ (hydrocarbons never reflect from surface) and $S = 0$ (hydrocarbons always reflect

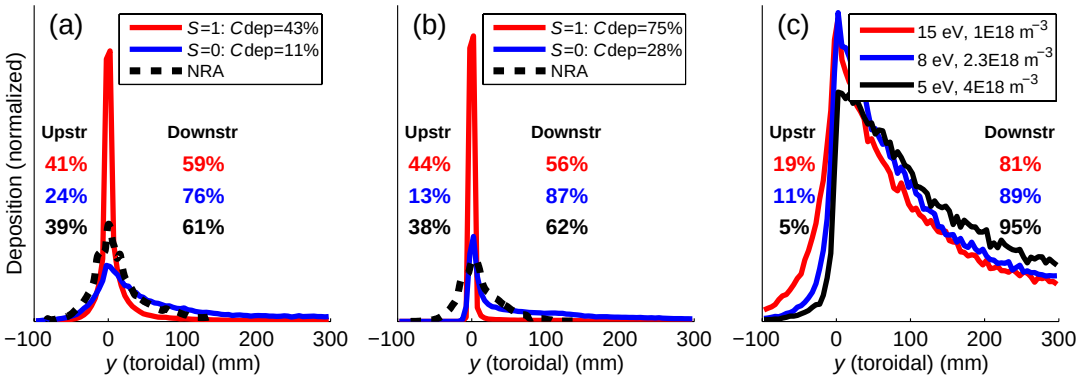

Figure 3. Poloidally integrated profiles of the modelled carbon layer, normalized to the same total deposition. Panels (a) and (b) show the results in forward field for UV and LV, respectively. The legends give the fraction of injected particles deposited in the NRA measurement region, C_{dep}, and the sticking probability S. Panel (c) shows the deposition pattern for three different collisionalities (ν_1, ν_2, ν_3) when $S = 0$.

from surface) are investigated. Physical and chemical erosion of the re-deposited carbon layer are accounted for, assuming chemical erosion yield Y_{chem} to be 1–2% of the incident deuterium flux and homogeneous mixing of carbon within 6 nm of the bulk material [8]. The present modelling takes into account the sheath electric field as calculated in [5]. Realistic modelling of the global electric field in the divertor plasma would require SOLPS calculations with drifts and is therefore left for future work. Accordingly, we have neglected thermal forces in the modelling presented here.

Figures 3(a) and (b) show the modelled toroidal deposition profiles at the two valves. With $S = 1$, the test particles get deposited on first incidence, which produces a peaked deposition around the injection valve. The assumption of non-sticking hydrocarbons $S = 0$ widens the profiles, but more particles ($57 \rightarrow 89\%$ for UV and $25 \rightarrow 72\%$ for LV) are also lost into the plasma or outside the measurement region. Varying Y_{chem} between 1–2% has much smaller effect on the profiles, and the fraction of deposited particles C_{dep} changes only by 1–2%. Due to cross-field gradients in background plasma density and temperature, the shape and thickness of the deposition is notably different between the two poloidal locations. At the LV ($T_{\mathrm{e}} = 22$ eV and $n_{\mathrm{e}} = 0.8 \times 10^{19}$ m^{-3}), the average ionization depth is only $L_{\mathrm{ion}} = 1.3$ mm, significantly limiting the extension of the methane cloud. At the UV ($T_{\mathrm{e}} = 17$ eV and $n_{\mathrm{e}} = 1 \times 10^{18}$ m^{-3}), L_{ion} is 6 mm, yielding a wider deposition layer that resembles the NRA data. The results therefore suggest smaller background plasma gradients and plasma conditions similar to UV.

The local plasma conditions do not only contribute to the flatness and thickness of the carbon layer, but may also affect the relative proportions of upstream and downstream deposition. As the collisionality increases, the friction caused by the plasma flow will force more ionized particles to the downstream direction, increasing the toroidal asymmetry of the deposition. To illustrate this, we consider artificial, homogeneous (no ∇T, ∇n), background plasmas with various collisionalities $\nu = L_{\mathrm{d}}/L_{\mathrm{ion}}$, where L_{d} is the classic Spitzer deflection mean free path for 0.025 eV C$^+$. Figure 3(c) shows the modelled toroidal profiles for three cases: $\nu_1 = 49$, $\nu_2 = 10$ and $\nu_3 = 2.4$, with $S = 0$ and sufficiently high $L_{\mathrm{ion}} = 10 \pm 1$ mm to yield wide profiles. Increasing the collisionality is observed to decrease upstream transport, providing a likely explanation for the negligible upstream deposition in reversed field with the high recycling plasma, recall figure 1. The significant underestimation of upstream deposition at the LV with $S = 0$ also suggests that the plasma density has been overestimated at that location.

Modelling with the SOLPS background plasma reveals that a large fraction of the hydrocarbon transport occurs in the neutral state. Roughly 40% of the hydrocarbon dissociation steps at the UV, occurring over the entire tracing time in the ERO volume, result in neutral atoms or molecules. Therefore, ionized test particles are not necessarily confined to the magnetic field lines for the rest of their plasma dwell time, but may become neutral and return to the surface, see figure 4. Without subsequent neutralization, particles ionized at L_{ion} would never reach the upstream surface parts, and would travel 70 cm (UV) or 15 cm (LV) before impinging on the downstream surface parts. The high fraction of neutral transport therefore enables even significant upstream deposition. However, as part of the neutral dissociation products travel away from the plates, the net deposition fraction remains much below 100%.

The sheath has a negligible effect on the poloidal hydrocarbon transport, as most of it occurs outside the extension of the sheath ($\sim$0.1 mm). In order to estimate the divertor electric field E that reproduces the experimentally observed poloidal transport in forward field, we specify a homogeneous E towards the surface throughout the ERO simulation volume. Figure 5 shows the modelled 2D deposition patterns for $S = 0$ and $E = 0.8$ V mm^{-1}, yielding the best poloidal agreement at the UV. At the LV, the strong parallel transport caused by the friction force reduces the effect of the poloidal $\mathbf{E} \times \mathbf{B}$ drift. The specified E is weak compared with the sheath modelled by either ERO ($\sim$100 V mm^{-1}) or SOLPS ($\sim$10 V mm^{-1}), and it is of the same order as the global electric field in the current SOLPS plasma solution (0.1–1 V mm^{-1}). As thermal forces are excluded in the present modelling, more particles are

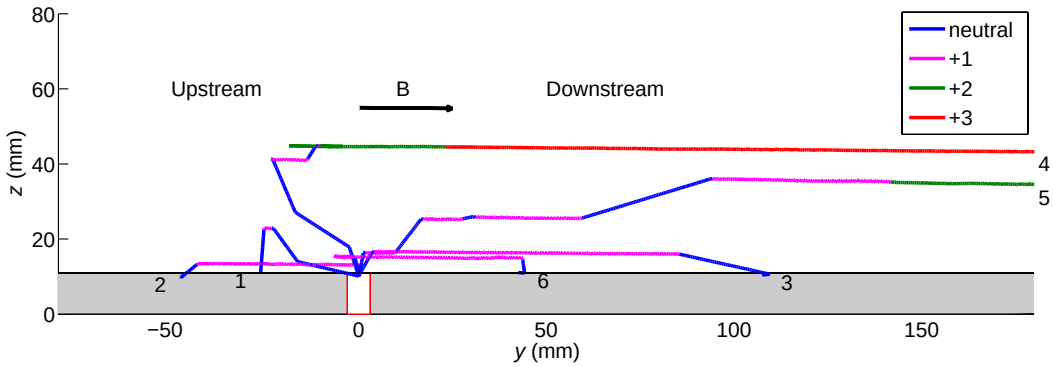

Figure 4. Selected test particle trajectories from ERO simulations for the UV, showing the charge states. As an example, particle number 2 undergoes the following reaction chain: $CH_4 \rightarrow CH^+ \rightarrow C$.

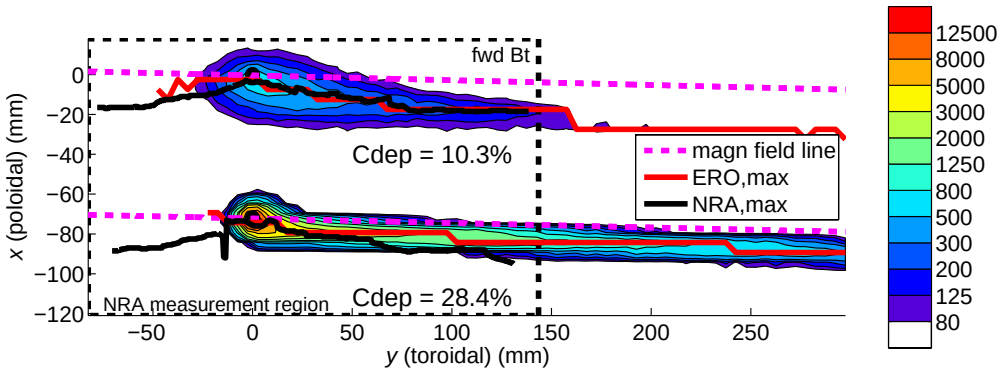

Figure 5. Modelled 2D profile of ^{13}C deposition (10^{15} at cm^{-2}), with sticking assumption $S = 0$ and a homogeneous electric field of 0.8 V mm^{-1} towards the surface. The lines of poloidal maximum deposition are shown and compared with the NRA results, recall figure 1.

pushed to the downstream side of the valves compared with figures 3(a) and (b).

4. Conclusions and outlook

Numerical modelling of the AUG L-mode forward B_T methane injection experiment [3] was carried out using the SOLPS5.0 and ERO codes. The cross-field distributions of background plasma density and temperature along the divertor surface were found to have a profound effect on the level of agreement between modelled and measured carbon deposition. ERO reproduced the wide pattern with deposition toroidally upstream from the injection, provided the ionization mean free path was sufficiently high and collisionality low, but could not match the deposition in a region where higher heat flux was measured. Comparison of experimental results with forward and reversed fields, accompanied by numerical modelling, indicated that an $\mathbf{E} \times \mathbf{B}$ drift in the divertor region could significantly affect the poloidal transport of hydrocarbons. The results therefore call for inclusion of 2D divertor electric potential data in ERO modelling and investigation of drift effects on the background plasma.

Acknowledgments

This work, supported by the European Communities under the contract of Association between EURATOM/Tekes, was carried out within the framework of the Task Force on Plasma Wall Interactions of the European Fusion Development Agreement. The views and opinions expressed herein do not necessarily reflect those of the European Commission. Part of the computations presented in this document have been made with CSC's computing environment. CSC is the Finnish IT centre for science and is owned by the Ministry of Education. Forschungszentrum Jülich, Institut für Energieforschung—Plasmaphysik, is gratefully acknowledged for providing the ERO code for the modelling presented in this work. This work was partially funded by the Academy of Finland project No. 121371.

References

[1] Clark R and Reiter D (ed) 2005 *Nuclear Fusion Research, Understanding Plasma–Surface Interactions* (Berlin: Springer)
[2] Pugno R *et al* 2005 *J. Nucl. Mater.* **337–339** 985–9
[3] Pugno R *et al* 2009 *J. Nucl. Mater.* **390–391** 68–71
[4] Schneider R *et al* 2006 *Contrib. Plasma Phys.* **46** 3–191
[5] Kirschner A *et al* 2000 *Nucl. Fusion* **40** 989
[6] Janev R and Reiter D 2002 *Jül Report Jül-3966*
[7] Kögler U and Winter J 1997 *Jül Report Jül-3361*
[8] Kirschner A *et al* 2009 *J. Nucl. Mater.* **390–391** 152–5

PUBLICATION III

Modelling of Carbon Transport in the Outer Divertor Plasma of ASDEX Upgrade

In: Contributions to Plasma Physics 50, No. 3–5,
439–444 (2010).

Contrib. Plasma Phys. **50**, No. 3-5, 439 – 444 (2010) / **DOI** 10.1002/ctpp.201010070

Modelling of Carbon Transport in the Outer Divertor Plasma of ASDEX Upgrade

L. Aho-Mantila*[1], M. Wischmeier[2], M.I. Airila[3], A.V. Chankin[2], D.P. Coster[2], Ch. Fuchs[2], M. Groth[1], A. Kirschner[4], K. Krieger[2], H.W. Müller[2], E. Wolfrum[2], and **the ASDEX Upgrade Team**

[1] Helsinki University of Technology, Association Euratom-TEKES, P.O. Box 4100, FI-02015 TKK, Finland
[2] Max-Planck Institut für Plasmaphysik, EURATOM Association, D-85748, Garching, Germany
[3] VTT Technical Research Centre of Finland, Association Euratom-TEKES, FI-02044 VTT, Finland
[4] Forschungszentrum Jülich, Association EURATOM-FZJ, Trilateral Euregio Cluster, D-52425 Jülich, Germany

Received 03 September 2009, revised 15 November 2009, accepted 01 December 2009
Published online 10 May 2010

Key words Carbon, impurity transport, divertor, SOLPS, ERO, drifts, electric field
Subject classification 52.25.Vy, 52.40.Hf, 52.55.Fa, 52.55.Rk, 52.65.Kj, 52.65.Pp

Carbon transport in the ASDEX Upgrade outer divertor plasma is investigated in numerical simulations. The SOLPS5.0 code package is used to model the scrape-off layer plasma in a set of repeated lower-single-null L-mode discharges. Special emphasis is given to replicate the plasma conditions measured in the full tungsten, vertical outer target of ASDEX Upgrade, and solutions with and without the effect of drifts are presented. First ERO simulations of hydrocarbon transport in a SOLPS plasma background including drifts are carried out, and significantly closer match to the experimental ^{13}C deposition pattern is obtained than with the solution without drifts. The 2D divertor electric field predicted by SOLPS is applied to the ERO modelling, and it is observed to result in a poloidal hydrocarbon drift that agrees well with the experiment. An increased carbon deposition efficiency, particularly upstream from the source, is obtained in the normal ASDEX Upgrade field configuration.

1 Introduction

Plasma-facing components (PFCs) in most present-day fusion devices are subject to a deuterium influx that erodes the surface material, releasing impurities into the plasma. In addition to physical sputtering, carbon-based materials undergo chemical erosion via hydrocarbon formation. Once released, these impurity molecules follow various dissociation processes in the plasma, get transported into remote regions and, ultimately, deposit back on to the surface along with the fuel particles. The formation of hydrogen-rich layers is of special concern for the future ITER reactor with carbon PFCs in the divertor, due to the presence of radioactive tritium in the fuel mix. In order to assess how critical fuel retention by co-deposition is for long-term operation, better understanding of carbon transport in the divertor target and migration in edge plasma regions is urgently needed.

Two-dimensional fluid codes have been subject to significant code validation efforts and they are extensively used for both interpretative and predictive modelling of the edge plasma regions in a tokamak [1, 2]. To follow the trajectories of impurity particles and their interaction with material surfaces, more sophisticated codes are additionally used: the 3-dimensional Monte Carlo impurity transport code ERO [3] calculates the trajectories of test particles in a given plasma background, including dissociation and ionization processes and the gyromotion of ionized particles, as well as reflection and erosion at the material surface. The present work describes the modelling of an ASDEX Upgrade (AUG) experiment, where tracer $^{13}CH_4$ methane was injected into the outer divertor plasma during lower-single-null (LSN) L-mode discharges [4]. According to the first results presented in [5], the modelled distribution of plasma temperature, density and electric potential along the divertor target

* Corresponding author: e-mail: leena.aho-mantila@tkk.fi, Phone: +358 9 470 25089, Fax: +358 9 470 23195

determine, to a large degree, the local transport of impurities and the resulting deposition pattern on the tiles. In this paper, SOLPS5.0 simulations with a coupled description of fluid plasma and Monte Carlo neutrals are presented in comparison with AUG experimental data, and the effect of activating drift terms on the target solution and resulting carbon deposition is investigated. The primary forces affecting the transport of hydrocarbons in the divertor plasma are identified and the deposition pattern modelled with ERO is compared to results from post-mortem surface analysis.

2 SOLPS5.0 modelling of ASDEX Upgrade L-mode discharges

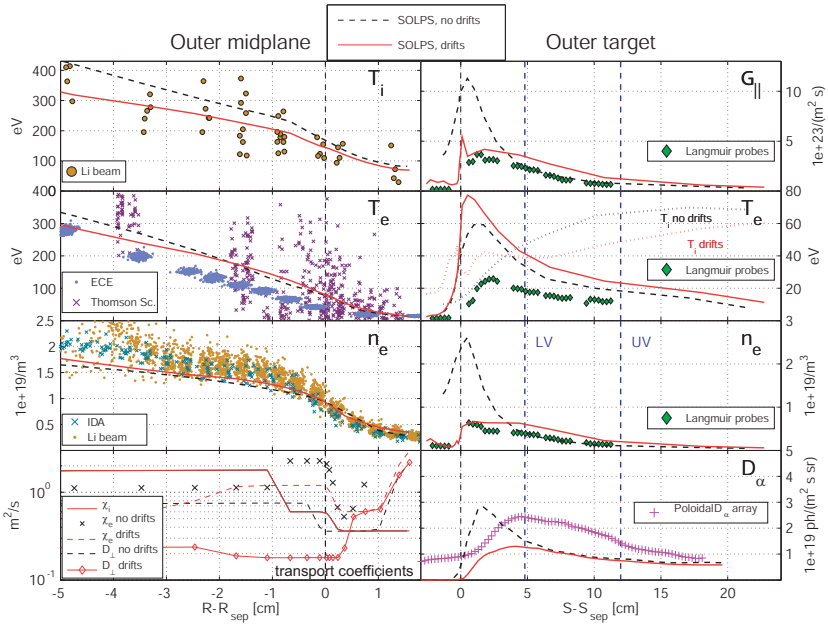

Fig. 1 Measured upstream and outer target profiles for the modelled set of AUG L-mode discharges, along the major radius R and the S-coordinate, respectively. The red solid and black dashed lines show the SOLPS solutions with and without drifts, respectively. The positions of the upper (UV) and lower (LV) valve are denoted with the blue dashed lines in the target profiles. The lower left figure shows the transport coefficients $D_\perp$, χ_i and χ_e specified in the simulations. (Online colour: www.cpp-journal.org).

2.1 Description of the $^{13}CH_4$ injection experiment

Local transport of carbon in AUG divertor plasma was investigated by injecting isotopically labelled ^{13}C tracer methane from two valves separated by 71 mm in the poloidal direction along the vertical outer target, the lower valve residing 47 mm above the strike point in the scrape-off layer [4, 5]. Injection of the trace impurity was carried out during 11 repeated LSN L-mode pulses (#22573-#22585, 2 unsuccessful) in deuterium fuelled plasmas, with B_T=-2.5T and I_p=0.8MA in the normal operation mode, i.e. ion $\nabla\mathbf{B}$ drift towards the divertor targets. The discharges had on average 0.75 MW of ECRH and 0.35 MW of Ohmic heating, and the feedback-controlled line-averaged plasma density was 3.2×10^{19} m^{-3}. The outer divertor plasma was in the attached regime and characterized in a separate discharge (#22469) by Langmuir probe (flush-mounted) measurements of the ion saturation current $J_{\rm sat}$ and electron temperature $T_{\rm e}$ during a vertical strike point sweep. Measurements of D_α and CIII line emission along a poloidally distributed array of lines-of-sight were also carried out. Upstream from the puff, at the low-field-side (LFS) midplane, radial profiles of $n_{\rm e}$, $T_{\rm e}$ and $T_{\rm i}$ covering the scrape-off layer (SOL) and

pedestal regions were measured using Lithium beam, ECE radiometer and Thomson scattering system during the actual injection experiment. A complementary n_e profile was obtained by combining the profiles from several diagnostics (IDA). The radiated power was monitored by a bolometer during another set of similar characterization discharges (#24187-#24189). Fig. 1 shows the experimental upstream and target plasma profiles.

2.2 SOLPS5.0 simulations

The scrape-off layer plasma in the experiment was modelled using the SOLPS5.0 code package, with the plasma fluid code B2.5 coupled with the Monte Carlo neutrals code Eirene-99 [6]. Calculation of parallel transport in B2.5 is based on the Braginskii equations, with kinetic corrections to the heat fluxes. Transport perpendicular to the flux surfaces is described by setting radially varying coefficients for anomalous diffusion $D_\perp$ and ion and electron heat conductivities $\chi_{i,e}$. The simulations were carried out on a 48x18 grid extending 7 cm into the core and 1.6 cm outside the separatrix on the LFS midplane, and covering 22 cm of the outer divertor target poloidally outside the separatrix (see also [5], Fig. 2). In addition to the fuel species, all charge states of the main impurities (C and He) were included in the solution. This work presents the first SOLPS simulations for ERO plasma background that were carried out with the diamagnetic and **E** x **B** drift terms activated.

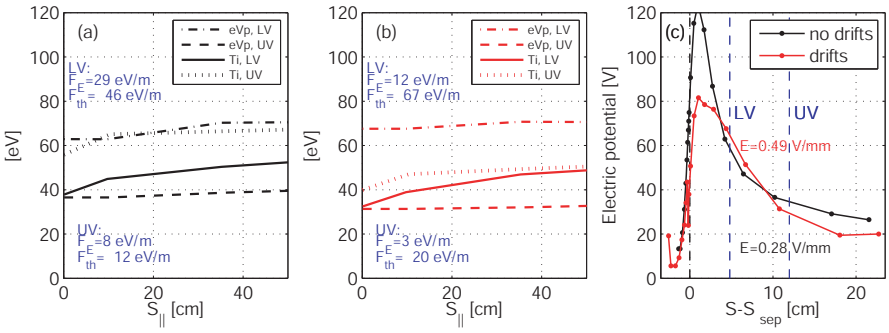

Fig. 2 Parallel profiles of electric potential V_p and T_i in the SOLPS solutions without (a) and with (b) drifts, on the flux surfaces closest to the valve locations. The parallel connection length to the target is denoted by $S_\parallel$, and the parallel electric and thermal forces are given for $S_\parallel$ ∼10 cm, corresponding to ∼5 mm distance normal to the target surface. Fig. (c) shows the profiles of V_p following the target surface and gives the strength of the electric field component parallel to the surface in between the two valves. (Online colour: www.cpp-journal.org).

The upstream separatrix density n_{sep} was kept on a constant, prescribed level by a midplane D_2 gas puff that was placed outside the SOL and operated in a feedback mode. Due to the scatter in the measured n_{sep}, as shown in Fig. 1, several runs were attempted with n_{sep} varying between 0.7-1.1×10^{19}m^{-3}. Bolometer measurements yield roughly 0.8 MW total radiation, from which ∼0.2 MW is emitted inside the separatrix. In the simulations, P_{in} ∼1 MW power is specified at the core boundary and, as a first approximation, it is assumed to be equally shared between ions and electrons. The focus of the present work is to obtain an outer target solution that corresponds to the Langmuir probe measurements of parallel flux density $\Gamma_\parallel$ (extracted from J_{sat}) and target electron temperature $T_{e,t}$. In addition, a reasonable correspondence with the experimental upstream profiles of n_e, T_e and T_i is sought for, in order to produce a realistic 2-dimensional plasma background for ERO.

The solutions giving the closest match to both upstream and target measurements, obtained with and without activated drift terms, are shown in Fig. 1 with the solid (drifts) and dashed (no drifts) lines. As discussed in several earlier publications (most recently in [7]), SOLPS has a tendency to overestimate target density $n_{e,t}$. This feature is visible in the solution without drifts which shows unrealistically high, peaked profiles of $n_{e,t}$ and $\Gamma_\parallel$. Activation of drift terms leads to a more even distribution of $n_{e,t}$ with significantly lower strike point density (1/5 compared to no-drift runs), despite the lower $D_\perp$ assigned compared to the no-drift case. Upstream, the density profiles remain within the scatter in measurement points, with n_{sep}=0.95×10^{19}m^{-3}. Both solutions give higher $T_{e,t}$ than what is measured with the probes. Very small parallel gradients of T_e are obtained and, therefore, $T_{e,t}$ is largely determined by upstream conditions. In both cases, the modelled upstream T_e remains above the level

measured by the ECE diagnostics but the large scatter in other measurement points yields notable uncertainty in the scrape-off layer T_e profile. In the presence of ECRH, fractions of P_in smaller than 40% for the electrons seem unlikely solutions and further investigations for decreasing $T_\mathrm{e,t}$ were left for future work. Close to the valve locations (see the blue dashed lines in Fig. 1), best agreement with the measured target parameteres is obtained with the SOLPS solution without drifts, despite the reasonably good overall agreement obtained when activating the drift terms.

In addition to deriving the first SOLPS drift solution for an ERO plasma background, this work describes the first inclusion of electric field and thermal forces predicted by SOLPS in ERO simulations. The effect anticipated in [5] is a net force parallel to the field lines and a poloidal **E** x **B** drift towards the separatrix. According to the results presented in [5], the hydrocarbons get ionized < 1 cm away from the valve, in the direction normal to the surface. This close to the surface, the parallel profile of the electric potential is largely influenced by the sheath boundary conditions, and could therefore be reasonably described even when drift terms are excluded from the modelling. The perpendicular profile is more likely to be influenced by the cross-field drifts. Figs. 2(a)-(b) show the parallel profiles of electric potential V_p and T_i for the two SOLPS solutions discussed here, and the corresponding V_p profiles along the target are shown in Fig. 2(c). The parallel electric force $F_{\parallel,E}$ that pushes the particles towards the target is weaker than the thermal force $F_{\parallel,\mathrm{th}}$ that acts in the direction of increasing temperature, see Figs. 2(a)-(b). This is particularly true for the drift solution. The resulting net effect of these forces is therefore transport toroidally upstream, away from the valve. Depending on the collisionality, this net parallel transport could be cancelled or even reversed by plasma friction that pushes the impurities downstream, as discussed in [5]. The electric field component towards the surface is 0.1-1V/mm, and an equally significant component parallel to the surface is observed in Fig. 2(c). All components of the electric field are stronger at the lower valve compared to the upper valve.

3 ERO modelling of hydrocarbon transport in the outer divertor plasma

The methane molecules injected through the two valves are modelled with the ERO code [3], taking a 3-dimensional simulation volume with Δy=40 cm toroidal, Δx=16 cm poloidal and Δz=16 cm radial (inside

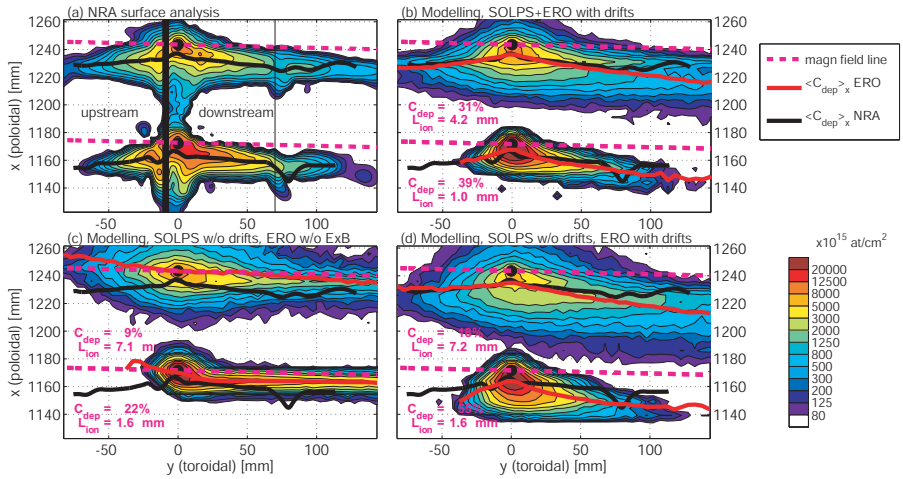

Fig. 3 2D ^{13}C deposition patterns on the divertor surface, from post-mortem NRA measurements [4] (a) and modelling with (b) and without (c)-(d) drifts in the SOLPS background. In (c), **E** x **B** drift of hydrocarbons is modelled only within the electrostatic sheath calculated by ERO [5]. For ease of comparison, the modelled deposition has been rescaled to the net deposition observed in the experiment, and the modelled deposition efficiency is denoted with $\mathrm{C_{dep}}$. The lines of poloidal mean deposition ($\langle \mathrm{C_{dep}} \rangle_x$) are also drawn. (Online colour: www.cpp-journal.org).

the plasma) extension (see also [5]). ERO models the dissociation and ionization reactions of the injected $^{13}CH_4$ with Monte Carlo operators using rate coefficients calculated according to Janev-Reiter data [8]. The transport of ionized particles under the influence of electromagnetic forces is calculated taking the gyro-motion of the test particles and Coulomb collisions with the background plasma into account. The code calculates reflection of neutral and ionized carbon from the tungsten surface according to TRIM results [9]. In this work, negligible sticking of hydrocarbons and a chemical re-erosion yield (calculated within time steps of 1 s) equal to 2% of the incident deuterium flux is assumed [5, 10]. More detailed investigations of plasma-surface interaction shall be carried out in the future. The plasma background is described by 2D profiles of n_e, T_e, T_i and the ion flow velocity, $u_{\|}$, extracted from the SOLPS solution. In addition to the modelling presented in [5], thermal forces arising from parallel temperature gradients are taken into account as described in [3]. The electric potential, as shown in Fig. 2, is used to calculate the electric field components E_x (along the surface) and E_z (normal to surface) throughout the ERO simulation volume, assuming E_y=0 (toroidal direction).

In the $^{13}CH_4$ experiment presented in Section 2.1, the local ^{13}C deposition was measured by nuclear reaction ion-beam analysis of the surrounding tungsten-coated graphite tiles. Comparison of the modelled steady-state deposition pattern to the observed one is presented in Fig. 3, for the two SOLPS backgrounds. The effect of **E** x **B** drift in ERO simulations is further visualized by comparing the simulations to a case with only $E_{\|}$ included from SOLPS (Fig. 3c). Due to a possible miscalibration of the experimental injection rates, the nominal deposition efficiencies C_{dep}=100% reported in [4] for both valves are uncertain. Therefore, the modelled patterns in Fig. 3 are scaled to the net depositions obtained with NRA. As described in [5], the extension and flatness of the deposition layer correlates with the average ionization depth L_{ion} of the methane molecules. The longest L_{ion}=7.2 mm is found in the no-drift background that has the lowest T_e at the UV location, yielding a too flat carbon layer compared to the NRA measurements and a lower deposition efficiency (C_{dep}=18%) compared to the LV (C_{dep}=55%) or both valves in the drift background (C_{dep}=31-39%). The LV patterns in both backgrounds are too peaked, as L_{ion} is decreased to < 2 mm. Best match to the NRA measurements is obtained with the drift background for the UV, where the observed layer profile is well reproduced with L_{ion}=4.2 mm. The measured 2/5 deposition toroidally upstream from the valve is also reasonably well reproduced when drifts are included in SOLPS. At both valves, 1/3 of net deposition is upstream from the injection, whereas in the no-drift background only 1/4 upstream deposition is observed at the UV.

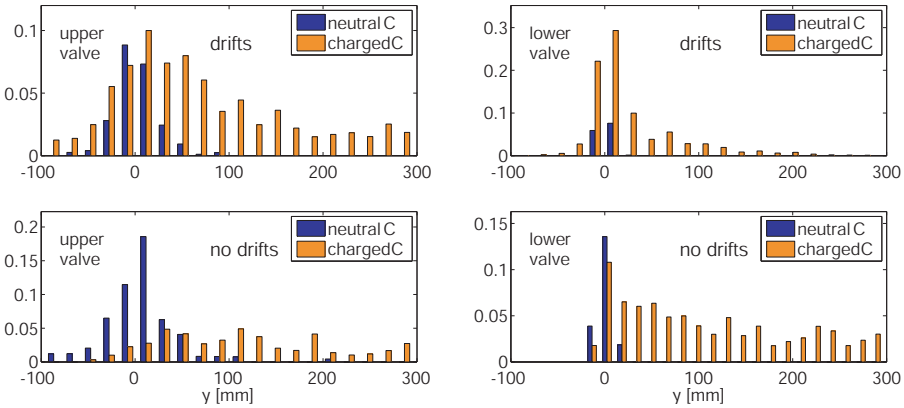

Fig. 4 Distribution of neutral and charged carbon impinging on the divertor surface in ERO simulation, when SOLPS plasma background with drifts (above) or without drifts (below) is used. In the latter case, only $E_{\|}$ from SOLPS is included in ERO simulations. (Online colour: www.cpp-journal.org).

ERO simulations reproduce the observed poloidal downward drift only when the full 2D divertor electric field in the SOLPS drift solution is included in the modelling. Net transport towards the separatrix occurs because of an **E** x **B** drift experienced by the ionized particles in the presence of non-zero E_z. The stronger E_z in the no-drift background yields too large poloidal transport, particularly at the LV, and the effect of **E** x **B** drift is more

pronounced downstream compared to upstream direction. When only $E_{\|}$ is taken from the (no-drift) SOLPS solution, recall Fig. 3(c), very little net poloidal transport is observed, and the influence of electric and thermal forces on the parallel transport is small. To further illustrate the effect of background conditions and drifts, the distribution of neutral and charged carbon impinging on the target surface is given in Fig. 4 for the cases shown in Figs. 3(b)-(c). As the ionization depth decreases, less neutrals are observed at the target. In the no-drift solution, the upstream deposition observed at the UV is caused by neutral dissociation products, since in this magnetic configuration the field lines in upstream direction guide the ionized particles away from the surface [5]. In the drift solution, the upstream deposition at both valves is, however, dominated by ionized particles. In this case, the ions get deposited due to the **E** x **B** drift associated with non-zero E_x, recall Fig. 2(c), yielding transport towards the surface. The drifts therefore lead to a striking increase of net deposition efficiencies by a factor of 2-3, as shown in Fig. 3. The different E_x profiles in the no-drift and drift backgrounds shown in Fig. 2 also explain part of the dissimilarities in the deposition layers in Figs. 3(b) and (d): Smallest E_x is observed at the UV in the no-drift background, decreasing the upstream deposition there, and highest E_x is found at the LV in the same background, limiting the toroidal transport and increasing the net deposition at that location.

4 Conclusions and Outlook

Numerical modelling of hydrocarbon transport in an ASDEX Upgrade outer divertor plasma was carried out using the SOLPS5.0 and ERO codes, with drifts activated in the plasma background for the first time. Good agreement between SOLPS modelling and target measurements was obtained close to where $^{13}CH_4$ was injected, and the 2D electric field and thermal forces were included in the background model for ERO. The divertor electric field was observed to yield a significant **E** x **B** drift of the puffed hydrocarbons along and towards the target surface, leading to a close correspondence with the experimental observations when drifts were included in SOLPS. In particular, increased deposition efficiencies were obtained in the AUG normal field configuration due to the **E** x **B** drift. To further improve the correspondence between modelling and measurements, careful investigations of surface interaction and recalibration of the $^{13}CH_4$ injection rate will be carried out.

Acknowledgements This work, supported by the European Communities under the contract of Association between EURATOM/Tekes, was carried out within the framework of the Task Force on Plasma Wall Interactions of the European Fusion Development Agreement. The views and opinions expressed herein do not necessarily reflect those of the European Commission. The work was partially funded by the Academy of Finland project No. 121371. Part of the computations presented in this document have been made with CSC's computing environment. CSC is the Finnish IT centre for science and is owned by the Ministry of Education.

References

[1] A.V. Chankin, D. P. Coster, R. Dux, C. Fuchs, G. Haas, A. Herrmann, L.D. Horton, A. Kallenbach, M. Kaufmann, C. Konz, K. Lackner, C. Maggi, H.W. Müller, J. Neuhauser, R. Pugno, M. Reich, and W. Schneider, Plasma Phys. Control. Fus. **48**, 839868 (2006).
[2] M. Wischmeier, M. Groth, A. Kallenbach, A.V. Chankin, D. P. Coster, R. Dux, A. Herrmann, H.W. Müller, R. Pugno, D. Reiter, A. Scarabosio, and J.G. Watkins, J. Nucl. Mater. **390-391**, 250 254 (2009).
[3] A. Kirschner, V. Philipps, J. Winter, and U. Kögler, Nucl. Fusion **40**, 989 (2000).
[4] R. Pugno, K. Krieger, M. Airila, L. Aho-Mantila, A. Kreter, S. Brezinsek, V. Rohde, D. Coster, A. Chankin, and M. Wischmeier, J. Nucl. Mater. **390-391**, 6871 (2009).
[5] L. Aho-Mantila, M.I. Airila, M.Wischmeier, D.P. Coster, A.V. Chankin, K. Krieger, R. Pugno, R. Neu, and V. Rohde, Phys. Scr. **T 138**, 014019 (2009).
[6] R. Schneider, X. Bonnin, K. Borrass, D. Coster, H. Kastelewicz, D. Reiter, V. Rozhansky, and B. Braams, Contrib. Plasma Phys. **46**(1-2), 3191 (2006).
[7] A.V. Chankin, D. P. Coster, R. Dux, C. Fuchs, G. Haas, A. Herrmann, L.D. Horton, A. Kallenbach, B. Kurzan, H.W. Müller, R. Pugno, M. Wischmeier, E. Wolfrum, and the ASDEX Upgrade Team, Nucl. Fus. **49** (2009), 015004.
[8] R. Janev and D. Reiter, Jül report Jül-3966, 2002.
[9] U. Kögler and J. Winter, Jül report Jül-3361, 1997.
[10] A. Kirschner, D. Borodin, V. Philipps, U. Samm, R. Ding, K. Schmid, J. Roth, A. Kukushkin, G. Federici, and A. Loarte, J. Nucl. Mater. **390-391**, 152155 (2009).

Series title, number and report code of publication

VTT Publications 773
VTT-PUBS-773

Author(s)
Leena Aho-Mantila

Title

Divertor plasma conditions and their effect on carbon migration in the ASDEX Upgrade tokamak

Abstract

Divertors play a critical role in power and particle exhaust and plasma-material interaction in tokamaks. Of particular concern is the release of impurities from the material components, which reduces the lifetime of the vessel wall and affects the fusion performance. Furthermore, impurities with low charge number can migrate and re-deposit forming potentially tritium-rich layers in the tokamak. Sophisticated numerical simulations are required to understand how the various complex and often nonlinear processes in the plasma boundary affect the divertor performance.

This thesis investigates the plasma conditions and the migration of impurities in the divertor region, using numerical code packages with the most complete available description of the relevant physical processes. It is known from earlier studies that the codes have both weaknesses and uncertainties in their models, which limits our current predictive capabilities. In this thesis work, carbon injection experiments at the ASDEX Upgrade tokamak are modelled. The work assesses the present-day boundary plasma models and elucidates impurity migration processes by comparing the simulations with experimental data.

The results show that both the local migration and the net erosion of carbon are sensitive to the divertor plasma conditions. Good agreement between the modelled and measured divertor plasma parameters is obtained for a limited operational regime at low density. In this regime, the measured carbon migration is also reproduced in the simulations, and it is shown to be significantly affected by the electric field and the collisionality of the plasma in the divertor region. A significant improvement in code-experiment agreement is obtained after drifts arising from electric and magnetic fields are included in both plasma and impurity simulations. At higher plasma densities, collisionless hot electrons are a potential explanation for the deficiencies observed when benchmarking the plasma models against experiments.

ISBN
978-951-38-7756-9 (soft back ed.)
978-951-38-7757-6 (URL: http://www.vtt.fi/publications/index.jsp)

Series title and ISSN	Project number
VTT Publications 1235-0621 (soft back ed.) 1455-0849 (URL: http://www.vtt.fi/publications/index.jsp)	73461

Date	Language	Pages
October 2011	English, finnish abstr.	76 p. + app. 62 p.

Name of project	Commissioned by

Keywords	Publisher
Tokamak, plasma-material interaction, scrape-off layer, kinetic modelling, fluid modelling, ASDEX Upgrade, fusion energy	VTT Technical Research Centre of Finland P.O. Box 1000, FI-02044 VTT, Finland Phone internat. +358 20 722 4520 Fax +358 20 722 4374

Julkaisun sarja, numero ja raporttikoodi

VTT Publications 773
VTT-PUBS-773

Tekijä(t)
Leena Aho-Mantila

Nimeke

Diverttorin plasmaolosuhteet ja niiden vaikutus hiilen kulkeutumiseen ASDEX Upgrade -tokamakissa

Tiivistelmä

Diverttorilla on tärkeä rooli tokamakin ensiseinämän läheisyydessä olevan plasman olosuhteiden ja plasma-materiaalivuorovaikutuksen säätelyssä. Erityisenä huolena on materiaalipintojen eroosio, joka lyhentää seinämien elinikää ja tuottaa epäpuhtauksia plasmaan. Epäpuhtauksien kulkeutumisesta riippuu, miten epäpuhtaudet vaikuttavat fuusioreaktorin suorituskykyyn ja mihin ne kerrostuvat uudelleen, mahdollisesti yhdessä tritiumin kanssa. Koska diverttorin toimintaan vaikuttavat prosessit ovat monimutkaisia ja epälineaarisia, niiden kuvaamiseen tarvitaan kehittyneitä simulointiohjelmistoja.

Tässä väitöskirjassa tarkastellaan diverttorialueen plasmaolosuhteita ja epäpuhtauksien kulkeutumista käyttäen tulevaisuuden koelaitteiden suunnitteluun tähtääviä simulointiohjelmistoja. Nämä ohjelmistot sisältävät viimeisimmät saatavilla olevat fysiikkamallit, mutta aiemmat työt ovat tuoneet esille merkittäviä epävarmuuksia niiden laskentatuloksissa. Väitöskirjassa simuloidaan ASDEX Upgrade -tokamakilla tehtyjä kokeita, joissa hiiltä on injektoitu diverttorialueelle. Työssä arvioidaan nykyisten reunaplasmamallien oikeellisuutta ja selvitetään hiilen kulkeutumisominaisuuksia vertaamalla simulaatiotuloksia kokeellisiin mittauksiin.

Työn tulokset osoittavat, että hiilen kokonaiseroosio ja paikallinen kulkeutuminen vaihtelevat diverttorin plasmaolosuhteiden mukaan. Simulaatioilla pystytään hyvin toistamaan mitatut plasmaolosuhteet rajatulla alhaisen tiheyden käyttöalueella. Tässä tapauksessa myös mallinnettu hiilen kulkeutuminen vastaa mittaustuloksia, ja sen osoitetaan riippuvan voimakkaasti diverttorialueen sähkökentästä ja plasman törmäyksellisyydestä. Sähkö- ja magneettikentistä johtuvan ajautumisen huomioiminen parantaa merkittävästi niin plasma- kuin epäpuhtaussimulaatioiden vastaavuutta koetulosten kanssa. Törmäyksettömät korkeaenergiset elektronit voivat selittää simulaatioiden ja kokeiden välisiä eroavaisuuksia suuremmilla plasmatiheyksillä.

ISBN
978-951-38-7756-9 (nid.)
978-951-38-7757-6 (URL: http://www.vtt.fi/publications/index.jsp)

Avainnimeke ja ISSN	Projektinumero
VTT Publications 1235-0621 (nid.) 1455-0849 (URL: http://www.vtt.fi/publications/index.jsp)	73461

Julkaisuaika	Kieli	Sivuja
Lokakuu 2011	Englanti, suom. tiiv.	76 s. + liitt. 62 s.

Projektin nimi	Toimeksiantaja(t)

Avainsanat	Julkaisija
Tokamak, plasma-material interaction, scrape-off layer, kinetic modelling, fluid modelling, ASDEX Upgrade, fusion energy	VTT PL 1000, 02044 VTT Puh. 020 722 4520 Faksi 020 722 4374

A tokamak device which relies on magnetic confinement of plasma is a promising concept for a fusion power plant. The big challenge facing the world fusion community is now the development of a tokamak which can operate with the high power flux densities relevant for a commercial fusion reactor. This necessitates that controlled power and particle exhaust scenarios and a material design which withstands the impinging plasma are developed. A crucial component is the tokamak divertor, which is characterized by tremendously complex plasma-wall interaction processes. This thesis investigates the behaviour of the divertor plasma and the associated release and transport of materials in the reactor-relevant ASDEX Upgrade tokamak. The validity of models used for predicting reactor operation is assessed through comparisons between numerical calculations and existing experimental data.

ISBN 978-951-38-7756-9 (soft back ed.)
ISSN 1235-0621 (soft back ed.)

ISBN 978-951-38-7757-6 (URL: http://www.vtt.fi/publications/index.jsp)
ISSN 1455-0849 (URL: http://www.vtt.fi/publications/index.jsp)